Oksana Savchak

Licenciatura em Bioquímica

Manganese oxide nanoflowers and liposome encapsulated superoxide dismutase microreactors on preventing oxidative stress

Dissertação para obtenção do Grau de Mestre em

Bioquímica para a Saúde

Orientador: Sandra Henriques Vaz, PhD, Instituto de Medicina Molecular João Lobo Antunes, Faculdade de Medicina da Universidade de Lisboa; Instituto de Farmacologia e Neurociências, Faculdade de Medicina da Universidade de Lisboa.

Co-orientador: Adam Armada-Moreira, PhD, Instituto de Medicina Molecular João Lobo Antunes, Faculdade de Medicina da Universidade de Lisboa; Instituto de Farmacologia e Neurociências, Faculdade de Medicina da Universidade de Lisboa.

Orientador interno: Hugo Miranda, PhD, CEDOC | NOVA Medical School, Faculdade de Ciências Médicas da Universidade de Lisboa

Maio de 2021

Oksana Savchak

Licenciatura em Bioquímica

Manganese oxide nanoflowers and liposome encapsulated superoxide dismutase microreactors on preventing oxidative stress

Dissertação para obtenção do Grau de Mestre em

Bioquímica para a Saúde

Orientador: Sandra Henriques Vaz, PhD, Instituto de Medicina Molecular João Lobo Antunes, Faculdade de Medicina da Universidade de Lisboa; Instituto de Farmacologia e Neurociências, Faculdade de Medicina da Universidade de Lisboa.

Co-orientador: Adam Armada-Moreira, PhD, Instituto de Medicina Molecular João Lobo Antunes, Faculdade de Medicina da Universidade de Lisboa; Instituto de Farmacologia e Neurociências, Faculdade de Medicina da Universidade de Lisboa.

Orientador interno: Hugo Miranda, PhD, CEDOC | NOVA Medical School, Faculdade de Ciências Médicas da Universidade de Lisboa

Júri:

Presidente: Prof. Doutor António Sebastião Rodrigues

Arguente: Prof. Doutora Ana Paula Gomes Moreira Pêgo

Vogal: Prof. Doutora Maria Teresa Nunes Mangas Catarino

Faculdade de Ciencias Medicas da Universidade Nova de Lisboa

CEDOC| Nova Medical School

Maio de 2021

Хто вам сказав, що я слабка,
що я корюся долі?
Хіба тремтить моя рука
чи пісня й думка кволі?
Ви чули, раз я завела
жалі та голосіння, —
то ж була буря весняна,
а не сльота осіння.

Леся Українка

Published Work

▪Armada-Moreira A, Gomes JI, Pina CC, **Savchak OK**, Gonçalves-Ribeiro J, Rei N, Pinto S, Morais TP, Martins R, Ribeiro FF, Sebastião AM, Crunelli V, Vaz SH. Going the extra (synaptic) mile: excitotoxicity as the road towards neurodegenerative diseases. Front. Cell. Neurosci. (2020)

Oral communications

▪ **Savchak OK**., Armada-Moreira A., Ramos-Docampo MA., Ribeiro FF., Sebastião AM., Städler B., Vaz SH. *Wolf in sheep's clothing: microreactor encapsulated manganese oxide nanoflowers*. 51st Annual Meeting of Pharmacology Portuguese Society and XIX Meeting of Toxicology, Portugal, February 17th-19th 2021.

▪ Gonçalves-Ribeiro J., **Savchak OK**., Morais TP., Lopes RF., Meneses C., Santisteban R., Lillo A., Crunelli V., Navarro-Brugal G., Franco R., Sebastião AM., Vaz SH. *Dual Effect of A1R and A2AR upon CB1R signalling in cortical astrocytes*. 51st Annual Meeting of Pharmacology Portuguese Society and XIX Meeting of Toxicology, Portugal, February 17th-19th 2021.

▪ Costa-Coelho T., Fonseca-Gomes J., Garcia G., Ferreira-Manso M., **Savchak OK**., Pinto S., Sebastião AM., Brites D., Diógenes MJ. – *Vesicle dissemination of neuronal TrkB-ICD in secretome: relevance for Alzheimer's disease pathophysiology*. 51st Annual Meeting of Pharmacology Portuguese Society and XIX Meeting of Toxicology, Portugal, February 17th-19th 2021.

▪ **Savchak OK**, Armada-Moreira A, Ribeiro FF, Sebastião AM, Vaz SH. *Cell antioxidant mechanisms mimicry: two generations of microreactors*. Neuroscience seminar, iMM, Lisboa, Portugal, November 2nd, 2020

▪ **Savchak OK**, Armada-Moreira A, Ribeiro FF, Sebastião AM, Vaz SH. *Nanotechnology approach to neuroinflammation: cell-like reactors in three-dimensional inflammation models*. Jornadas Intercalares Anuais dos Mestrados dos Departamentos de Química e de Ciências da Vida 2020, Faculdade de Ciência e Tecnologia (FCT), Lisbon, Portugal, February 13th-14th, 2020

▪ **Savchak OK**, Armada-Moreira A, Ribeiro FF, Sebastião AM, Vaz SH. *Nanotechnology approach to neuroinflammation: cell-like reactors in three-dimensional inflammation models*. XXXVIII Annual Meeting of Pharmacology Portuguese Society and XIX Meeting of Toxicology, Coimbra, Portugal, February 5th-7th 2020.

▪ **Savchak OK**, Armada-Moreira A, Ribeiro FF, Sebastião AM, Vaz SH. *Nanoparticle and liposome-based microreactors as reactive oxygen species scavengers in a 3D model of neuroinflammation.* Neuroscience seminar, iMM, Lisboa, Portugal, November 11th, 2019

Poster presentations

▪ **Savchak OK,** Armada.Moreira A., Ramos-Docampo MA., Ribeiro FF., Sebastião AM., Städler B., Vaz SH. *Manganese oxide nanoflowers containing microreactors to support neuroblastoma cells against oxidative stress.* MANA International Symposium 2021, International Center for Materials Nanoarchitectonics, National Institute for Materials Science, Japan.

▪ **Savchak OK,** Armada.Moreira A., Ramos-Docampo MA., Ribeiro FF., Sebastião AM., Städler B., Vaz SH. *Flowers and Blades. Manganese oxide nanoparticles in cell like reactors targeting oxidative stress*. AIMS Research competition, Annual International (bio)Medical Students Meeting, Faculdade de Medicina, Universidade de Lisboa, Portugal.

▪ **Savchak OK**, Armada-Moreira A, Ribeiro FF, Sebastião AM, Vaz SH. *Nanoparticle and liposome-based microreactors as reactive oxygen species scavengers in a 3D model of neuroinflammation*. 5th Annual Meeting of the PhD Students of the Mind-Brain College, University of Lisbon, Lisbon, Portugal, November 13th 2019.

Agradecimentos

Primeiramente quero agradecer à minha orientadora, Sandra Vaz. A investigação nem sempre vem fácil. Muitas vezes é dolorosa, e não funciona, e encontra novas maneiras de nos desmotivar. É importante termos alguém para nos ensinar as práticas de laboratório e teoria de investigação. Foi essencial ter alguém que me conseguiu apoiar. Que consegue apoiar toda a gente. Que sabe tão bem o quão difícil pode ser e está lá, inspira e continua em frente, e puxa com ela. Que se preocupa tanto com cada alto e baixo, com cada pessoa, e que cria o ambiente de mais do que apenas um grupo. Estiveste lá nos bons dias e maus dias e só espero que nunca te esqueças que também estarei por ti. Eu pensava que sabia o que é um "orientador", no entanto redefiniste o termo. Para sempre agora a palavra orientador significara algo mais.

Adam Moreira, mais do que mentor, mostraste me uma coisa que tanto procurei. Curiosidade. De olhar para algo novo e de repente ver se uma ideia a acender na cabeça. Ou para algo antigo. Ou comum. Ver e pensar, "e se fosse diferente?". De não seguir um caminho convencional e encontrar o teu próprio, mesmo que não seja o mais fácil. Espero que alguma vez os nossos caminhos ainda irão intercetar, até porque os nossos interesses científicos estão deveras próximos. Agradeço todo o esforço que tiveste de me ensinar, todas as dúvidas que esclareceste e todas as vezes que estavas disponível quando pedia ajuda. Mas também por me teres dado autonomia. Gostaria de pensar que aprendi muito e certamente uma muito grande parte disto foi contigo.

Gostaria de agradecer a Dr. Brigitte Städler, pela oportunidade de discutir o trabalho consigo, por toda a ajuda no projeto e pela oportunidade de planear futuros trabalhos consigo. Foram sempre discussões muito interessantes e todo o apoio que me deu ajudou-me a chegar onde estou hoje. Agradeço também ao Dr. Miguel A. Ramos-Docampo pela disponibilidade para ajudar e pelo estudo mais aprofundado das nanopartículas.

Gostaria também de agradecer a professora Ana Maria Sebastião pela oportunidade de trabalhar no seu laboratório onde tive a oportunidade de aprender, crescer cientificamente e encontrar uma equipa fantástica.

Carolina, quantas vezes já falamos a tentar nos lembrar quando ficamos tão próximas? Quando passamos a falar todos os dias e quando começamos a planear todas as viagens? E quando planeamos a nossa principal, uma casa nas montanhas, com lareira, gatos, livros e mais ninguém. Onde teremos paz. Foram mil conversas serias e nem tanto. E

tantas duvidas, tantos receios, e felicidades. E discussões de sonhos esquisitos. E de nos sentimos a vontade para partilhar quando não estávamos bem porque sabemos que vamos ser compreendidas. Há mil agradecimentos e nenhum fica bem expresso em papel. No entanto mereces cada um deles.

As astros, o melhor grupo que se poderia desejar. A cooperação, entreajuda e a conexão que temos. E tantos interesses diferentes no mesmo grupo que encontram uma maneira de cooperar e de seguirmos com preocupação os sucessos de cada uma de nós. As reuniões com comida e com as distrações para falar de cusquices. As lindas bichas da glia, saídas pré-pandemia e as infinitas tentativas de combinar uma chamada de grupo, que nunca funciona por alguma razão. O entusiasmo da Joana Gomes que nada e ninguém consegue vencer e a luz em ti a brilhar tão intensamente. A Joana Ribeiro, i feel you on a spiritual level. Portanto reclamemos até o fim do mundo! E a Sara Pinto, a mais nova do grupo, no entanto quem encaixou como uma peça do mesmo puzzle. Tu não tinhas outra opção, universo preparou te para as bichas da glia. Carolina, a bicha estrangeira que fugiu de nós, continuaras nos nossos corações.

Tiago Coelho, quantas horas de sono em falta temos em soma? Já nos conhecíamos a algum tempo, no entanto foi no mestrado que ficamos apenas nos os dois. E ficamos amigos. E discutimos. E ficamos amigos outra vez. E andamos em círculos até nos habituarmos um ao outro. Mas de alguma maneira laboratório e ciência para mim ficou imprescindível da tua presença. E pelo tal agradeço toda a ajuda, e não agradeço todas as vezes que fiquei até tarde para te ajudar. No entanto voltaria a faze lo.

Fabio e Vera, as minhas majestics, fizeram e farão uma parte muito importante de mim. A nossa amizade sobreviveu o tempo, o afastar dos caminhos e os zodíacos da Vera. O nosso trio é algo que espero que consigamos segurar para até sermos muito velhos.

Murilhas, Ju, Francisco, Chica, Daniela, Diogo. Sem vocês a faculdade não seria a mesma. Todos os momentos que partilhamos, todas as brincadeiras e todo o falecimento no DQ, sempre tão gelado.

Батькам за допомогу, терпець а також за віру в мене, коли в мені її більше не залишалося. Та й за то що стільки віддали бо хотіли побачити лише щоб я змогла мати те життя яке хочу. За те що завжди стояли за мною горою та підтримували коли я падала. Ми нечасто то говоримо один одному але знаємо що воно є так. І так буде. Я буду стояти також за вами, завжди.

Abstract

The lack of antioxidant defences and high oxygen consumption rates render the brain vulnerable to oxidative stress. While most treatments target the scavenging of reactive oxygen species (ROS), cell mimicry does so by offering a long-term antioxidant support to protect the brain cell population from oxidative damage. Layer-by-layer microreactor assembling technique allows the development of personalized therapeutic particles, incorporating various active principles into targeting pertinent issues. For instance, catalytic activity can be achieved by superoxide dismutase (SOD) or manganese oxide (Mn_3O_4) nanoflowers. Incorporation of liposome-encapsulated enzyme SOD (L_{SOD}) and/or nanoflowers in microreactors allows drawing a line between natural and artificial catalytic entities in cell mimicry.

Thus, this work aimed to expand the use of microreactors to support neuroblastoma cells and mixed primary cultures against H_2O_2- and lipopolysaccharide (LPS) both physically and enzymatically. Microreactors were assembled with a polystyrene core, following by the deposition of polydopamine and poly-*L*-lysine precursor layers before immobilizing only nanoflowers or nanoflowers+L_{SOD} as intermediate layers.

Synthesized nanoflowers and microreactors showed both SOD and catalase activity, while L_{SOD} retained low activity that was abolished by microreactor assembly, and therefore considered redundant for posterior use. While nanoflowers showed significant toxicity at low concentrations when incubated with cells, microreactors with integrated nanoflowers caused an inhibition of cell proliferation and only minor toxicity at high concentrations. Importantly, cells in the presence of the microreactors showed higher viability when subjected to H_2O_2, illustrating their capacity to rescue cells from oxidative stress induced death. Primary cultures showed consistence with the previous toxicity results but also a rise in intracellular ROS, reflective of possible underlying nanoflower effect.

Taken together, microreactors with dual catalytic activity are a cell mimicry approach that can assist their mammalian counterpart to survive changes in their environment.

Keywords: oxidative stress; manganese oxide nanoflowers; cell mimicry; layer-by-layer; microreactors.

Resumo

O cérebro é particularmente vulnerável ao stress oxidativo, uma vez que tem um elevado consumo de oxigénio que leva à produção de espécies reativas de oxigénio (ERO) e, simultaneamente, expressa uma baixa quantidade de enzimas antioxidantes. Enquanto a maioria dos tratamentos para o stress oxidativo se focam na eliminação das ERO, o mimetismo celular, que inclui reatores que podem incorporar várias entidades ativas, é considerado um novo modelo de tratamento eficiente e durador. Por exemplo, o consumo de ERO produzidas em excesso pode ser alcançado através da utilização da enzima superóxido dismutase (SOD) e de nanoflores de óxido de manganês.

Este trabalho teve como objetivo o desenvolvimento de microreatores com capacidade de mimetizar as características celulares antioxidantes, de modo a prevenir o stress oxidativo induzido por H_2O_2 e lipopolisacárido (LPS) na linha celular SH-SY5Y de neuroblastoma humano e em culturas primárias mistas, respetivamente. SOD encapsulado em lipossomas (L_{SOD}) e nanoflores foram sintetizados e caracterizados física- e cataliticamente. Microreatores foram construídos a partir dum núcleo de poliestireno, incorporando nanoflores ou nanoflores+L_{SOD} como entidades ativas, e com deposição electroestática de camadas intermédias de polidopamina e poli-*L*-lisina.

Quer as nanoflores, quer os microreatores, demonstraram atividade de SOD e catalase. O L_{SOD} mostrou atividade baixa de SOD, que foi anulada pela incorporação destes no microreactor. Enquanto as nanoflores livres mostraram altas taxas de toxicidade na linha celular SH-SY5Y, quando incorporadas nos microreactores, estes mostraram baixos níveis de toxicidade direta e inibição de proliferação na linha celular. Os microreactores foram capazes de reverter parcialmente a viabilidade da linha celular tratada com H_2O_2, no entanto induziram um aumento nos níveis de ERO intracelulares nas culturas primarias, representativo de um efeito dual.

Globalmente, microreatores demonstraram a capacidade de proteção antioxidante às células, oferecendo uma alternativa aos habituais agentes terapêuticos e representando um suporte enzimático para as células biológicas.

Palavras-chave: stress oxidativo; mimetização celular; nanoflores de oxido de manganês; microreator.

List of Abbreviations

BBB	Blood-Brain Barrier
CAT	Catalase
CD68	Cluster of Differentiation 68
CNS	Central Nervous System
DA	Dopamine
DHE	Dihydroethidium
DPPC	Dipalmitoylphosphatidylcholine
GFAP	Glial Fibrillary Acidic Protein
GPx	Glutathione peroxidase
GSSH/GSH	Oxidized glutathione/reduced glutathione
Iba1	Ionized calcium binding adapter protein 1
LbL	Layer-by-Layer deposition
LPS	Lipopolysaccharide
NADPH	Nicotinamide adenine dinucleotide phosphate
PB	Phosphate Buffer
PBS	Phosphate Buffer Saline
PDA	Poly-dopamine
PI	Propidium iodide
PLL	Poly-*L*-Lysin
PMAc	Poly (methacrylic acid)-*co*- (colesteryl methacrylate)
PS	Polystyrene particles
PUFA	Polyunsaturated fatty acids
ROS	Reactive oxygen species
SA	Stearylamine
SEM	Scanning Electron Microscopy
SOD	Superoxide dismutase
TEM	Transmission Electron Microscopy.

Contents

1. Introduction 1

1.1. Oxidative stress 1

1.1.1. Reactive oxygen species and a series of unfortunate events: oxidative stress, cytotoxicity, and system dysregulation 1

1.1.1.1. Superoxide dismutase is a superstar. 6

1.1.2. Oxidative stress pathogenesis in the brain: a seesaw between neurodegeneration and oxidative stress 7

1.2. Nanotechnology 9

1.2.1. Brief history course – diving deep to the very bottom 9

1.2.2. Nanotechnological approach to science 10

1.2.3. Organic and lipid nanomaterials. Liposomes. 13

1.2.4. Liposome-encapsulated SOD enzyme 17

1.2.5. Metal and metal oxide nanoparticles: a brave new world 17

1.2.6. Metal nanoparticles-associated toxicity – every fairy-tale needs a villain 20

1.2.7. Manganese oxide nanoflowers 22

1.3. Synthetic biology and cell mimicry 24

1.3.1. Up the ladder: artificial enzymes, organelles, and cells. 25

1.3.2. Layer-by layer deposition 27

1.3.3. Microreactors and astrosomes 28

1.4. Scientific aims 29

2. Methods 31

2.1. Reagents and Materials 31

2.2. Nanofabrication 32

2.2.1. Manganese oxide nanoflower synthesis. 32

2.2.2. Superoxide dismutase-containing liposome synthesis 32

2.2.3. Microreactor assembly 33

2.2.4. Determination of microreactor concentration 34

2.2.5. Physical characterization of synthesized materials 34
2.2.6. Deposition control 34
2.2.7. Electron Microscopy 35
2.2.8. Superoxide dismutase activity assay 35
2.2.9. AmplexRed H_2O_2 assay 36
2.3. SH-SY5Y neuroblastoma cell line 36
2.3.1. Cell maintenance 36
2.3.2. Nanomaterial and microreactors exposure 36
2.3.3. Microreactor *in situ* activity upon oxidative stress 37
2.4. Primary cell cultures 37
2.4.1. Culture 37
2.4.2. Nanoparticle and microreactor exposure 38
2.4.3. Inflammation induction 38
2.4.3.1. ROS measurement 38
2.4.3.1. Immunocytochemistry 39
2.4.3.2. Western Blot 39
2.5. Cell viability 41
2.6. Statistical analysis 42
3. Results 43
3.1. Manganese oxide nanoparticles 43
3.1.1. Transmission and scanning electron microscopy (TEM and SEM) 43
3.1.2. Dynamic light scattering and ζ- potential 44
3.1.3. Enzymatic activity 47
3.2. Liposomes 50
3.2.1. Dynamic light scattering (DLS) and ζ- potential 51
3.2.2. Enzymatic activity 54
3.3. Microreactors 56
3.3.1. First generation of microreactors: Mn_3O_4 nanoflowers and liposome-encapsulated superoxide dismutase 56

3.3.1.1. Physical characterization 56
3.3.1.2. Enzymatic activity 60
3.3.2. Second generation: Mn_3O_4 nanoflowers-containing microreactors 61
3.3.2.1. Physical characterization 61
3.3.2.2. Enzymatic activity 63
3.4. SH-SY5Y neuroblastoma cell line 65
3.4.1. Nanoparticle and liposome toxicity in SH-SY5Y neuroblastoma cells 65
3.4.2. First generation microreactors toxicity in SH-SY5Y neuroblastoma cells 68
3.4.3. Second generation microreactors toxicity in SH-SY5Y neuroblastoma cells 70
3.4.4. Microreactors rescuing SH-SY5Y neuroblastoma cell line from H_2O_2 induced oxidative stress. 72
3.5. Mixed primary cortex cell culture 74
3.5.1. Neuroinflammation induction 74
3.5.2. Manganese oxide nanoparticles and first generation microreactors toxicity to primary cultures 77
3.5.3. Nanoparticle and microreactor activity upon reactive oxygen species 78
4. Conclusions and future perspectives 81
5. References 85
6. Supplementary Data 100

Table of Figures

Figure 1: Main antioxidant enzymatic reactions of the cells. 5
Figure 2: Timeline of technology discoveries that allowed detailed studies and development of nanotechnology. 10
Figure 3: Schematic representation of main approaches of material manipulation at the nanoscale. 11
Figure 4: Molecular structure of the liposome membrane. 14
Figure 5: Crystalline structure of hausmannite (Mn_3O_4) manganese oxide particles. 23
Figure 6: Mn_3O_4 nanoflowers. 43
Figure 7: Enzymatic activity of Mn_3O_4 nanoflowers. 47
Figure 8: Superoxide dismutase activity of liposomes and enzymes in free solution. 54
Figure 9: Deposition control in first generation microreactors. 57
Figure 10: Superoxide dismutase like activity of free Mn_3O_4 nanoflowers and microreactors containing liposome encapsulated SOD and Mn_3O_4 nanoflowers in free solution. 60
Figure 11: Deposition control in second generation microreactors. 62
Figure 12: Enzymatic activity of second generation microreactors. 63
Figure 13: Concentration-dependent nanomaterial toxicity evaluation in SH-SY5Y neuronal cell line. 66
Figure 14: Concentration-dependent first generation microreactors cytotoxicity study in SH-SY5Y neuroblastoma cell line. 69
Figure 15: Second generation microreactors cytotoxicity assessment in SH-SY5Y neuroblastoma cells. 70

1. Introduction

As an open system, the human organism is dependent on a constant interchange of energy and material with the outside world. This means it had to develop reliable mechanisms of protection as well as adaptive systems. Consumed food contains toxins that are excreted by clearance systems (liver, kidneys, etc.), inhaled air contains pollens and microparticles that must be filtered, open wounds are seen as friendly invitations by pathogenic bacteria, which must be fought off, as tissues are being repaired. Even the consumption of oxygen required to produce the necessary energy for basic functions results in the production of reactive molecules that can damage the system around them. While the human organism found a way to adapt to these threats, sometimes glitches in the system can occur. When there self-autonomous functions fail to divert these threats, humans are forced to rely on their ingenuity to design strategies to compensate for what the body cannot do.

Search for adequate therapies has faced issue after issue. The present lack of knowledge is the main cause that holds humanity back from successfully treating many diseases. Every invention, every new technology, was eventually turned into the field of medicine. Organic and inorganic, of human, of animal, of plant, of pure chemical lab origin, all were tried in the attempted counter-action where nature failed. This thesis will discuss the damage inflicted by oxidative stress, the ways it can deteriorate living systems and a new way to approach the problem – nanotechnology and cell mimicry.

1.1. Oxidative stress

1.1.1. Reactive oxygen species and a series of unfortunate events: oxidative stress, cytotoxicity, and system dysregulation

Reactive oxygen species (ROS) is a term used to chemically characterize reactive molecules containing oxygen atoms. Their high reactivity is due to one or more unpaired electrons at the outer valence orbital, which also confers a high instability. Most physiologically abundant ROS are superoxide anion (O_2^-), hydroxyl radical (HO^-) and hydrogen peroxide (H_2O_2). O_2^- and H_2O_2 are usually considered primary ROS, as they are directly produced by respiration and metabolic processes. Secondary ROS are generated mostly as a result of interaction between O_2^- or H_2O_2 with other

compounds, as for example enzymes or metal catalysts or HO^-, formed from the H_2O_2. (*1*, *2*). ROS are normally produced in small quantities by living organisms, resulting from normal cell functioning and also as a response to internal or external stimuli, such as oxidative stress, inflammation or ionizing radiation (*3*).

O_2^- is a primary by-product of mitochondrial respiratory chain. Also called electron transport chain, it is a series of four complexes responsible for a string of redox reactions and establishment of electron transfer throughout the reactions coupled to the proton transfer across the membrane. As redox reactions are highly exergonic, the electron transfer chain is used by the organism as a way of adenosine triphosphate (ATP) production (*4*). The main utilization of oxygen by the respiratory chain occurs in the complex IV, by the enzyme cytochrome C oxidase, as it transfers the electrons to molecular oxygen, generating this way water as the final by-product of respiratory chain (*5*). Due to strict temporal, substrate availability, and direction of the reaction control (*4*, *6*), reactions' intermediates are highly stable and almost all of the oxygen is converted into the end product, with only a small portion escaping the route by reacting with other components of the respiratory chain. Around 1-2% of oxygen that escapes the full process is converted into O_2^- and released into the mitochondria matrix and intra- and extracellular space (*7*, *8*). The leaks have been shown to originate from the complex I (NADH dehydrogenase) and complex III (ubiquinol cytochrome C oxidoreductase) (*9*). However, new studies suggest that, while both complexes release O_2^-into the mitochondrial matrix, complex III is the only one capable of also releasing this ion into the cytosol. As cell membranes are highly impermeable to charged O_2^- ions, these are mainly released into the matrix and are unable to escape intact mitochondria. Their presence in the cytosol can be indicative of mitochondrial damage or degeneration (*10*).

The main sources of H_2O_2 differ from the O_2^-. While it is not directly produced by the respiratory chain, it can be found in the mitochondrial and adjacent cytosol space due to the superoxide dismutase (SOD) enzyme's activity. Other sources of H_2O_2 include peroxisomes and endoplasmic reticulum (*11*, *12*). Peroxisomes are an important topic when considering ROS, specially H_2O_2. Peroxisomes are both production and scavenging sites of ROS and reactive nitrogen species (RNS), as they are the main sites of oxygen consumption, release, and utilization in metabolic processes. H_2O_2 -generating enzymes are a vast range of oxidases, involved, for instance, in α- and β- oxidation and generation of nitric oxides. As peroxisomes are constantly exposed to large quantities of oxygen radicals, they also contain high quantities of ROS-scavenging enzymes, distinguishing the catalase and glutathione

peroxidase, but also Mn-SOD, an enzyme traditionally referred to as mitochondrial (*13*). The delicate ROS production/scavenging equilibrium controlled by peroxisomes is also responsible for the ROS-mediated signalling, discussed further in the chapter.

H_2O_2 cannot be considered a free radical, as it does not contain any unpaired electrons. Some studies emphasize the unreactivity of pure H_2O_2 but, nonetheless, recognise its accentuated contribution to cytotoxicity. Due to its weaker charge, the molecule easily crosses biological membranes where, by reacting with reduced forms of metallic centres of certain enzymes, it can be decomposed into HO^- radicals (*14*, *15*). HO^- are extremely reactive, unstable and oxidize any organic molecule they encounter, which makes them dangerous to the organism. When discussing oxidative stress and ROS danger to the organism, the main players are usually HO^- radicals and the molecules oxidized by them, such as proteins and lipids. HO^- are mostly formed by the Fenton reaction, which involves H_2O_2 metabolically produced by cells, as previously mentioned and reduced active metal ions, usually iron and copper (*16*, *17*). Because of its high reactivity, HO^- reacts with nearby molecules, usually within a range of less than 2 nm, so the damage inflicted by it is usually localized.

Deleterious ROS effects are observed in a system where, for any reason, a higher production of ROS occurs, or where there is a deficiency of enzymatic and non-enzymatic antioxidants responsible for their clearance. Both case scenarios lead to an imbalance in oxidant/antioxidant equilibrium and a rise in ROS concentrations. Free ROS in the system can cause, as previously referred, lipid peroxidation, oxidation of proteins and DNA damage. While there are other effects, the above are usually described and seen as the main contributors for ROS-induced toxicity.

Lipids are the most abundant component of biological membranes so, logically, their damage or destruction may lead to serious consequences for the cell. ROS, specially HO^-, primarily attack the double bonds of polyunsaturated fatty acids (PUFA), resulting in hydroperoxides and lipid peroxyl radicals (*18*). When HO^- acts upon membrane lipids, it attacks glico- and phospholipids, as well as the cholesterol that composes the membrane (*19*). At this stage, the lipids are still physiologically stable, but a new agent enters the game: metal centre complexes. Active metal ions, usually part of reduced proteins and enzyme metallic centres, promote further lipid oxidation and breakdown into reactive radicals, while also contributing to the H_2O_2 decomposition (*20*). As the human organism has a high content of iron and copper centre complexes, this reaction and cellular damage is only limited by the balance of ROS/antioxidant defence mechanisms. While cells can usually compensate

membrane lipid damage resulting from accumulation of lipid peroxidases to a certain extent, high oxidation rates increase membrane' permeability and decrease its fluidity and membrane potential, resulting in compromised cell function and ultimately membrane rupture and cell death (*21*).

DNA oxidation by ROS can not only cause particular cell damage and death, but it also has the ability to promote mutations that can cause transcription and translation errors, causing large scale damage. It was estimated that from the total number of DNA damage events, a significant portion is inflicted by ROS. Exposure of DNA to free radicals can cause double strand breaks, DNA-protein cross linking (*22*), and base modifications (*23*). Base modifications can cause modifications in nucleotide pairings, causing point mutations in the DNA strand (*16*, *24*). Elevated concentrations of ROS during the cell proliferation cycle can result in aberrant chromatin repackaging and incorrect chromosome recombination. In cases where in which the damage is detected during cell proliferation, it will frequently result in cell cycle arrest, by inhibiting mitosis or meiosis (*24*). In some cases, if the oxidative stress burst inflicted too significant of a damage (for example double strand breaks that are hardly repairable), cells initiate the apoptosis cascade (*25*).

Protein oxidation can occur by different mechanisms, yielding different consequences for the system. ROS can attack the protein backbone, peptide bonds or amino acid residues that are susceptible to oxidation (*26*). When oxidizing the protein backbone, $HO^{\cdot}$ radical attacks the α-hydrogen, forming, in this way, a radical carbon atom in either α-carbon or side chains (*27*). When ROS act upon peptide bonds they either interfere during the deamidation pathway or oxidize proline residues. Both scenarios were proven to cleave the peptide bond between amino acids and cause protein fragmentation. Another event that can lead to protein damage is the oxidation at the side chains of amino acids. While they are all susceptible to oxidation, cysteine and methionine residues are the most affected by the action of ROS and RNS. Even in mild ROS exposure, these residues are easily oxidized into disulfides and methionine sulfoxides, respectively (*28*). As cysteines are one of the amino acids responsible for the formation of disulphide bridges (-SH group), their oxidation may gravely interfere with protein structure, correct folding, and interaction with other molecules. However, most of the systems also possess counterbalancing mechanisms such as disulfide reductases and methionine sulfoxide reductases that can convert the residues into their initial oxidation state, thus preventing the damage that can be caused by a dysfunctional protein and, subsequently, preventing more serious damage by "sacrificing" the repairable residues and protecting both peptide bonds

and protein backbone (*29*). Another mechanism that can lead to cell damage is abnormal protein glycation promoted by ROS. Glycation can induce structural changes in proteins, resulting in their partial or full loss of activity. Protein misfolding, loss of function and gain of toxic function (for example accumulation and aggregation in tissues) is a hallmark of numerous diseases, both easily treatable and with no treatment at all (*30*–*32*).

Living organisms also possess antioxidant defences against ROS inflicted damage. These can be divided into primary enzymatic defences and secondary defences, usually non-enzymatic or not specifically targeted for ROS. Main primary antioxidants are catalase (CAT), superoxide dismutase (SOD) and glutathione peroxidase (GPx). Their activity as ROS scavengers is schematically represented in the **figure 1** (*33*). Secondary antioxidant defences target preferentially the free radical inflicted damage where, for example, ATP and Ca^{2+}- independent proteases combat oxidatively damaged proteins (*1*, *34*), while oxidation damaged DNA is detected and repaired by endonucleases III (pyrimidines), glycosylases (purines) and other base excision mechanisms (*35*, *36*).

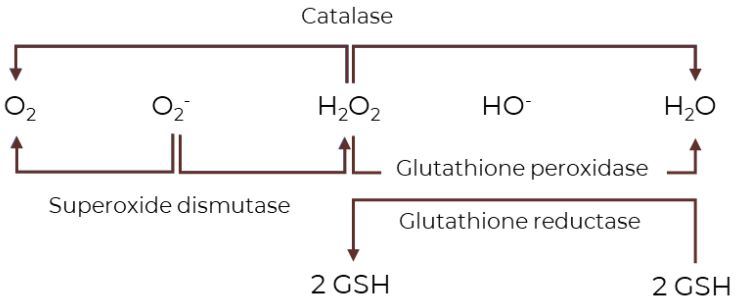

Figure 1: Main antioxidant enzymatic reactions of the cells. Superoxide dismutase enzyme is responsible for converting the O_2^- into hydrogen peroxide and molecular oxygen, while catalase and glutathione peroxidase further scavenge the system from hydrogen peroxide to prevent cellular damage. The outcome of enzymatic antioxidant reactions are water, molecular oxygen, and reduced glutathione.

Similarly to cells' physiological pH gradients, these also create specific gradients of redox equilibriums throughout the cell, generally using H_2O_2 for that purpose due to its unreactivity and stability (*37*). While both CAT and GPx enzymes are able to scavenge H_2O_2, CAT is usually seen more in the perspective of defence scavenging as the catalytic activity is much faster and predominant in high concentrations of H_2O_2, while GPx if preferable in the maintenance of ROS sensitive GSSG/GSH (oxidized glutathione/reduced glutathione) (*38*) and NADPH/$NADP^+$ (Nicotinamide adenine dinucleotide phosphate) (*39*, *40*), responsible for the redox

equilibrium and oxidative stress sensing. ROS, especially H_2O_2, are important signalling molecules. For instance, one of their function is highly selective protein cysteine residue oxidation, that reversibly or irreversibly modifies their structure (*41*). Many signalling events involving ROS consist of the oxidation of biomolecules, susceptible to it, biomolecules that, in their turn, activate signalling networks. As the variation in ROS concentrations, therefore higher rates of biomolecules oxidation are a direct product of rise in ROS levels and oxidative stress, signalling events are mainly but not exclusively involved in cell cycle control, cellular repair, and apoptosis/necrosis pathways (*42*).

1.1.1.1. Superoxide dismutase is a superstar.

SOD is considered one of the most powerful antioxidants in nature and has been intensely explored for decades as a therapeutic agent (*43*). It scavenges the O_2^- ion, which, while not being the most toxic, is the precursor to many other reactive oxygen and nitrogen species, many of them much more toxic and damaging to the system. SOD acts by converting O_2^- into H_2O_2 and molecular oxygen. In humans, SOD enzyme can be found in three isoforms, which vary in terms of the metal cofactor. SOD 1 contains a copper-zinc cofactor and is mostly found in the cytosol (*44*, *45*), SOD 2 with a manganese cofactor, being mainly found in the mitochondrial matrix (*45*), and, finally, SOD 3, which also contains a copper and zinc cofactor enzyme, is excreted specifically to extracellular space (*46*).

SOD has been an attractive therapeutic agent for a long time. It has been applied as a treatment of oxidative stress related diseases such as ischemia (*47*), rheumatoid arthritis (*48*), cancer, brain edema (*49*), among many others. Administration of enzymatic antioxidants in inflammatory diseases, in particular SOD had better therapeutic efficiency than the non-enzymatic ones. However, it presents some restrictions for the direct use, such as non-specific distribution, very short circulation time in biological liquids (blood, plasma) and inability to penetrate biological membranes due to high molecular weight (*50*, *51*). Upon oral administration, SOD is degraded by proteolysis, while, if injected intravenously, it is eliminated by renal clearance within 6-10 minutes (*50*). To overcome this, several delivery methods has been tested, starting from the direct manipulation and modification of the SOD molecules by functionalization (PEGylation, etc.) (*52*, *53*) and to encapsulation in polymer particles, archaeosomes (*50*), and liposomes (*47–49*, *54–59*).

1.1.2. Oxidative stress pathogenesis in the brain: a seesaw between neurodegeneration and oxidative stress

The brain consumes around 20% of all oxygen supply (*60*), which is extremely high when considering its weight ratio to the rest of the body (2%). It has high-energy demands and metabolic activity rates, and, as a result, it produces high amounts of ROS. Unfortunately for the brain, it is not that well equipped for its own requirements. Low levels of antioxidants (*61*), high number of non-replicating cells susceptible to oxidative stress (namely neurons) (*62*), high content of PUFA susceptible to lipid peroxidation (*63*), all these factors make the brain an easy target for pathological oxidative stress.

Neurons contain around 50% less cytosolic GSH and 50 times lower catalase levels than hepatocytes (*64*). While this is not an issue in homeostasis, these features allied to the fact that neurons also have low levels of H_2O_2 (in the scale of nM (*65*)), makes them far less resistant to ROS bursts and oxidative stress. Interestingly, SOD enzyme concentrations are not significantly lower in neurons in relation to any other cell and are essential for neuronal survival (*66*). In order to prevent oxidative stress, the brain has also developed adaptation mechanisms. Prevent, not treat, is the brain's' slogan. Neurons and glial cells metabolize low amounts of fatty acids, giving a preference to glucose or ketone bodies (*67*) in order to meet their energetic demands, but, as the β-oxidation of fatty acids demands more oxygen, that also implies generating higher amounts of ROS (*67*, *68*).

Calcium (Ca^{2+}) signalling, excitotoxicity and oxidative stress are the ouroboros of the brain. One can cause another, and they go in circles until cells succumb. In homeostatic scenario, neurons maintain a steady Ca^{2+} gradient, with low intracellular and high extracellular [Ca^{2+}]. This ion plays the role of a secondary messenger, regulating synaptic plasticity, gene expression, energy production and membrane excitability (*69*). The regulation of signalling is achieved through the regulation of intracellular/extracellular [Ca^{2+}], via voltage-dependent Ca^{2+} channels or receptor operated channels (*70*, *71*). Receptor operated channels activation and consequent influx of Ca^{2+} is tightly related to elevated ROS production. While the main Ca^{2+} storage organelle in the cell is the endoplasmic reticulum, the mitochondria also plays a major role in determining the amplitude and duration of Ca^{2+} transients (*72*, *73*). Production of ROS is dependent of oxidative phosphorylation – a process heavily reliant on the proton gradient and membrane potential. In cases of excitotoxicity, the overload of Ca^{2+} influx caused by overstimulation of N-methyl-D-aspartate (NMDA) receptor

destabilizes the mitochondrial membrane potential (*74*), causing higher ROS production. Another proposed mechanism for the elevation of ROS production is Ca^{2+} induced cytochrome c release, that can not only promote abnormal ROS production, but also lead to an outer membrane rupture, promoting the release of ROS to cytoplasm (*75*).

Inflammation and oxidative stress go hand in hand in the central nervous system (CNS). For instance, microglia is the main ROS source in the CNS, producing it through oxidative phosphorylation, or by intracellular peroxidases and NADPH oxidases, with the latter being the main source of ROS in activated microglia (*76*). Moreover, O_2^- produced by NADPH oxidases is predominantly extracellular (*77*). While SOD 3, the extracellular form of SOD enzyme, scavenges the ion, one of the resulting by-products is H_2O_2. Being highly membrane permeable, H_2O_2 can then, from there, enter other cells and promote oxidative stress intracellularly (*77*). Not only, but H_2O_2 was also found to be the primary microglia-activating ROS, promoting its gain of pro-inflammatory phenotype (*78*). Oxidized by ROS biomolecules can also be recognized as danger associated molecular patterns (DAMPs), further promoting microglia activation (*79*).

PUFA are essential molecules for the brain. PUFA and their metabolites participate in a number of signalling events. N-arachidonoyl-ethanolamine or anandamide (ANA) and 2-arachidonoyl-glycerol (2-AG) are the best known ligands of CB1 and CB2 receptors of the endocannabinoid system (*80*). Endocannabinoid system is majorly involved in neurotransmitter release, synaptic plasticity mechanisms and Ca^{2+} transients regulation (*81*). Both main ligands, referred above, are metabolites of the arachidonic acid (ARA), which is a PUFA. Its susceptibility to oxidation may result in a compromised function of the system, while its metabolism through β-oxidation also generates a rise in ROS production (*82*).

Summing, the brain is both in less and more danger to oxidative stress. While it is endowed with mechanisms for preventing high exposure to ROS under physiological conditions, once it exposed to abnormally high concentrations of ROS it has no means of counteracting it, being extremely vulnerable under these conditions. While the cause and the consequence are not entirely clear, high ROS concentrations were found in Parkinson's disease, Alzheimer's disease, Amyotrophic Lateral Sclerosis and in the ageing brain (*83*, *84*). While the presence of oxidative stress and ROS in the brain is traditionally seen as a secondary damage or consequence, its contribution to these

pathologies should not be overlooked. Hence, it is imperative to deepen our knowledge of the mechanisms of induction and progression of oxidative stress.

1.2. Nanotechnology

1.2.1. Brief history course – diving deep to the very bottom

It is difficult to establish when nanotechnology truly began. First known uses of nanomaterials go as far as 13th-14th centuries BCE (in accordance to some reports, 6th century BCE). Stained glass crafts were found in Egypt and Mesopotamia, whose analysis unveiled the presence of copper, gold, and cuprous oxide nanoparticles in their composition (*85*). One of the most notorious examples of nanomaterials, the Lycurgus cup, is a silver and gold nanoparticle mixture, creating the very first dichroic glass (*86*). Another prominent example is the Damascus steel. Light, elegant and strong enough to cut through armour without losing sharpness, the secret of its success hid in the incorporation of carbon nanotubes in the metal structure (*87*).

The first attempt to understand optical properties of nanoparticles, namely gold nanoparticles, was in 1857 by Michael Faraday (*88*). What he himself called a "summer relaxing study" (*89*), was actually the first attempt to study the infamous "Ruby Gold", which was no other than colloidal gold nanoparticles. He studied the interaction of light with various metals and rightfully concluded that one of the main features of the unique optical properties of colloidal gold was the particle size. Faraday did not take these studies much further and it was not until almost 100 years later that his studies were confirmed and validated by Turkevich and his team (*90*, *91*).

And this leads to another important jump in the nanotechnology field. Nanotechnology could not advance without the means of studying it. There are, to this day, some discussions of what was the cause and what was the consequence, but a decisive advancement for nanotechnology was conferred by the gradual development of techniques and equipment that allowed studies to be precise enough for the study of nanomaterials (**figure 2**).

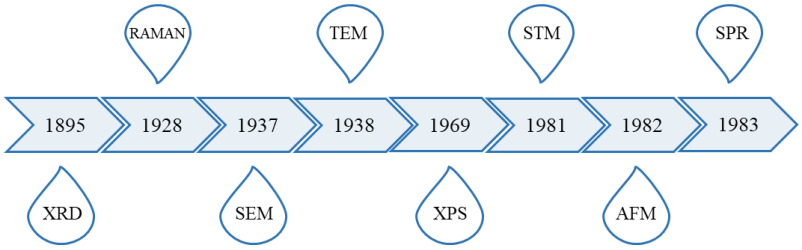

Figure 2: Timeline of technology discoveries that allowed detailed studies and development of nanotechnology (inspired by (92)**).** Abbreviations: XRD – X-ray dispersion; RAMAN – RAMAN spectroscopy; SEM – scanning electron microscopy; TEM – transmission electron microscopy; XPS – X-ray photoelectron spectroscopy; STM – scanning tunnelling microscopy; AFM – atomic force microscopy; SPR – surface plasmon resonance.

The investigation is now accelerating - new methods are being developed and old ones are being improved. Studies of fragile organic nanomaterials, as well as dynamic systems, are still a challenge. Modern equipment allows us to study (for what it seems), a big part of nanoparticle properties. Or maybe not. Maybe there is still a giant discovery behind a closed door for which we do not yet hold the key. The fact is that nanotechnology had, and continues to have, an undeniable impact in science. To some, it is not even considered to be a mere science evolution but a revolution. For the first time, humanity is able to change, and to control, fundamental properties of materials. It is no longer studying and applying what we have in our hands but modifying the very fundamentals of matter and shaping it into what we need.

1.2.2. Nanotechnological approach to science

For those interested in nanotechnology, there are some fundamentals to keep in mind: the difference between nanomaterial, nanoscience, and nanotechnology.

In a brief explanation, nanomaterial is a particle or substance which exists whether humans have interfered with it or not. In order to be considered a nanomaterial, the object must have at least one of its dimensions within the nanoscale, more specifically, no larger than approximately one hundred nanometres. As for nanoparticles, these must have all the dimensions in the nanometre scale. Both organic and inorganic, nanomaterials are widely present in nature, spontaneously occurring. Living beings are able to produce both organic and inorganic (*93–95*) nanomaterials as by-products of their activity. Fully inorganic nanomaterials are also frequent to come by. Formed mostly in nature's own reactors (volcanos, thermal springs, etc.), materials like nanocrystals, carbon nanotubes, metal and metal oxides, quantum dots, can be found anywhere with high or extreme temperatures and

pressure. Usually highly stable, they are easily dissipated through bodies of water and soils, sometimes presenting a health hazard to the biome (*96*, *97*).

Broadly, the term nanoscience can refer to the study any kind of material at the nanometre scale. Observational, structural, and functional studies, microbiology and ecology research, among many others, are directed into studying nanomaterials. However, could it be called a technology if there is no production or manipulation of the material? All of the applications mentioned before were, to our best knowledge, mere observations, and accidental discoveries of some compound property without the understanding of origins of these unique properties. With the invention of the above referred techniques, better understanding of nanomaterials and the nano scale world came and with it also came curiosity. To make use of them, to change them, and to see how far can we adapt or even recreate from scratch what we saw. So, as we speak of learning how to manipulate, fabricate, and make a use of nanoscience, we speak of nanotechnology.

Nanotechnology developed immensely in the last decades and, with it, evolved the understanding of nanotechnology concept. Simplistically, nanofabrication is viewed from two main perspectives where the same material can be obtained by two radially opposite approaches: top-down and bottom-up (**figure 3**). In an analogy, top-down would be comparable to crafting a statue from a solid block of stone while bottom-up is assembling a statue piece by piece, Ikea style.

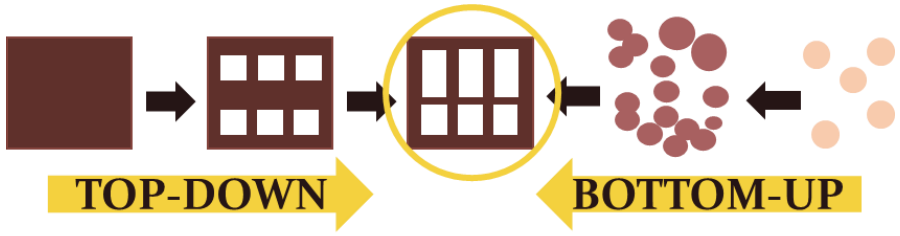

Figure 3: Schematic representation of main approaches of material manipulation at the nanoscale. Simplified representation of how top-down approach reduced the bulk solid material while the bottom up assembles it from the simple atoms or molecules in order to obtain the same type of material.

The top-down is the eldest brother of the two approaches. It relies on the nanoscale manipulation of any sized material and its reduction to the smallest possible size by deletion of unnecessary or not crucially functional parts. Top-down is a more relevant technique in an industrial setting and it usually resorts to lithography

as a go-to method (*98*). Lithographs operate by using photons, electrons or ion beams, imprinting desired patterns on semiconductor surfaces on a micro- or nano-scale (*98–100*) and their main applications consist of production of electronic chips, biosensors and bioelectronics, fluidics and nanowires (*98*, *101*, *102*). Top-down approach offers a very precise and controlled process. However, it is also the product of an older industry. It requires high use of space, machinery, and maintenance. It is not yet a fully sustainable industry. In the run for higher sensitivity and lower scale impact, it has to use high frequency beams that not many materials can withstand (*103*). It is foreseen that, eventually, the bottom up synthesis will dethrone the top down approach.

Bottom-up is a more chemical-oriented synthesis approach. The idea and first advances in this field were owned to the naturally occurring self-organizing processes where, from atoms and simple molecules and their interactions dictated by physical laws, complex structures are formed. The processes of simple molecular assembly (DNA assembly, protein folding) into complex three-dimensional structures are examples of a frequently occurring bottom-up self-assembly phenomenon. Envisioning this example, self-assembly through supramolecular interactions (electrostatic, Van der Waals, hydrophobicity - hydrophilicity interaction, hydrogen bonds, etc.) is the main base for the bottom-up nanofabrication (*104*). The technique allows to construct two- or three-dimensional systems with a large variety of application areas. Starting from assembly of electronic devices (microchips, electrical circuits), passing through fields of inorganic nanotechnology where metal, metal oxide, polymeric nanoparticles, quantum dots, and magnetic and semiconductor metal particles reside, the shifting sands of debated organic nature of carbon nanomaterials, onto a more biological field of organic particles as lipid vesicles such as micelles and liposomes.

Many of the issues that exist in science and technology today can, in theory, be solved by the application of nanotechnology. If optimized, nanofabrication and production can produce much lighter and smaller products with the same functionalities. That would also mean a reduction of costs in prime materials and production, lower demand of heavy machinery and a great space saving, among many other advantages translated in increase of human quality of life (*105*, *106*). However, it also presents its fair share of pushbacks. Nanotechnology is relatively new to the world. To the majority of the population, it is still an abstract concept, taken from sci-fi books, with mini robots running through our veins. Science is fundamentally reliant on the public, on the funding and populational needs. While the premise of nanotechnology is good, the actual situation still reflects high costs and

investments for reduced yield, besides raising a high number of ethical issues of how far is nanotechnology allowed to alter the matter (*107*, *108*). Another existing concern is bringing something new into the ecosystem, the toxicity of nanoparticles and the way the nature will interact with them. While nanoparticles already exist in nature, they are an integral part of it, and were here long before us. The biome has, to some degree, evolved into cohabitating with them. This equilibrium can shift if nanotechnology goes into industrial production. Bioaccumulation is an incredibly pressing issue and it going rogue in not unprecedented. Antibiotics were always existent and naturally produced but it was human activity, the incredible scale up, that created the issue of bioaccumulation and the growing danger of antibiotic resistance. Nanotechnology still lacks systematic studies of long term activity and toxicity effects (*109*). Low toxicities and medicinal applications were shown in extremely controlled laboratory conditions. This will not be the case when assessing the exposure toxicity (*110*). It is also very complicated to predict theoretically the extent of the effect due to high number of variables. Nanoparticle toxicity will be further discussed in the following chapters, but the existent infrastructures are not yet sufficient to effectively evaluate the consequences of nanotechnology development (*105*).

1.2.3. Organic and lipid nanomaterials. Liposomes.

On the most used nanotechnology developments in medicine, natural molecules such as polymers and lipids take the first place. When investigating promising treatment molecules, many are discarded on account of their applicability restrictions such as poor solubility, stability, narrow therapeutic window, low bioavailability, and small half-life, in spite of their beneficial effect. While synthetic drugs can sometimes be manipulated to tune their properties to what is needed, with natural molecules that is much harder to do so. The search for a technology that would overcome these restrictions without losing the therapeutic potential led to the investigation of nanocomposites. Carrier constructs were found to lower the side effects of therapeutic agents, possess unique surface properties, and improve their pharmacokinetics (*111*, *112*). Lipids are a class of molecules that distinguished their ground. They are biocompatible and biodegradable, also making them useful for biomedicine. They are also dynamic, as they spontaneously assemble or disintegrate in specific conditions such as polarity of the solvent, pH or temperature, allowing to personalize these characteristics as drug release control (*113*). Due to their compatibility and closeness to cellular membrane composition, they may interact

better with biological components and membranes, and, that way, possibly augmenting the effectiveness of the drug delivery (*114*, *115*). Due to their compatibility and effectiveness enhancement, lipids are high-ranking on the nanomedicine interest list.

There are many types of lipid uses in nano-biomedicine, distinguishing vesicular lipid systems such as micelles and liposomes and particulate lipid systems such as solid lipid particles and nanostructured lipid carriers (*115*, *116*). Particulate lipid systems consist of fully solid nanoparticles or both solid and liquid forms lipid in the structure that enclose the cargo within themselves, either entrapping it, or solubilizing in the liquid phase lipid (*117–119*)

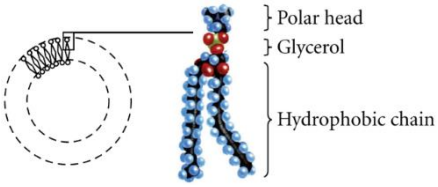

Figure 4: Molecular structure of the liposome membrane adapted from (*127*)

Vesicular lipids make use of the natural tendency of amphipathic lipids to aggregate in a certain manner. Amphipathic lipids are structurally composed of a hydrophilic and a hydrophobic part. In an aqueous solution, these tend to self-aggregate in particles, exposing the hydrophilic part of the molecule and shielding the hydrophobic part inside of the particle. Depending on the external environment and on the lipid type, these can assemble in mono or bi-layers. If they form only monolayered structures, the molecules close on themselves, hiding the hydrophobic tail inside of the sphere. This creates a micelle – a spherical structure with no aqueous media inside (*120*). While micelles possess the beneficial characteristics of lipid particles such as biocompatibility and degradability, they are not as optimal for drug encapsulation. They are usually reduced in size and can only encapsulate hydrophobic compounds. They are also unstable, prone to aggregation, rearrangement and fusion that can result in the premature loss of their cargo and disintegration (*121*, *122*).

Amphipathic lipids can also assemble into a bi-layer membrane. Liposomes were first discovered in mid-60's by Bangham and his colleagues (*123*) and proven to be an efficient drug carriers in the 70's (*124*). They are usually composed of phospholipids: hydrophilic phosphate groups that interact with the exterior and two apolar hydrophobic chains (**figure 4**). Surrounded by aqueous media on the outside, and containing aqueous media inside of the vesicle, the lipid membrane is 2 molecules in thickness – constituted by two lamellae. Hydrophobic forces that drive the membrane formation and the Van der Waals force between hydrocarbon tails maintain and further stabilize the structure. Liposomes are very versatile. When

compared with the other lipid nanoconstructs, these have the advantage of being able to encapsulate both hydrophobic and hydrophilic cargo. While hydrophilic cargo is encapsulated inside of the liposomes that contain an aqueous pocket, hydrophobic molecules find their home entrapped in the liposomal membranes (*125*).

Liposome characteristics and applicability depends on a range of factors: their size, lipid composition and physicochemical properties of these, concentration, temperature, and external environment. Structurally, liposomes vary in sizes and can be distinguished into three main categories accordingly: small vesicles (20-100 nm in diameter), intermediate (100-200 nm) and large (above 200 and up to 1000 nm) and in lamellarity where they can either be unilamellar or multilamellar (*125*, *126*). These differ on the type of cargo they encapsulate and the role they must play pharmacologically. For example, small liposomes are able to encapsulate less of a quantity or reduced in size cargo but can more easily penetrate various tissues and cross biological barriers such as blood vessels. Lamellarity is important for cargo characteristics. Unilamellar vesicles have a larger aqueous pocket and can entrap more hydrophilic molecules, while the multilamellar allow higher encapsulation of lipophilic molecules that need to be entrapped in the membrane (*125*). Liposome size also defines the in vivo behaviour and circulation. For instance, particles larger than 200 nm can activate the human complement system, while particles larger than 150 nm are filtered when passing through the liver (*127*).

The liposome lipid composition is decided in accordance with its functional requirements. Liposome is usually assembled with a main lipid, used in the highest concentration and if necessary, additional lipids can be added in order to finely tune the liposome's structure to the function it is expected to perform. Similarly to biological membranes, produced in the laboratory liposomes often incorporate cholesterol. Cholesterol is responsible for higher organization, rigidity, and stability of the membrane, as well as reducing its permeability and ensuring lower loss of the cargo (*126*, *128*, *129*). By incorporating a charged lipid into the structure, liposomes gain a more accentuated surface charge which will increase their colloidal stability. This can be useful in studies that require charged particles and may even assist on the encapsulation of charged cargo (*127*, *130*, *131*). Depending on the liquid crystalline phase transition temperature of the constituent lipids, when at physiological temperature they can be either in liquid or gel state, which also affects their behaviour and cargo release (*132*, *133*). Depending on the choice of lipids, these can be pH responsive, temperature responsive, redox responsive, and also emerging as magnetic responsive and photo-responsive release. In some cases, liposomes are

adapted for theragnostic purposes by encapsulating active cargo and functionalizing the surface with both antibodies for specific targeting and imaging probes for diagnostical purposes (*113*). By manipulating the liposome overall charge, its behaviour *in vivo* is also altered. Positively charged liposomes appear to have more associated toxicity than neutral and negatively charged ones. Neutral vesicles can circulate for longer periods of time in the bloodstream, while the negatively charged ones are rapidly cleared from the organism, due to liposome interaction with plasma proteins such as opsonins and high- and low-density lipoproteins (*134*, *135*).

One of technical disadvantages of liposomes is their production. It is expensive at industrial scale and traditional optimized methods usually do not yield good encapsulation efficiencies. One of the most used techniques for liposome production is the thin-film rehydration (*136*). It involves the evaporation of a lipid organic solvent and rehydration of these with the aqueous solvent of choice. In a polar solution, lipids aggregate in liposomes which are later treated through a series of processes in order to obtain the needed size and lamellarity (french pressure cell extrusion, freeze and thaw cycles) (*137*) . If the drug to be incapsulated is lipophilic, it is dissolved prior to the solvent evaporation in the lipid solution, while hydrophilic drugs are dissolved in the hydrating solvent. However, the encapsulation efficiency of water-soluble drugs is usually very low : 5% - 15% (*125*) and the non-encapsulated drug has to be removed by dialysis or chromatography. Industrial scale up for such low yield production is usually not profitable. Other active entrapment methods were also developed in order to allow high water-soluble drug encapsulation rates. Such are, for example, pH gradients or ion gradients (*137*) that can assist on high encapsulation rate but are also more costly on equipment and processing steps.

Presently, there is a vast number of liposome-containing formulations that have been approved for human use. These are used in cosmetics, gene therapies and cancer treatments, among others. An extensive list of clinically approved nano-formulated drugs can be found at (*111*, *138*) and many more in clinical trials (*125*). Some interesting studies are also being followed in their development of novel therapeutic agents, such as for example nanoliposomes with the ability to cross blood-brain barrier (BBB) and target the main hallmarks of Alzheimer disease – tau protein and Aβ plaques (*139*) or heat sensitive liposomes targeting specifically HER2-expressing tumours (*140*). While new nanotechnology is gradually catching up to the success liposomes made in the biomedicine field, there is yet much improvement to be made.

1.2.4. Liposome-encapsulated SOD enzyme

SOD, as discussed in 1.1.1.1. is an attractive therapeutic target and many studies were conducted in order to allow its use in medicine. A frequent example is SOD encapsulation in liposomes. The lipid formulation of the liposome is a major factor for an effective encapsulation. Not only it can affect the SOD encapsulation rate, but also its enzymatic activity. Primarily, the encapsulation of hydrophilic SOD is difficult and usually yields very poorly, as it has an affinity for external aqueous solution and tends to diffuse to exterior of the liposome. Many attempts of SOD encapsulation previously failed due to this factor, and many studies later focused on finding an adequate lipid formulation for SOD-containing liposomes. Some physical liposome synthesis methods were found effective, such as submitting liposomes and yet to be encapsulated SOD to freeze and thaw cycles (*57*). The destruction and re-formation of liposomes would promote higher probability of the enzyme encapsulation. Numerous studies also found a drastic encapsulation rate improvement by incorporation of charged lipids into the liposome structure. For once, formulations including stearylamine (SA, cationic lipid), raised encapsulation rate up to 20% when compared to the no SA formulation (*51*, *54*, *55*, *57*, *141*). As superoxide dismutase enzyme has a negative charge, positively charged lipids, due to electrostatic forces, assist on the entrapment of higher concentrations of the enzyme inside of the liposome.

Lipid composition, specially the main lipid (used in the highest concentration) and cholesterol are responsible for the stability of the vesicle. As liposome-encapsulated SOD is produced to target oxidative stress pathologies, the vesicle must itself be resistant to oxidative stress and remain stable in such conditions. Overall, an ideal drug delivery system should allow an efficient way to the drug of interest in high concentrations, to the sought site of delivery and provide a controlled and long-term release of the drug. A previously conducted study also demonstrated that endothelial cells treated with superoxide dismutase and catalase encapsulated inside of liposomes increase the activity of these enzymes 40-fold, when compared to free enzyme treatment (*142*).

1.2.5. Metal and metal oxide nanoparticles: a brave new world

As previously mentioned, metal and metal oxide nanoparticles are the materials that were used since early history and caused a major buzz due to their unique properties at the nanoscale range, very different from the usual bulk materials. Metal nanoparticles are distinguished by the fact they are synthesized from fully metal

precursors, being possible to obtain them by both top down and bottom up approach. Bottom up nanoparticle synthesis, briefly discussed before, when applied to metal and metal oxide nanoparticles, accounts for some of the main production methods. The most well-known technologies are physical and chemical synthesis (*143*). Physical synthesis relies on methods like laser ablation, plasma etching, evaporation-condensation, etc (*143*, *144*). The chemical approach is more based on reduction reactions, pH and ion variations, chemical reactions between precursors and surfactants. Chemical synthesis accounts for methods such as sol-gel, micro-emulsions and thermolysis (*145*). Both approaches are often used in cooperation in order to optimize the synthesis process. Another emerging field is the biological production of nanoparticles. Nanoparticles produced as by-products of organism metabolism are far safer and more sustainable, already offering a considerable range of different nanoparticle compositions (detailed reviews can be found at (*146*, *147*)).

The special interest that science takes in metal nanoparticles is owned by their unique properties, not observed in same composition bulk materials:

a) **High surface area to total volume of the particle.** This affects not only the individual properties of the material but also its interaction with the exterior. Surface atoms have unsaturated bonds which generate free energy and are responsible for nanoparticle interactions, electrical, and enzymatic properties. When modifying the shape of the particle, curvatures and angles are known to concentrate higher amount of these bonds, therefore creating points of higher free surface energy. This affects very significantly the reactivity of the particle and the nature of established interaction, as the higher is the ratio of surface area to the total volume of atoms, the higher the free surface energy the material processes. By this, the size and shape of nanoparticle defines its stability and reactivity (*148–151*).
b) **Surface plasmon resonance (SPR).** As photons (incident light) are oscillatory particles, they have a magnetic field. This field can interact with free electrons on the surface of the metal and force them to also oscillate, creating out-of-phase oscillations. In some cases, if the incident electromagnetic field has the right frequency, stimulation of electrons creates a coordinated group oscillation, that is then called a plasmon. When the plasmons' own electromagnetic field interacts with incident photons which oscillate in the same frequency, the light is scattered. As edges and curvatures accumulate more free electrons, they are also able to produce higher plasmon energy, and

the incident light is accumulated and scattered from few concentrated points, enhancing the generated magnetic field immensely (*152–157*).

c) **Quantum confinement** is a phenomenon describing the number of degrees of the electron momentum. The free and forbidden energies are defined by the interaction of the electron with surrounding particles, protons of the same atom, and neighbouring particles. Now, this liberty can vary in different materials. A bulk material has a theoretical infinite number of liberty degrees, but the more we reduce the structure size, the more we confine the electrons' motion to very restricted, narrow, and tailored levels, called a quantum boxes. Although, theoretically, this happens to any dimension charge, scientists can only significantly grasp the effect of quantum confinement when the material contains between hundreds to thousands of atoms. In these cases, the gap between ground and excited states grows, and levels themselves narrow down to very specific energies. Quantum confinement is usually spoken when speaking of SPR, as it has the ability to amplify the signal, as the more energy is needed to excite an electron, the more energy it will release once it returns to the ground state (*158*). The strict control of energy levels in materials by varying their size also allows for strict control of the optical and electronical properties of this material (*159–162*).

Magnetism, although not a factor like the above, is a prospective property that many metal and metal oxide nanoparticles possess. Due to their small dimensions, the amount of magnetic domains in a particle is reduced and easily aligned to an external magnetic field (*163*). By applying the external magnetic field, it is possible to control nanoparticle orientation, motility, and temperature as they release the energy in the form of heat, and can reach very high temperatures in a very low spatial range (*163*, *164*). In biomedicine, para- and super paramagnetic nanoparticles are already widely explored in magnetic resonance diagnostics (*165–167*), and are starting to gain more use in hyperthermia treatments (*164*, *168*) and in controlled release drug delivery (*169*, *170*).

The use of nanotechnology in everyday life is much more frequent then many people would assume (*171*). Titanium and zinc oxides are widely used in cleaning, disinfection, and UV protection (both textiles and cosmetics) (*172*, *173*). Photocatalysts are used in paints, coatings, and photovoltaic cells. Metal nanoparticles are also found in waterproofing, lubrication, environmental sensors, and finally biomedicine. Medicine already uses nanoparticles in dentistry, tissue regeneration, sensors, drug delivery, amongst many others. Noble metals, and silver in particular, showed

mesmerizing anti-bacterial, -microbial and -viral activity with low to no toxicity. Transition metals, both pure and oxides are being heavily explored due to high enzymatic and electro-opto-magnetic activities. Quantum dots and more recently carbon dots are being explored as amazing sensors and imaging devices (detailed reviews can be found at (*174–176*). Overall, the "to do" list still has too many point left unchecked, a fact that can be seen as a promising to many new grounds to explore.

1.2.6. Metal nanoparticles-associated toxicity – every fairy-tale needs a villain

One of the obstacles of studying the nanoparticle-associated toxicity is that their activity is extremely dependent on their physical characteristics. The previously mentioned characteristics that define nanoparticle properties are the ones that are also determinant variables in nanoparticle-induced toxicity. As the scale is extremely low, even alterations of few nanometres, in size or shape, can modify, either by amplifying or mitigating the organism's response to the exposure. That makes theoretical predictions of the toxicity very difficult (*177*). When, for example, varying the size of the particle, smaller sizes can diffuse more easily and also penetrate the cells and subcellular compartments with higher ease, where they can have higher associated toxicity (*178*). Other factors include surface charge, geometry, solubility and particle composition (*179*, *180*). Nanoparticle geometry can differentially affect its interaction with cells and it also majorly affects the uptake route (*181*, *182*). Charge defines the way particles may interact with the cellular environment and cells themselves, also influencing the uptake of nanoparticles. Composition affects the nanoparticle activity and biocompatibility. It also determines its lifetime, as deuterating in free elements particles can influence very significantly the cellular response and viability. Prediction of nanoparticle toxicity is also complicated by the fact that not all factors vary linearly - a interesting representative study of this can be found at (*183*).

When studied *in vitro*, mechanisms on nanoparticle toxicity are mainly mediated through particle degradation and release of free elemental compounds, oxidative stress, and membrane damage (*179*, *184*). Particle degradation is very dependent on the intended use. Factors involving the particle itself can account for the composition, crystallinity for metal oxides, size, and structure defects. The solvent also plays an important role, whether it is simple aqueous buffer solution or complex cell medium, pH of the solvent, presence of growth factors, free ions, etc., that can influence the particle stability (*185*). As an example, quantum dots constituted by

cadmium and zinc (CdSe/ZnSe), can degrade in aqueous media, releasing free cadmium that is toxic to cells (*186*). Free ions such as iron and copper can also inactivate some metalloproteins by interacting and dislodging the metallic core (*187*). Nanoparticles can also catalyse the production of reactive oxygen species or/and destabilize the cell, invoking oxidative stress and increase of ROS produced by the cells. This can contribute to DNA damage (genotoxicity) (*188–190*), and protein and lipid peroxidation (*2*, *27*, *34*, *191*). Not only that, but some nanoparticles are known to cause a decrease in mitochondrial membrane potential, impairments in transport chain and activation of NADPH system (*192*, *193*). Membrane damage can be inflicted by both physical (rough angular surface of the nanoparticle can inflict damage and if uptaken damage the organelles) and chemical (lipid peroxidation, membrane depolarization) characteristics (*180*, *184*, *194*). Nanoparticle-caused cytotoxicity can also be of a more indirect nature, such as modifying gene expression (*195–197*) and causing a cell cycle arrest, or even triggering inflammatory response (*198*). Some nanoparticles can also modify cell signalling in unexpected ways (*199*, *200*). They were shown to increase influx of extracellular Ca^{2+}, causing perturbation of cellular Ca^{2+} homeostasis (*201*). For a reason, to this day, metal nanoparticles are the most frequently used for the treatment of tumours where the targeted toxicity can be used for a beneficial end (*202*).

While *in vitro* testing may be able to predict immediate cell responses, it is unable to provide information about the overall organism response to nanoparticle presence. The mechanisms described before mostly focus on cell specific mechanisms, and the effect on a large scale can be seen in a different way. For example, while for any particular intended use of nanoparticle its charge or size may not be important, these factors can affect the way the particles will behave within the system, affecting their excretion (*203*) or interaction with biomolecules (*200*). Nanoparticle distribution in the body depends majorly on the administration route and the constituent material of the particle, however, the most frequent places of accumulation are the liver, kidneys, spleen and somewhat the heart and lungs. Some nanoparticles can also cross the BBB and accumulate in brain tissue (*200*, *204–206*).

Toxicological data extracted from cell line tests can contradict the results when applied to more advanced models. Carcinoma cell line were previously studied to show a very different pathophysiology from normal *in vitro* cells, by that not complicating only the *in vitro* to *in vivo* transition but even only cell studies transitions (*207–209*). The nanoparticle activity and toxicity mechanisms must be studied further, constructing a more extensive network of data and possible correlations. Complete

study models, including both cellular and *in vivo* models, are also crucial for a correct estimate of the nanoparticle toxicity (*207*, *210*).

1.2.7. Manganese oxide nanoflowers

Manganese (Mn) is a heavy metal abundantly found in nature, mostly in earth crust, soils and sometimes water (*211*). When it comes to abundancy, it is only second to iron when considering the transition metals. In biological organisms, manganese is found only in trace amounts. Mn excess in organism is called manganism and it is symptomatically similar to parkinsonism (*212*, *213*). Elemental manganese has the capacity to cross the BBB and accumulate in brain tissues, mostly basal ganglia (*214*), causing oxidative stress, activation of microglia and astrocytes (*215–219*), motor disturbances and cognitive impairment (*212*, *220*).

While the Mn excess can be a dangerous pathology, a trace amount if it is crucial for the functioning of biological systems. An adult human body contains around 10-20 mg of Mn (*221*). Due to its abundance and consistent presence in the ecosystem, organisms evolved into incorporating Mn as protein and enzyme cofactors or/and activating ions. Some of the most prominent examples of Mn dependent enzymes are antioxidant mitochondrial superoxide dismutase and acetylcholine esterase that play an important role in protecting against oxidative stress. Many other enzymes also require manganese cofactor, such as glutamine synthetases, arginases and pyruvate carboxylases. Some bacterial strains also have manganese-requiring catalases (*222*). Overall, a large number of proteins and enzymes of all classes depend on the manganese cofactors (*223*, *224*). Oxidation state is an important factor for metalloproteins. While manganese has various oxidation states, the 2+ is the most stable and constitutes the core of unactive metalloproteins (*13*). Other recurring and biologically important oxidation states are 3+ and 4+ and sometimes 5+ (*221*, *225*) that, due to lower stability, react enthusiastically with other molecules, in order to be reduced back to the most stable state (*13*). Both 3+ and 4+ manganese oxidation states are also important for superoxide dismutase and catalase enzymes, gaining a significant biological importance in terms of antioxidant activity (*13*).

Due to the active involvement of manganese in the antioxidant defences of organisms, it is one of the elements that gained an increasing interest in leading research facilities. As aging and neurodegenerative disorders have been associated with an increase in oxidative stress and insufficient clearance of ROS, this was one of the first targets of research. O_2^- level rise is usually related to mitochondrial

dysfunction and compromised mitochondrial superoxide dismutase levels. As for the treatment, mitochondrial SOD is a Mn metal centre enzyme and s manganese was investigated in the context of creating artificial superoxide dismutase enzyme substitutes. Firstly, biological complexes were explored, such as chelating scaffolds for Mn ion. Some of the most notable ones were Mn salen complexes (*226–228*), Mn porphyrins (*229*, *230*) and Mn cyclic polyamines and polyamine-polycarboxylates (*231–235*). These complexes tend to be more stable, biocompatible, behaviourally similar to biological antioxidant enzymes, and many of them, mostly Mn-salen complexes, show multi-enzymatic activities (*228*). However, they are also susceptible to biological enzymes weaknesses, as they require specific environments to properly function and are degraded over time. Harsh environments and incorporation into more complex structures may still be a challenge. On the other hand, manganese nanoparticles were also closely studied on the topic of enzymatic activity. Amongst many, they show some of the most complex structural and magnetic (*236*, *237*) properties due to the nature of structures and bonds they form. These are more applied in industrial settings (such as clearance of water and industrial contaminations (*238*), electro-sensors and -catalysts, supercapacitors (*239*) and chemical catalysts (*240*)), manganese and manganese oxides also slowly found their way into biomedicine. Nanocrystalline manganese oxides were also a fruitful field for investigation. They present both a large number of synthesis pathways (*241*) and of compositional variants, yielding in MnO (*242*), MnO_2 (*243*), Mn_2O_3 (*244*), Mn_3O_4 (*244–247*) and Mn_5O_8 (*249*) nanocrystals. The oxidation state and, therefore the crystalline structure of the manganese oxide is largely dependent on the synthesis conditions, one of the most used methods being calcination in air or inert atmosphere, but also accounting for methods like co-precipitation, sol-gel, hydrothermal/solvothermal, etc. Hausmannite (Mn_3O_4) nanoparticles are already used in oxidation of methane and carbon monoxides (*250*), reduction of nitrobenzene to nitrosobenzene (*251*) and degradation of organic pollutants in water (*252*, *253*).

When it comes to biological antioxidant capacity of manganese oxide nanoparticles, hausmannite particles showed the best performance, displaying high capacity of SOD, catalase, and glutathione peroxidase activity mimicry. They present a mix of Mn 2+ and 3+ oxidation states that confers them a higher chemical versatility and a very particular tetragonal crystalline structure (**figure 5**). It was

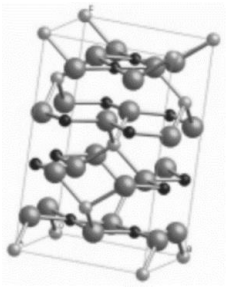

Figure 5: Crystalline structure of hausmannite (Mn_3O_4) manganese oxide particles reproduced with the permission of (*339*).

also reported to form a variety of nanoparticle forms, where the synthesis can yield either in manganese oxide solid particles, such as cubes, rods, polyhedrons, etc., or single 1D nanocrystals that can later in the process agglomerate into forming “spiky” structures of single crystals. Different laboratories attributed them different names, such as honeycomb nanospheres (*254*) or nanoflowers (*246–248*). When compared with other obtained geometries (cubes, polyhedrons, hexagonal plates, and flakes), the nanoflower showed both multi-enzymatic activity and higher rates of substrate conversion (higher enzymatic activity) (*248*). The tendency for higher SOD-like activity in relation to CAT/GPx-like activities depended on the oxidation state of the nanoparticles. Higher oxidized content of manganese in manganese oxide (Mn_3O_4) nanoflowers exhibited preference towards CAT/GPx-like activity while reduced state showed higher SOD-like activity (*247*). Cyclic voltammetry of nanoflowers showed a much higher current capacity when compared to other geometries, further confirming the higher enzymatic activity capacity, already seen by enzymatic assays. Accentuated activity is mainly attributed to the very high surface area/total volume ratio of crystals, while the multi-enzymatic phenomena to higher porosity of the given structure, possibly creating more adequate environment to accommodate substrates (*247*). Nanoflowers also exhibited biological enzyme-like kinetics and significant activity at concentrations as low as 10-50 ng/mL (*248*). In cell studies, they showed cytoprotective effect against H_2O_2 (*246*) and 1-methyl-4-phenylpyridinium (MPP+) (*247*) neurotoxin, without interfering with natural antioxidant balance of the cell or nitic oxide bioavailability (*248*).

1.3. Synthetic biology and cell mimicry

Synthetic biology is when engineers get their hands on biology. It relies on the modification of biological systems to fit the required needs. Most synthetic biology research started and continued relaying heavily on the manipulation of cell DNA (*255*, *256*). What started with recombinant DNA, culminated in the later years with CRISPR-Cas9 technology, an efficient way to control and modify genetic expression of organisms (*257*). Drug delivery systems (*258*), protective coatings for biomolecules and modification of protein structures and folding (*53*, *259*) to adapt to specific required action are other examples of this research field. Overall, synthetic biology research stands on three mains principles: study of biological processes, biological modelling (both computational and experimental biology) and finally the construction of engineered systems (*260*).

Cell mimicry and artificial cells are a relatively young topic in research and as so, the term encompasses a spectrum of definitions. Cell mimicry as biomedicine main target is to develop a supporting system for biological cells, to compensate for loss of functions (*261*). As an independent research field, it is also a term used for the creation of complex artificial systems that aim to replicate of some of the cells biological functions, such as accommodating respiratory chains or enzymatic pathways (*262*, *263*). Cell mimicry can be approached by the top down method, that envisions cell mimicry as encapsulation or entrapment of entire cells or specifically isolated organelles or vesicles and their posterior use (*264*, *265*). and bottom-up, the assembly of structures from the molecular building blocks (*266*). While top down has the advantage of using already living cells and being able to make use of intricate metabolic pathways and self-regulating systems, it offers less control over the exact nature and activity of a produced structure. Bottom up, once again, is far more promising as it allows a highly controlled production, which is tunable to the needs of each system, but that is very limited to the lack of knowledge and by the fact the that inanimate/living barrier has not yet been broken.

1.3.1. Up the ladder: artificial enzymes, organelles, and cells.

Functional nanocomposites, incorporation of modified natural molecules and inorganic mimetics and, above all, cell mimicry are a newer and advanced field in nanotechnology. When assembling artificial biological systems, three main categories can be distinguished: artificial enzymes or so called nanozymes, artificial organelles and artificial cells.

Natural enzymes are the basis of living beings. However, when they fail, the simple addition of the same external enzyme is often not a viable treatment. Enzymes, as most of biological molecules, are sensitive to the environment, and easily lose their activity and are degraded by the organism (*267*). They have low targeting capacity and circulating half-life. Therapeutic drugs using natural enzymes are extremely high in cost of production and proper storage, whilst frequently having low long term stability (*267*). In order to solve this issue, researchers invested in finding alternatives for these enzymes. Artificial enzymes included the modifications of natural enzymes, while nanozymes, a more advanced term is applied to novel synthetically constructed biomolecules or use of inorganic materials as enzyme' catalytic substitutes. Enzyme-targeted synthetic biology invested in modification of naturally existing enzymes, artificial incorporation of metallic cofactors into biomolecules, enzymatically active

biofilms and coatings, and usage of inorganic materials with catalytic abilities, such as metal and metal oxide nanoparticles (*268–270*).

An artificial organelle is a step up from the artificial enzymes. It encompasses a construction of a structure with a specific activity that is usually attributed to a living cell. Vesicles with genetic machinery, capsules with metabolic pathways or the use of enzymes are all examples of artificial organelles. When increasing the complexity to organelles, the question of molecular crowding and compartmentalization arises (*271*). Each component has a specific time and space frame for function and interaction with the rest of the system. The most successful organelle replicates to this moment account for liposomes, polymerosomes, capsosomes or vesosomes with the ability to encapsulate active cargo and penetrate into the cell, exhibiting its activity (*272*), as they allow spatial and chemical environment control over the cargo.

Artificial cell is the most complex structure of the enumerated above. It envisions the use of multiple complexes in a hierarchical manner, incorporating active cargoes, organelles, multiple structures with an ability of dynamic interaction and communication. For as simple as it sounds, artificial organelles and artificial cells also differ in size and the intended spatial activity. While an organelle is intended to be incorporated into a living cell structure, performing its designated functions, an artificial cell is an extracellular system, required to have a higher degree of complexity and autonomy. A true artificial cell, due to its complexity, is still not reproducible, however, scientists have developed the concept of “minimal cell” for cell mimicry studies. Minimal cell is an idea of composite incorporating one or more specific functions of a living cells (*273*, *274*). This can be anything considered necessary, starting from gene expression mechanisms (*275*), enzymatic reactions (*276–279*), and inflammatory signalling and to the constructions of respiratory chains.

The most complicated point in cell mimicry is not the replication of a static construct identical to a cell. It is its dynamics. Its functional complexity has made the replication of a living cell impossible to this day. However, it can be used to the advantage of science. Biological cells *ex vivo* used for molecular studies are very fragile and inconsistent with their response. While these are not as complex as *in vivo* models, and often do not replicate the true response, simultaneously their inherent individual complexity can interfere with a study targeting a specific metabolic pathway or circuit. The creation of an artificial construct able to replicate a specific biological function, being restricting it to that function only, could be beneficial for more precise molecular studies (*280*).

1.3.2. Layer-by layer deposition

Nanofabrication of complex multi-layered structures often resorts to layer-by-layer (LbL) assembly approach. As the assembly of both artificial organelles and cells is usually reliant of higher complexity structures with different components, LbL is frequently used as the most convenient deposition technique. While there are other assembly methods, such as Langmuit-Blodgett (based on Van der Waals interactions) and self-assembled monolayers (SAMs – thiol monolayers deposition), these are regarded as frequently limited by lower stability, robustness of the structures and interlayer interactions, and need for specific films or compound in order to assemble correctly, in this way limiting the produced variability of materials (*281*). LbL is, in its turn, inexpensive, easily replicated, and versatile method that allows efficient modification of surfaces, accounting for several types of interactions and versatility in film compositional characteristics. There are also variations on the typical LbL deposition of passive layered films on a solid surface. Spin LbL assembly, imprinting assisted LbL, electromagnetic assembly, hydrodynamic deposition, pattern creating with lithography, and LbL deposition on spherical particles are all variations of a traditional method, often having as an aim to augment the efficiency and specificity of the deposition, creating higher complexity and improved process control structures (*281*–*284*).

The main practical theory behind LbL deposition is the adsorption of molecules to an assembly surface by any of the later discussed interactions. Sequential deposition of films requires washing steps in between them with water or aqueous buffers. This way, the excess of the previous coating is removed from the solution and the wated is adsorbed onto the surface, preventing further unrequired deposition, and stabilizing the previous layer (*284*). LbL can be performed at any type of surface and biomolecules, as long as it is capable of establishing the interaction that is held as the basis for that assembly. The method allows a high level of flexibility on the layer interaction. These can be electrostatic, covalent bonding, hydrogen bonding, hydrophilic/hydrophobic interactions, and more complex interactions such as protein-protein, antibody-antigen, glycans and their receptors and finally nanotechnologists favourite – DNA (detailed reviews can be found at (*281*, *282*)).

While LbL is a useful technique to assemble a number of particles, it also presents some disadvantages to its use. Poor colloidal stability and drug loading, low level of controlled encapsulation, release, and specific interaction with cells, and finally a low protocol yield that is barely scalable (*285*). As the layering process occurs step by

step, at each time, needing time for each deposition and requiring an excess of the deposited material, it can also rapidly become highly time and material consumable in highly complex structures composed with a variety of levels and biomolecule variations.

1.3.3. Microreactors and astrosomes

While the artificial cell research has been rapidly advancing, there is still a low amount of studies to cover all biological systems. As an example, studies involving CNS usually have in focus neurons as the main players, leaving the other components largely unexplored. For instance, while astrocytes, the main gatekeepers of brain homeostasis, account for some interesting technology studies of computational artificial networks (*286*–*288*), the practical applications are not yet largely investigated as a perspective for efficient artificial cell mimicry application. However, it is not a complete radio silence. An interesting series of research was done by Armada-Moreira *et al* on the development of artificial cells targeting the prevention of excitotoxicity – job typically performed by the astrocytes (*289*, *290*). Two generations of microreactors were reported to mimic astrocytic function in the prevention of excitotoxicity in cells. While first generation of microreactors included only platinum nanoparticles as the active principle, they were reported to be able to scavenge both H_2O_2 and ammonia (NH_4^+), and exhibited a cytoprotective effect on neuroblastoma cell line (*277*). They were able to prevent to some degree the cellular death promoted by the presence of H_2O_2 and NH_4^+. Second generation microreactors showed an already enhanced experimental design, including both platinum nanoparticles and liposome-encapsulated glutamate dehydrogenase and glutathione reductase (*279*). The enhanced complexity of the microreactor not only revealed an improvement in the astrocyte mimicry development, but also showed better cytoprotective effect on primary neuronal cultures, rescuing cell viability from H_2O_2 and NH_4^+ induced toxicity, and also normalizing neuronal signalling.

1.4. Scientific aims

The main goal of this work was to design and develop a novel microreactor system mimicking antioxidant mechanisms of the cell in a response to chronic inflammatory reaction in the CNS. By applying nanotechnology bottom up approach, microreactors were assembled layer-by-layer into a multilevel structure incorporating liposome encapsulated SOD enzyme and Mn_3O_4 nanoflowers. Both active components are targeted into scavenging ROS and exhibiting cytoprotective action of cell´ natural antioxidant defences against inflammation induced oxidative stress.

Accordingly, the following specific aims were pursued:

1. **Synthesis and characterization of Mn_3O_4 nanoflowers.** Physical characterization was achieved by scanning and transmission electron microscopy (SEM and TEM), dynamic light scattering and ζ-potential. Assessment and characterization of enzyme-like activity by enzymatic assays in free solution.
2. **Synthesis of SOD-containing liposomes.** Optimization of lipid composition and characterization of the structures by dynamic light scattering and ζ-potential. Liposome-entrapped enzyme activity assessment in free solution by enzymatic assays.
3. **Assembly of the microreactors containing Mn nanoparticles and liposome-entrapped SOD.** Structure characterization and deposition control by SEM, TEM, fluorescence microscopy and ζ-potential. Assessment of SOD-like and CAT-like activity of microreactors in free solution.
4. **Assessment of liposome, nanoparticle and microreactor integration and cytotoxicity in SH-SY5Y neuroblastoma cell line.**
5. **Assessment of nanoparticle and microreactor integration and cytotoxicity in mixed primary cultures.**
6. **Evaluation of reactive oxygen species scavenging capacity of microreactors in SH-SY5Y neuroblastoma cell line and primary mixed cell cultures.**

2. Methods

2.1. Reagents and Materials

Nanofabrication: potassium permanganate ($KMnO_4$), oleic acid ≥ 99% (GC), absolute ethanol, superoxide dismutase from bovine erythrocytes (SOD, EC 1.15.1.1, ≥ 3000 U/mg), dopamine hydrochloride (DA), poly(L-lysine) (PLL, MW 40000–70 000 Da), 4-(2-hydroxyethyl) piperazine-1-ethanesulfonic acid) (HEPES), stearylamine (SA) were purchased from Sigma-Aldrich (St. Louis, MO, USA). Dipalmitoylphosphatidylcholine (DPPC) and cholesterol were purchased from Avanti Polar Lipids (Alabaster, AL, USA). Polystyrene (PS) particles (7.06 µm in diameter) were acquired from Microparticles GmbH (Berlin, Germany). Poly(methacrylic acid)-*co*-cholesteryl methacrylate (PMAc) was synthesized in house, according to a previously published protocol (*291*).

Cell cultures: Hank's balanced saline solution (HBSS), fetal bovine serum (FBS), Neurobasal medium, Opti-MEM medium, DMEM/F-12 GlutaMAX™ supplement medium, penicillin-streptomycin (10 000 U/mL), L-glutamine (200 mmol), B-27 (50x), gentamycin (50 mg/mL), trypsin-EDTA (0.025%, no phenol red), were purchased from Thermo Fisher Scientific (Waltham, MA, USA).

Others: SOD Assay Kit, glycine, paraformaldehyde (PFA), bovine serum albumin (BSA), Triton X-100, hydrogen peroxide (H_2O_2, 30% w/w), paraquat, dihydroethidium (DHE), lipopolysaccharides from *Escherichia coli* O55:B5 (LPS) were purchased from Sigma-Aldrich (St. Louis, MO, USA). Amplex UltraRed was purchased from Thermo Fisher Scientific (Waltham, MA, USA). Cell counting kit 8 (CCK-8) was obtained from Dojindo EU GmbH (Munich, Germany). Complete Mini, EDTA-free protease inhibitor cocktail was purchased from Roche Diagnostics, Germany.

Buffer solutions: phosphate buffer (0.2 M, pH 7.4), phosphate buffered saline 1x (PBS 1x 0.14 M NaCl, 27 mM KCl, 18 mM KH_2PO_4, 10 mM Na_2HPO_4, pH 7.4) and PBS 10x(1.4 M NaCl, 2.7 mM KCl, 1.8 mM KH_2PO_4, 0.1 M Na_2HPO_4 pH 7.4), Tris buffer (10 mM Tris base, pH 8.5), HEPES low ionic strength solution (10 mM HEPES, pH 7.3), HEPES-saline solution (20 mM HEPES, 120 mM NaCl, pH 7.3).

2.2. Nanofabrication

2.2.1. Manganese oxide nanoflower synthesis.

The presented protocol is an adapted version of previously described manganese oxide nanoflower synthesis (*254*, *292*). In order to synthetize manganese oxide nanoparticles, 6.4 mmol of KMn_3O_4 were dissolved in 500 mL of MiliQ water and stirred vigorously for 30 minutes. Then, 10 mL of oleic acid were added in continuous flux of 0.25 mL/min while the solution was stirred at 60°C. The stirring was performed for about 5 hours, until a dark emulsion in the oil phase was formed. The emulsion was later isolated and washed 1x with absolute ethanol in order to precipitate, 3x in MiliQ water and 3x in absolute ethanol. Isolated precipitate was then dried for 10h at 80°C and calcinated under normal atmosphere at 200°C for 5h. The obtained powder was resuspended in pretended buffer to 2 mg/mL and sonicated for 3 pulses.

2.2.2. Superoxide dismutase-containing liposome synthesis.

In order to produce functional uniform and unilamellar liposomes, a previously described protocol was used and adapted to the experimental requirement (*57*). Liposomes were synthesized with the following lipidic composition: DPPC:Chol:SA (6:3:1, wt.%) and DPPC:Chol (7:3, wt.%). Lipid stock solutions were prepared in 25 mg/mL concentration and mixed in pretended ratio immediately before the synthesis.

Obtained lipid mixture solution was dried with a rotary evaporator at 300 mbar at RT for about 15 minutes, until no liquid residue could be observed and then further dried in vacuum for 2h. The lipid film was later rehydrated with HEPES-saline buffer at 65°C for 2h, with occasional vortex agitation. Resuspension volume is variable with a pretended final lipid concentration of 2.5 mg/mL. After the rehydration, the solution was submitted to four freeze and thaw cycles (10 min at -196°C and 10 min at 65°C) and extrusion through a 200 nm membrane on a metal plate warmed to 60°C, above the lipid melting temperature, 23 times in order to form unilamellar and uniform empty liposomes. The SOD enzyme (500 U/mL) was then added to the solution and submitted to two more freeze and thaw cycles (10 min at -196°C and 10 min at 65°C) and followed with one more extrusion through a 200 nm membrane. The non-encapsulated enzyme was separated by size exclusion chromatography.

2.2.3. Microreactor assembly

Microreactors were assembled by the layer-by-layer deposition technique, layering active components and inert polymers based on electrostatic and chemical attraction between the layers. The procedure was previously developed and described (*277*, *293*). Polystyrene (PS) beads with a diameter of 7 µm were used as core for the assembly. The volume of used reagents is equal to the volume of polystyrene particles used in the beginning. Initial solution of PS particles was washed 3x with Tris buffer pH 8.5 (1800 rpm, 45 sec) and incubated with dopamine (DA) solution (2.5 mg/mL in Tris buffer pH 8.5) for 3 hours. The polymerization could be observed by the change of colour, as the polydopamine (PDA) gains a dark translucent colour. From this step on, the reactors were washed 3x with HEPES-saline buffer (1800 rpm 45 sec) in between every step, unless stated otherwise. After washing the excess PDA, microreactors were incubated with poly-L-lysine (PLL, 1 mg/mL) for 10 min and later with previously synthesised liposomes for 40 min. Next layer was obtained by incubation of microreactors with poly(methacrylic acid)-*co*-(cholesteryl methacrylate) (PMAc, 2 mg/mL) for 10 min. Assembly was then followed by PLL (1 mg/mL) for 10 min, Mn_3O_2 nanoflowers (0.5 mg/mL) for 20 min and once again PLL (1 mg/mL) for 10 min. Microreactors were coated with another liposome layer for 40 min and PMAc for 10 min. After PMAc incubation, microreactors were washed 3x with Tris buffer pH 8.5 (1800 rpm, 45 sec) and incubated with finishing layer of DA solution (2.5 mg/mL) overnight. The next day microreactors were washed 3x with HEPES-saline buffer (1800 rpm, 45 sec) and stored for posterior use at 4°C.

For microreactors containing only nanoflowers, the assembly protocol is identical, excluding the steps related to liposomes. Initial solution of PS particles was washed with Tris Buffer pH 8.5 3x (1800 rpm, 45 sec) and incubated with dopamine (DA) solution for 3 hours. Next PLL (1 mg/mL) for 10 min, NP (0.5 mg/mL) for 20 min and PLL (1 mg/mL), 10 min were layered in the exact order, always with 3x intermediate washes with phosphate buffer 0.2 M pH 7.4. Particles were incubated with DA solution (2.5 mg/mL in Tris buffer pH 8.5) overnight. The following day fully assembled microreactors were washed with phosphate buffer 0.2 M pH 7.4 (3x, 1800 rpm, 45 sec) and stored at 4°C for posterior use.

2.2.4. Determination of microreactor concentration

A small sample of finished microreactors was diluted in a range 1:100 to 1:250, depending on the initial amount of PS particles and solution concentration, in the buffer used to maintain microreactors (HEPES-Saline or phosphate buffer 0.2 M). From the diluted solution, 1 µL was pipetted to a glass slide in a triplicate from different regions of the sample (top, middle, and bottom portion) and observed under brightfield of inverted widefield Zeiss Axiovert 200 microscope (Carl Zeiss Inc., Germany). The images were acquired by AxioVision 4 (Carl Zeiss Inc.) software. The photo of triplicates is taken with the 5x objective and the microreactors are counted manually in each sample. The microreactor solution concentration is calculated by multiplying the mean number of reactors in a microliter by the dilution factor and total available volume of microreactors.

2.2.5. Physical characterization of synthesized materials

The particle size, size distribution and ζ-potential of the liposomes, nanoparticles and microreactors were measured by Zetasizer Nano ZS (Malvern Instruments, UK), using a dispersant refractive index of 1.450. Sample size distribution was measured by dynamic light scattering (DLS) and the surface charge by ζ-potential. Before the measurement, sample was diluted in an adequate buffer (HEPES 10mM buffer for liposomes and microreactors and phosphate buffer 0.2 M buffer for Mn_3O_2 nanoflowers) at 1:20 ratio.

2.2.6. Deposition control

In order to confirm their correct assembly, microreactors were analysed after each layering step. Polymer coatings were measured via surface ζ-potential of the reactor after each layering step as it is, in theory, reflective of the charge of the outer layer (last deposited polymer). During the synthesis of microreactor, following each step 50 µL of sample was collected to have a sample for each used polymer as the outer layer. Samples were resuspended in 950 µL of HEPES 10 mM buffer and the charge was measured via ζ-potential.

Liposome deposition was verified by fluorescent dye di-8-ANEPPS (4-[2-[6-(Dioctylamino)-2-naphthalenyl]ethenyl]-1-(3-sulfopropyl)-pyridinium, inner salt). A sample of microreactors was isolated after depositing the first layers of liposomes, the second, and after fully assembling the microreactors. A small aliquot was incubated

with 10 μM di-8-ANEPPS and left to bind for 10-15 minutes protected from light. Afterwards, a small droplet on a glass slide was observed under an inverted widefield Zeiss Axiovert 200 microscope (Carl Zeiss Inc., Germany) at 40x amplification with 567 nm emission filter.

2.2.7. Electron Microscopy

Manganese oxide nanoflower deposition was confirmed by Scanning Electron Microscopy (SEM) and Transmission Electron Microscopy (TEM). For TEM, a sample of microreactors was isolated before and after the nanoparticle deposition step. The sample was deposited on a copper grid with no further staining and observed by the transmission electron microscope (Hitachi H-7650).

SEM was performed in collaboration with Dr. Brigitte Städler by Miguel A. Ramos-Docampo in Laboratory for Cell Mimicry in Interdisciplinary Nanoscience Center, Denmark. Shortly, the samples were deposited on silicon wafers, allowed to dry and coated with a thin layer of platinum (6 nm). Scanning electron microscopy (SEM) images of the nanoflowers and microreactors were taken with a FE-SEM from FEI (Nova-600), operating at 5 kV with a working distance of 5 mm.

2.2.8. Superoxide dismutase activity assay

Superoxide dismutase activity assay is a commercially available assay kit from Sigma Aldrich. This assay has a colorimetric principle and relies on xanthine and xanthine oxidase to produce the O_2^- in a solution and the formation of WST-1 (tetrazolium salt) formazan dye upon reduction of the WST-1 by the O_2^-. Formazan dye has an absorption spectrum in the wavelength of visible light, with the maximum at approximately 440-450 nm. In the presence of superoxide dismutase enzyme, or a material with a superoxide dismutase-like activity, O_2^- will be converted into oxygen and hydrogen peroxide, preventing the formation of the dye.

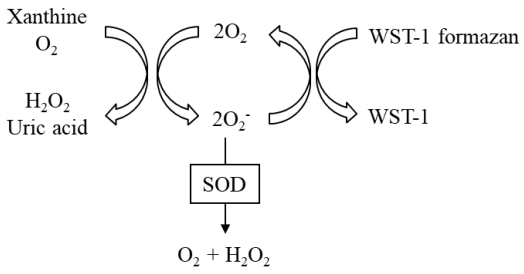

The assay was performed in a 96 well plate and the reaction mix was prepared directly in the well. Two controls were made: a negative control in which no SOD or SOD-like material nor O_2^- producing mix was added and a positive control, with the complete reaction mix and no SOD activity material. For each nanoparticle and microreactor assay, a separate control was made in order to exclude the colour

present in the solution. The plate with running assay was incubated for 20 min at 37°C. The absorbance was read at 450 nm, with a microplate reader TECAN Infinite M200 (TECAN, Switzerland)

2.2.9. AmplexRed H_2O_2 assay

Catalase like activity of nanomaterials was accessed by the AmplexRed assay, commercially available from Sigma. Briefly, the assay relies on the reaction of H_2O_2 with AmplexRed reagent (10-acetyl-3,7-dihydroxyphenoxazine), which in the presence of horseradish peroxidase form a fluorescent compound resorufin. Samples of nanoflowers and microreactors were left to react with 400 µM of H_2O_2 for 30 min. After, diluted 1:40 samples are incubated for 30 min with the AmplexRed reaction mix, and their fluorescence was measured at Ex_{540}/Em_{590}.

2.3. SH-SY5Y neuroblastoma cell line

2.3.1. Cell maintenance

SH-SY5Y cells were cultured in Opti-MEM reduced serum media supplemented with 2 mM glutamine, 10% (v/v) foetal bovine serum (FBS) and antibiotic solution (100 U/mL penicillin and 0.1 mg/mL streptomycin) at 37°C in a humified 5% CO_2 atmosphere. Cells were split by aspirating the previous media and washing with Hank's Balanced Salt solution (HBSS), followed by trypsinization step with trypsin-EDTA (0.025% w/v) for 3 min at 37°C. Cells were later plated in 1:10-1:20 ratio range and accounted as one passage. Cells were observed to reach confluency in 4-8 days, depending on the dilution, after which the next passage was performed. Sub culturing is performed until the 20th passage, after which the cells are considered too distinct from the neuronal phenotype (*294*). Cells were plated in untreated petri dishes for subsequent passage and in 24 well and 96 well plates for functional and toxicity tests.

2.3.2. Nanomaterial and microreactors exposure

The main aim of nanomaterial study in SH-SY5Y neuroblastoma cell line was to determine possible cytotoxic effect, associated mainly with metal oxide nanoparticles and to compare their effect with liposomes and microreactors incorporating both referred above nanostructures.

Cells were incubated with either nanoparticles, liposomes or microreactors 24 hours prior to calculated reach of confluency (≈80-90% confluency). After the 24 hours exposure, cell viability was analysed. Both nanoparticles and liposomes were tested in same concentration range in order for cytotoxic effect to be comparable. The minimum concentration used was 10 ng/mL and the maximum 0.1 mg/mL. Concerning microreactors, both pre-defined numbers of microreactors and microreactor:cell ratios were tested. The tested amounts ranged from 1.5E4 to 3E5 of microreactors per well and ratio varied in a range between 1 microreactors per 20 cells up to 2 microreactors per each cell.

2.3.3. Microreactor *in situ* activity upon oxidative stress

Subjecting the cells to oxidative stress was achieved by treating them with H_2O_2. Cells were simultaneously incubated with microreactors and a range of H_2O_2 concentrations for 4 hours. Afterwards, their viability was evaluated by CCK8 cell counting kit. Control groups included cells exposed to microreactors with no H_2O_2 treatment and cells without the microreactors treated with the same range of H_2O_2 as the test groups.

2.4. Primary cell cultures

2.4.1. Culture

Cortical mixed cell cultures were obtained from E18 Sprague Dawley. The animals were purchased from Charles River. All the animal procedures reported were performed in accordance with the guidelines of Directive 2010/63/EU, and of the Portuguese Law (DL 113/213). The protocols were approved by the Instituto de Medicina Molecular João Lobo Antunes– iMM's institutional Animal Welfare Body – ORBEA-iMM and the Portuguese National Authority – DGAV (Direcção Geral de Alimentação e Veterinária).

The primary culture protocol followed a procedure described in (*295*). Embryos were extracted from the progenitor and washed in cold HBSS. The following steps were performed inside a laminar flow chamber. Embryos were decapitated and the brains were dissected. With a help of a dissecting microscope, meninges were carefully removed, and the hemispheres separated. Cerebral cortices were carefully isolated from the hippocampus, thalamus, and cerebellum areas, and mechanically dissociated with the surgical pincette. The tissue was later enzymatically digested

with 0.025% (w/v) trypsin-EDTA for 15 min at 37°C. The reaction was stopped by 3x consecutive washes with 30% FBS in HBSS with centrifugation (10 min, 200G) in between steps. Pellet was later resuspended in DMEM GlutaMax+F12 supplemented with 1% 100 IU/mL penicillin and 0.1 mg/mL streptomycin and 1% B27 supplement for mixed cultures media and filtered through 70 µm pore nylon filter. Cells were counted using Trypan-blue staining and hemocytometer and plated in PDL (0.1 mg/mL) and laminin (5 µg/mL) coated plates at a density of 1.5E5 cells/mL in 24-well plates for toxicity, reactive oxygen species assays and immunocytochemistry and 5E5 cells/mL cells in 6 well plates for western blot.

Cultures were maintained in a humidified incubator at 37°C with 5% CO_2. Culture media was changed on the third and seventh day after seeding and every 7 days thereafter. Cells were fixed or collected (western blot) at day 21 in culture.

2.4.2. Nanoparticle and microreactor exposure

In order to explore the toxicity effect of nanomaterials over primary cultures, and then compare it with its effect on the neuronal cell line, primary cultures were incubated with manganese oxide nanoparticles and microreactors. Concentration of nanoflowers used for the test was 500 ng/mL in phosphate buffer 0.2 M pH 7.4. Microreactors were studied in two distinct concentrations: 1.5E5 and 3E5 microreactors per well. As the cells are plated with 1.5E5 cells/mL, these values represent 1:1 and 2:1 microreactor to cell ratio, respectively. Cells were treated with nanomaterials 24h prior to fixation, therefore at DIV20.

2.4.3. Inflammation induction

The culture was treated with lipopolysaccharide (LPS) in order to induce an inflammatory-like response. Cells were activated by one acute insult with either 100 ng/mL or 1 µg/mL of LPS for 24 hours. After the 24h period, the levels of ROS were measured by DHE, as well as by the detection of inflammation related proteins through western blot and immunohistochemistry.

2.4.3.1. ROS measurement

For measuring reactive oxygen species, cells were incubated with 25 mM dihydroethidium (DHE) fluorescent dye for 30 min. DHE is superoxide specific fluorophore and has the particularity of having two excitation and emission

wavelengths, that allow the distinction between extracellular and intracellular O_2^-. Cell fluorescence was measured with TECAN Infinite M200, with excitation at 370 nm and emission at 420 nm for extracellular O_2^-, and excitation 535 nm, emission 610 nm for intracellular O_2^-. Fluorescence in each well was measured 4x4 (16 points from the well) in order to maximise the accuracy. The fluorescence of cells that had not been incubated with fluorophore was also measured in same conditions, and the obtained value was subtracted from the other measurements as background fluorescence.

2.4.3.1. Immunocytochemistry

For immunostaining, at DIV21 cells were fixed with 4% paraformaldehyde (PFA) for 30 min at 4°C. Afterwards, cells were washed 3x with PBS 1x for 5 min each wash. Excess unreacted aldehydes that result from the fixation processs, and that can cause an increase in background fluorescence were blocked by incubation with 0.1 M glycine for 10 min at RT. Cells were once again washed 3x with PBS and later incubated with 0.1% Triton in PBS for 10 min at RT to permeabilize the cellular membrane. Following, cells were blocked with 10% FBS in PBS for 1h at RT. Without intermediate washing step, samples were incubated with the primary antibody diluted in 10% FBS solution and left overnight. Next, cells were washed from the primary antibody with PBS 1x for 15 min and incubated with the secondary antibody (1:200 dilution in PBS) for 1h at RT. Once again, cells were washed for about 15 minutes with PBS and incubated with 1:1000 DAPI for 10 to 15 min. After DAPI incubation, cells were subjected to three to four more washes with PBS for about 15 minutes. Lastly, glass cover slips were fixed on glass slides with 7 µL Mowiol and allowed to dry stored in a dark place.

Microscopy pictures were acquired by inverted widefield Zeiss Axiovert 200 microscope (Carl Zeiss Inc., Germany) and confocal point-scanning microscope Zeiss LSM 710 (Carl Zeiss MicroImaging, Germany) with 40x objective and analysed by image processing program ImageJ.

2.4.3.2. Western Blot

At DIV21 cultured cells were collected for western blotting. For that, cells were washed with ice-cold PBS three times and lysed with RIPA buffer (50mM Tris-HCl (pH 7.5), 150 mM NaCl, 5mM EDTA, 0.1% SDS, 1% Triton X-100 and protease inhibitors (10mM NaF, 5mM Na_3VO_4 and complete Mini, EDTA-free protease inhibitor cocktail) for 15 minutes on ice. Cell lysates were collected and sonicated with three pulses, in order to further destroy the cell membrane and intracellular organelles. Protein concentration was quantified using the Bio-Rad DC reagent kit, accordingly to the manufacturer

protocol. The absorbance was read using a microplate reader TECAN Infinite M200 (TECAN, Switzerland). Quantified samples were then further denatured and stained by the sample buffer (70 mM Tris pH 6.8, 2% SDS, 6% glycerol, 120 mM dithiothreitol, 0.012% bromophenol blue) in a final concentration of 1x and incubating them for 10 min at 95°C. The amount of total protein loaded into the gel between 20 and 40 µg. Samples and a NZYColour Protein Marker II were loaded and ran in 12.5% sodium dodecyl sulphate polyacrylamide gel (SDS-PAGE) using a standard migration buffer (25 mM Tris-base pH 8.3, 192 mM glycine, 10% SDS) at a voltage of 80-120 mV in a Bio-Rad system. Separated proteins were then transferred onto polyvinylidene difluoride (PVDF) membranes (GE Healthcare, Buckinghamshire, UK), which had been previously activated in methanol, using a transfer buffer (25 mM Tris-base pH 8.3, 192 mM glycine, 15% methanol) at 350 mA for 1 hour 15 minutes on ice. The staining was then removed with sequential washes with TBS-T buffer (Tris-Buffered Saline Tween 20: 20 mM Tris-base, 137 mM NaCl and 0.1% Tween 20). Membranes were blocked in a 3% Bovine Albumin Serum (BCA) in TBS-T solution for 1 hour at room temperature (RT). After blocking, membranes are washed 3x with TBS-T and incubated with the primary antibody diluted in 3% BCA overnight, at 4°C and at constant rotation. Later, membranes were once again washed 3x times with TBS-T and incubated with correspondent horseradish peroxidase-conjugated secondary antibody in 3% BCA for 1 hour at RT and with constant agitation. Finally, the membranes were washed for 30 minutes with TBS-T and their immunoreactivity assessed by using blotting detection reagent ECL chemiluminescence system (Amersham-ECL Western Blotting Detection Reagents – GE Healthcare, Buckinghamshire, UK) and revealing the membrane with Amersham 680 system. Membranes that needed re-incubation with other antibodies were incubated with stripping solution (200 mM glycine, 0.1% SDS, 1% Tween® 20, 50% acetic acid glacial, pH 2.2) for 30 min at RT, followed with 3x washes with TBS-T. Afterwards, they were once again blocked in 3% BCA solution and submitted to the same protocol of immunostaining.

Results were analysed by densitometry, using the ImageJ software. Band intensities were quantified and normalized to tubulin that served as a quantification control.

2.5. Cell viability

Cell viability of the primary culture and SH-SY5Y neuroblastoma cell line was evaluated by three methods: CCK 8 cell viability kit, propidium iodade (PI) and trypan blue.

CCK8 commercial kit is an enzymatic colorimetric assay that allows to determine cell viability based on the enzymatic formazan dye conversion. Water soluble tetrazolium salt WST-8 is reduced by dehydrogenases present in the cells, producing a formazan dye with a distinct orange colour that can be measured by spectrophotometer at 450 nm. Cell culture is incubated with 10% (v/v) of CCK8 reagent and left in the incubator for 2 hours. Later, the media is taken to 96 well plate and absorbance is read at 450 nm by the plate reader. The results were analysed comparing each measurement to the negative control absorbance accounted as 100% cell viability.

Propidium iodide is a DNA intercalating fluorescent dye. It allows the estimation of cell membrane integrity. In cases when the dye is uptaken by the cell, it is representative of a loss of membrane exclusion capacity and compromised defence barrier, hence the cell is considered non-viable (*296*). In order to determine cell culture viability, cells are incubated with PI half an hour prior to the fixation. Later, cells are also stained by nuclear dye DAPI. PI marked cells are counted in percentage of the total number of cells.

Trypan Blue is a frequently used dye for cell count. In viable cells it only interacts with the exterior of the cell membrane giving it a light coloration at the membrane perimeter. In damaged or dead cells, the membrane integrity is compromised, and the dye can penetrate and stain the interior of the cell. In practice, after the 24h microreactors exposure, media is aspirated and cells are trypsinized with trypsin-EDTA 0.05% for 3-4 minutes, and then gently resuspended in new media. A sample of cell suspension was mixed with trypan blue in a 1:5 proportion and counted using a hemocytometer. For every condition, each independent experiment is performed in duplicates and each duplicate is counted in triplicates.

2.6. Statistical analysis

When producing nanoparticles, three independent batches were produced. For physical characterization data, each batch was considered as independent experiment, therefore all physical characterization of nanoparticles has a maximum N value of 3. When evaluating nanoflower enzymatic activity, each assay was accounted as one independent experiment. All conditions in enzymatic assays were performed in duplicates.

Liposomes and microreactors were produced consistently and each batch was accounted as one independent experiment, for both physical and biochemical characterization. Inside each independent batch, physical characterization was performed in triplicates and enzymatic assays in duplicates for each condition.

In studies involving SH-SY5Y, each subclone was accounted as one N per passage. All viability assays were performed in duplicates. For primary cultures, each embryo or a defined and separated from the culture group of embryos used for a primary cell culture was considered as an independent experiment (N=1). Inside each experiment, all tests were ran in duplicates. Western blot and microscopy results were analysed by ImageJ software (*297*).

Mathematical and statistical data was presented and analysed using GraphPad Prism (GraphPad Software, Inc., CA, USA). Data presented exclusively for demonstrational purposes was not statistically analysed, and it corresponds to one or two individual independent experiments. All data submitted to statistical analysis corresponds to, at least, three independent experiments with a minimum of two replicates in each. All data was presented as the mean value of the data set ± standard error of mean (mean ± SEM). Outlier analysis was performed with Rout method, allowing the identification of various outliers in one data-set, with the Q value 1%. Two tail unpaired T-student test was used when comparing only two sets of data (sample and a control). One-way ANOVA statistical analysis was used when comparing three or more experimental groups. Multiple comparisons tests were used when analysing the results with one-way ANOVA - the Dunnett multiple comparison test was used when the datasets were being compared to one control group and Sidak multiple comparison test was used for specific comparisons between groups. A p-value <0.05 represents statistically significant differences between the compared groups.

3. Results

3.1. Manganese oxide nanoparticles

Mn_3O_4 nanoflowers were synthesized by manganese deposition on oleic acid micelles, in a potassium permanganate solution. In the process of oil deposition, drying and calcination at high temperatures, particles form hausmannite structures: metal oxide nanoparticles containing both 2+ and 3+ Mn and a unique flower-like morphology. These were also previously demonstrated to have the capacity to mimic the three main antioxidant enzymes functions: to scavenge reactive oxygen species.

3.1.1. Transmission and scanning electron microscopy (TEM and SEM)

Synthetized Mn_3O_4 nanoflowers were analysed by TEM and SEM. As depicted in **figure 6A** and **6B**, these nanoparticles display flower- or snowflake-like structures composed of layered 2D nanocrystals. When comparing the obtained shapes with those reported in literature using the same synthesis protocol, the previously reported nanoflowers had much softer flower-like geometry (*254*, *292*). Nanoflowers synthesized in this work have extremely sharp blade-like edges. The synthesis was performed three times and the images are representative of the nanoflowers resultant from the synthesis.

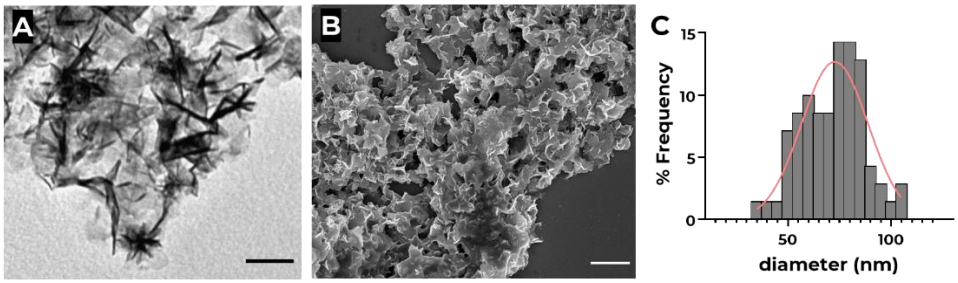

Figure 6: Mn_3O_4 nanoflowers. A) Transmission electron microscopy (TEM) of Mn_3O_4 nanoflowers- Scale bar 200 nm. B) Scanning electron microscopy (SEM) of Mn_3O_4 nanoflowers. Scale bar 500 nm. C) Size distribution of synthesized Mn_3O_4 nanoflowers. Measures represented in a frequency distribution histogram with a nonlinear fit. **N=3.** SEM was images were acquired by Miguel A. Ramos-Docampo, a post-doctoral researcher at Cell Mimicry laboratory in Interdisciplinary Nanoscience Center, Aarhus.

The size analysis was performed manually by setting the scale in Fiji software and measuring each nanoflower diameter separately. For higher accuracy of measurement, TEM images were used, measuring separated from the cluster nanoflowers. The particle size distribution is represented in **figure 6C**. The average nanoflower diameter was 71.68±1.801 nm (mean ± SEM). Nonlinear fit of frequency

distribution has a 72 nm amplitude, also representative of the normal distribution of the sizes. The aggregated state of nanoparticles in the electron microscopy samples can be explained not only by their instability and tendency to aggregate, but also by the sample preparation process. The copper grid used for sample deposition and visualization by electron microscopy requires a dry sample. By drying out the solvent on the surface of the grid, nanoparticles tend to create strong capillary forces, forming the observed in the **figure 6A** and **6B** aggregates (*298*).

3.1.2. Dynamic light scattering and ζ- potential

Physical characteristics of nanoparticles in the solution were evaluated by measuring the dynamic light scattering, a commonly used method for determining particle size, and by measuring the zeta potential, representative of the colloidal stability of particles and, by proxy, of the particle surface charge.

Nanoparticles were studied in three different buffer environments: phosphate buffer, phosphate buffer saline 1x ionic strength (PBS 1x) and phosphate buffer saline 10x (PBS 10x). Unless specific conditions for nanoparticles are required, metal and metal oxide nanoparticles are usually kept either in water or simple phosphate buffers. However, the choice of adequate solution for nanoparticle is important and can significantly impact their activity, stability, and lifetime. Another factor taken inconsideration is the application of the nanoparticles, as if they are to be applied to living systems, physiologically compatible buffers are a plus. Some of the factors that are important to take into account when considering an adequate buffer are its composition, pH, and ionic strength (*299*).

Phosphate buffer was chosen based on a previously published report, which demonstrated that it was the most adequate for the Mn_3O_4 nanoflowers, by keeping a good stability and maximizing the nanoparticles' activity (*248*). To determine the influence of buffer ionic strength, three phosphate buffers were tested. As nanoparticles would, in future studies, be used in physiological conditions, all buffers had neutral pH 7.4. Tested compositions were phosphate buffer 0.2 M, phosphate buffer saline (PBS) 1x and PBS 10x. As both phosphate buffer and PBS 1x are widely used as buffers for physiological pH, the expected outcome would be to obtain similar nanoflower stability in either buffer. In case of any significant variance, the presence of the salt in PBS would most probably be the decisive factor. For the same reason, nanoparticles in a PBS 10x buffer were expected to have a lower colloidal stability and possibly higher rate of precipitation in the solution.

ζ- potential is a measure of electrostatic forces between the charges on the surface of particles in solution. The stability standard is variable to each material, but a good stability is usually attributed to particles with values lower than -25 mV or higher than 25 mV (*174*) (by other data lower than -30 mV or higher than 30 mV (*300*, *301*)). The ζ- potential of nanoflowers in the phosphate buffer was measured to be -20.18±2.382 mV (mean ± SEM) (**table 1**), which corresponds to reasonably stable nanoparticles with some associated aggregation and/or precipitation. While nanoflowers in PBS buffer have a similar stability with a ζ- potential value of -20.54±1.495 mV, when the ionic strength of the solution is highly raised (tenfold raise), a drastic change to -2.749 ± 0.08630 mV is observed. This goes along with the theoretical data and predicted outcome, as high ionic strengths, namely salts, are very frequently used to decrease material colloidal stability and in order to precipitate it, since they are usually associated with the reduction of particle charge in solution (*302*).

Table 1: DLS size distribution and ζ-potential of Mn_3O_4 nanoflowers. Nanoflower characteristics tested in three buffers: phosphate buffer 0.2 M, PBS 1x and PBS 10x. Data presented as mean ± SEM.

		PB (mean ±SEM) **PDI**	PBS 1x (mean ±SEM) **PDI**	PBS 10x (mean ±SEM) **PDI**
N=1	DLS (nm)	2031±55.51 **0.3575**	1921±159.4 **0.3102**	1843±58.81 **0.2204**
N=2	Z-potential (mV)	-20.18±2.382	-20.54±1.495	-2.749±0.08630

Dynamic light scattering, which relies on the incidence and scattering of a monochromatic beam from particles in a solution was employed to determine the average size of particles in the solution (*303*). While the average particle size in solution is measured by Z-average size and gives a stable dimensional result of particle size, the polydispersity index (PDI) is a dimensionless fit to the correlation data obtained by all cumulative Z-average values and shows the homogeneity of the sample (*303*). In highly pure and homogeneous samples, PDI can go as low as 0.05, but it is extremely rare. In nanomaterial DLS analysis, a sample is considered to be monodisperse if the PDI is equal to or lower than 0.1 (*304*).

Regardless of buffer, average particle size determined by DLS was substantially higher than those determined by TEM, with nanoparticles in phosphate buffer showing an average size of 2031 ± 55.51 nm (mean ± SEM), 1921 ± 159.4 nm, and 1843± 58.81 nm for

PB, PBS 1x and PBS 10x buffers, respectively. (**table 1**). Not only, but PDI values in all three buffers showed a high level of heterogeneity in size distribution. While this shows a highly different result compared to that obtained by TEM, nanoflowers can show a tendency to aggregate, as can be assumed from the previously obtained ζ-potential value. As so, the measurements given by the DLS correspond to aggregates formed in the solution, and not to individual nanoparticles. The different buffers have no significant effect in aggregate size, concluding that once it reaches its aggregation limit, then these aggregates have an optimal stability. DLS measurement was only performed in one experiment (N=1) and, considering the nanoparticle tendency to aggregate and inability of the method to differentiate individual particles in an agglomerate, it was deemed as not adequate for posterior studies.

Taking into account the obtained results, phosphate buffer was considered to be the most adequate for the future experiments. The particle charge and size in solution are not only essential for determining their stability but also for further planning of microreactor assembly. A good colloidal stability of nanoparticles means a successful synthesis and a solution that can be used further in the study. The negative charge also defines the experimental design for the microreactor assembly, as it will require the use of positively charged polymers before and after nanoparticle deposition, in order to promote layer interaction.

Drawing from the results discussion, both phosphate buffer and PBS 1x would be optimal buffers. Phosphate buffer was chosen for storage and posterior use of nanoflowers, as it has a simpler composition, avoiding the possible risk of unforeseen interactions between buffer components and nanoflowers. It was also found to be more reliable, as a study has previously found a phosphate buffer optimal for nanoflowers enzymatic activity (*248*). From this moment on, to the rest of the work, unless stated otherwise, the working buffer is phosphate buffer 0.2 M pH 7.4.

3.1.3. Enzymatic activity

In order to test the capacity of nanoparticles to successfully mimic SOD activity, free solution assays were performed using a commercial kit for determining superoxide dismutase activity. This assay, described in **2.2.7**., relies on the production of O_2^- by oxidation of xanthine by xanthine oxidase and the oxidation of WST formazan by O_2^- into a colorimetric dye. Higher amounts of ion in the solution translates into a higher production of colour compound, measured by absorbance of the solution at 450 nm wavelength. The positive control is accounted as 100% of the superoxide produced by the assay and corresponds to the sample with no addition of any kind of antioxidant. Samples are normalized to the positive control and their values are representative of the concentration of ions remaining in the solution. The enzymatic assays were performed at 37°C to mimic more closely a physiological condition. In order to determine the optimal concentration of nanoflowers required to have a significant enzymatic activity, a concentration screening assay was performed. As presented in the **figure 7A**, the tested range of concentration started at 500 ng/mL and went up to 1.25 mg/mL, and the activity was then determined by the amount of O_2^- that nanoflowers have the capacity to scavenge in the 20 minutes of the assay.

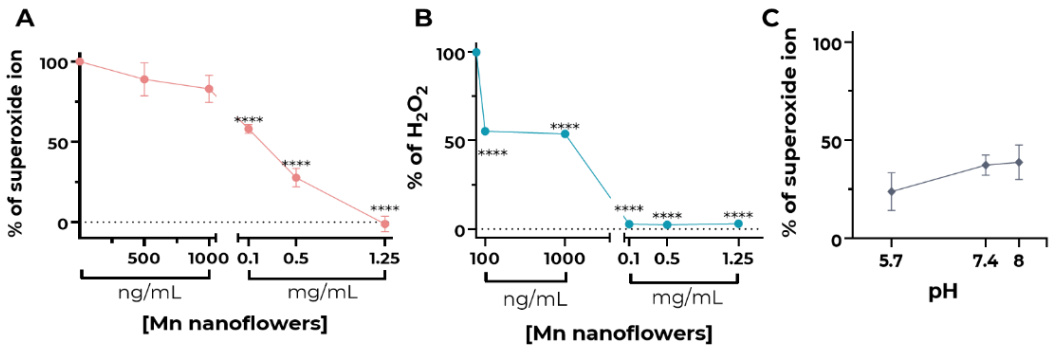

Figure 7: Enzymatic activity of Mn_3O_4 nanoflowers. A) Concentration dependent superoxide dismutase like activity of manganese oxide nanoparticles in free solution. All percentages normalized to control situation with zero nanoparticles or any other superoxide dismutase-like activity that is considered to be 100% of the O_2^-. Each percentage corresponds to the amount of O_2^- remaining in the solution after 20 min of reaction, when in presence of indicated concentration of pure nanoflowers. **N=3-10**. Values are presented as mean ± SEM. Statistical analysis to positive control, ** p<0.01, **** p<0.0001, one-way ANOVA with Dunnett multiple comparison test. **B)** Catalase like activity of Mn_3O_4 nanoflowers in free solution. All data normalized to positive control (Presence of H_2O_2 and absence of any material with catalase activity). Each percentage corresponds to the amount of H_2O_2 remaining in the solution after 30 min of reaction, when in presence of indicated concentration of pure nanoflowers. **N=3-4**. Values are presented as mean ± SEM. **C)** pH dependent superoxide dismutase like activity of manganese oxide nanoflower in free solution. Data normalized to 100% control situation with no antioxidants in the reaction (not presented in the figure). All data presented and mean±SEM, **N=4-10**, no significant differences found.

As seen above, at concentrations in the order of nanograms, nanoparticles have no significant effect in O_2^- consumption. A significant decrease in the amount of O_2^- in solution can only be observed at 0.1 mg/mL, with 58.06±2.801% (mean ± SEM) of O_2^- remaining in the solution after the reaction. When the concentration is increased to 0.5 mg/mL, the amount of remaining O_2^- is equal to 34.06±4.136%, and if the concentration is raised up to 1.25 mg/mL, -1.212±4.824% of the initial O_2^- amount is detected. The lower than zero number in ion scavenging is most likely related to the assay's associated error. As so, 1.25 mg/mL of manganese oxide nanoparticles are concluded to consume all the O_2^- produced by the assay, while 0.5 mg/mL consumes approximately 66% of the ion. The assay was performed in ten (for 0.5 mg/mL concentration) and three (remaining concentrations) independent assays (N=3-10).

In order to evaluate catalase activity of free nanoparticles, a similar range of concentrations was incubated with 400 μM of H_2O_2 and left to react for 30 minutes at 37°C (**figure 7B**). Unlike superoxide dismutase like activity, catalase like activity of free nanoparticles was observed in lower range of concentrations. Starting from the lowest concentration, an incubation with 100 ng/mL of pure nanoflowers resulted in almost 45% of H_2O_2 decrease (55.34±0.8708% of H_2O_2 remained in the solution). A 10 fold raise of concentration (1000 ng/mL) did not notably change the activity, when compared with 100 ng/mL, with 53.83±0.6543% of H_2O_2 remaining in the solution after the reaction. However, when testing concentrations 0.1, 0.5 and 1.25 mg/mL, remaining H_2O_2 in the solution was 2.715±1.942%, 2.405±0.4427% and 3.064±0.6997% of the initial concentration, translated at roughly 98% for 0.1 and 0.5 mg/mL and 97% for 1.25 mg/mL of the ion scavenged. As low concentrations of nanoflowers showed considerable amounts of H_2O_2 consumption, a future study to be conducted would be to explore the lowest threshold for nanoparticle concentrations, in order to have significant catalase-like activity. The obtained result comes closer to the concentrations explored in the study that was taken as the basis for nanoflower synthesis (*246*), however, further studies are required. Nanoparticles synthesized in this study may have a higher tendency for catalase like activity. As described, hausmannite nanoparticles are a mix of both 2+ and 3+ oxidation state manganese, and the ratio between the two can determine whether they are more active as SOD or catalase enzyme (*247*).

Both enzymatic assays showed poor linearity in concentration dependent activity. Kinetic studies of nanoparticle enzymatic activities are very sparse as nanoparticle enzymatic activity is still a very new concept and these rarely obey the same chemistry rules as those established for biological enzymes. However, some studies with

manganese oxide nanoparticles (flowers (*247*, *248*) and spheres (*305*)) showed linear behaviour in concentration dependent enzymatic activity and Michaelis-Menten -like kinetics, that allowed for the calculation of Km and Vmax of the reactions. Moreover, when nanoflowers were studied with variable concentrations, for evaluating SOD activity, they showed exponential activity growth until a saturation plateau is reached. These studies also register significant exponential activity at lower concentrations than the ones presented in this work. While previously reported manganese oxide nanoparticles had significant SOD and catalase activities in a range of 10-100 ng/mL, in the synthesized nanoflowers, as seen in the **figure 7**, only concentration above 0.1 mg/mL showed significant SOD activity. This is not an expected result, as these nanoflowers show a very high surface to volume ratio and sharp edges, associated with an accumulation of higher amount of free energy and usually related to higher enzymatic capacity. A similar study of spherical Mn_3O_4 particles also showed a very similar pattern of SOD-like enzymatic activity (*306*). In free solution, these consumed O_2^- in an exponential manner starting from 5 µg/mL, however, they reached a consumption plateau at approximately 60-70% of the ion scavenging activity, *au contraire* from the **figure 7** where a high concentration of nanoflowers consumes 100% the produced by the assay ion.

The optimal concentration for further studies was decided to be 0.5 mg/mL as it consumed a reasonable amount of O_2^- (≈66%) and almost entirely H_2O_2, but was not as concentrated as the 1.25 mg/mL solution that could potentially be more harmful for the studies *in situ*, as higher concentrations of nanoparticles may both consume a larger than necessary amount of O_2^- (a small amount is physiologically necessary) and be more cytotoxic to cells (*307*).

In some cases, nanoparticle activity can also be pH-dependent (for example iron oxides (*308*) and platinum nanoparticles (*309*)). In order to test whether Mn_3O_4 nanoflowers activity is also pH-dependent, nanoparticles were resuspended in three different pH buffers and had their activity tested by the superoxide dismutase activity assay kit (**figure 7C**). As phosphoric acid is a triprotic acid, it allows to have a stable phosphate buffer with three distinct pH: 5.7, 7.4 and 8. Maintaining the same conditions for the nanoparticles, such as same buffer ionic strength of 0.2 M and the same reaction temperature and only varying the pH, the activity was measured in four independent assays (N=4).

In the tested pH range, all conditions appeared to maintain similar enzymatic activity. As seen, varying the pH of the buffer does not appear to significantly influence

their enzymatic activity. No higher nor lower ranges of pH were further tested as they were deemed not essential for the work in question. As nanoflowers are to be applied to biological systems, extreme pH conditions would not be favourable and, therefore, they were not further investigated. For posterior use, in the presented work and/or biomedicine application, it was essential for nanoparticles to have a good stability and activity at normal ionic strength and physiological conditions, such as neutral pH and 37°C temperature. The consistency can also be seen as beneficial, as it allows to assume stable and predictable activity of nanoparticles even in case of unpredicted variability, such as pH change in the extracellular space or entrapment of nanoparticles in acidic vesicles as a result of cell uptake.

With all the to-the-point obtained data, the characterization of free solution enzymatic activity of nanoparticles was considered to be sufficient for the intended application. By synthesizing Mn_3O_4 nanoflowers, the aim was to find an optimal applicability conditions, and study nanoflowers catalytic activity in different situations such as variation in concentration and pH of the solution. Summing up the previous data, the nanoflower working solution was established as 0.5 mg/mL in phosphate buffer 0.2 M and with pH of 7.4. When choosing the working solution, the optimal enzymatic activity, registering a significant ion decrease without using unnecessarily high concentrations of nanoflowers, as well as nanoflowers physical properties in a solution, such as stability and size distribution in different buffer environments, were both taken into account.

3.2. Liposomes

Liposomes are used in biomedicine if order to protect and “hide” the cargo that could not be used directly in the organism. Lipid composition, as well as physical properties such as size, lamellarity and charge of the liposome, are all essential for a successful enzyme encapsulation and activity. Adequate lipid formulation have to take into account the cargo, the environment that the liposomes will be subjected to and their required activity. This chapter describes liposome synthesis and SOD enzyme encapsulation, characterizing the produced liposomes by their physical and enzymatic properties.

3.2.1. Dynamic light scattering (DLS) and ζ- potential

The liposomes were synthesized in two formulations presented in the **table 2**. The physical characteristics were analysed by DLS in order to determine the average size and size homogeneity of the liposomes. As previously referred in the chapter **3.1.2.**, DLS provides with the dimensional data of particle size, as well as dimensionless PDI value that shows the homogeneity of the measured sample. A sample is considered monodispersed if the PDI is equal or lower than 0.1. ζ- potential analysis allowed to determine the average liposome charge in the solution, which is important for the assembly of the microreactors, as the charge defines the neighbouring layer charges in order to guarantee correct assembly.

The first formulation tested in this work was based on a previously described protocol (*57*) with a main lipid DPPC, cholesterol (incorporated in order to confer better stability to the membrane), and stearylamine (SA) (discussed in more detail in chapter **1.2.4.**). In this previous study, between several variable compositions, the DPPC:Chol:SA in 6:3:1 wt ratio was described as the most favourable for superoxide dismutase encapsulation, forming homogeneous and unilamelar liposomes. This composition was, therefore, replicated for the liposome synthesis in this work. Additionally, a second formulation was also tested, which excluded the charged lipid (SA), using only DPPC and cholesterol to synthetize liposomes with the proportion compensation – 7 parts of the DPPC to 3 of cholesterol. The characterization values of both liposomes are presented in the **table 2**. Each formulation was characterized with empty liposomes and with liposomes containing encapsulated superoxide dismutase. It should be noted that liposomes with encapsulated enzyme undergo additional freeze and thaw cycles, the double of the extrusions through a 200 nm filter and a size exclusion chromatography. Lipids have a natural tendency to form liposomes in an aqueous solution, however, without any process control, the formation is spontaneous and rarely have good levels of dispersity, or the same number of membrane lamellae. Both freeze and thaw cycles and filter extrusion are standard methods to control the homogeneity of produced liposomes (*125*, *126*, *137*). Freeze and thaw cycles are fast temperature changing environments where the liposomes are quickly destroyed and re-assembled, promoting formation of only unilamelar vesicles. Filter extrusion above lipid melting temperature allows to uniformize liposome size while the size exclusion chromatography further separates any different size vesicles and non-encapsulated enzymes. Both empty and enzyme containing liposomes, in both formulations were expected to have a maximum vesicle size of 200 nm and a low size distribution with more uniform values for liposomes after the enzyme encapsulation.

Table 2: Physical characterization of two lipid formulations of liposomes. Liposome size distribution was determined by DLS, data presented as mean ± SEM of the measured liposome size and PDI – polydispersity index representative of the dispersity of the values. First formulation was synthesized and studied in three independent experiences (**N=3**) while the second in nine independent experiences (**N=9**). DLS was performed in both before (L_{empty}) and after (L_{SOD}) enzyme encapsulation and chromatography steps. ζ- potential data presented as mean ± SEM.

		L_{empty} (nm, mean ± SEM) **PDI**	L_{SOD} (nm, mean ± SEM) **PDI**
N=3	DPPC:Chol:SA (6:3:1)	2242±209.8 **0.2793**	1945±206.5 **0.4495**
N=9	DPPC:Chol (7:3)	167.8±0.9517 **0.2006**	141.0±1.502 **0.1142**
		ζ- potential $_{DPPC:Chol}$	**-7.612 ± 0.7268 mV**

The first formulation reported in the article showed high aggregation rates, with an average size of 2242±209.8 and 1945±206.5 nm (mean ± SEM) for empty liposomes and enzyme containing liposomes, respectively. The size distribution was also broad with PDI of 0.2793 and 0.4495 for empty liposomes and enzyme containing liposomes. As seen before, after enzyme encapsulation and chromatography, while liposomes were expected to be more homogeneous, these, on the contrary, show higher dispersity. Visually, there were also issues as the sample formed white deposits and a very large concentration of liposomes would be lost in the chromatography. As the dilution factor associated with size exclusion chromatography is about two or three, these would barely yield around a six times diluted sample. Due to the formation of more dense white deposit, it was concluded that most likely liposomes aggregated for unknown reasons. The synthesis was replicated 3 times, with high control of every step and the final result was not altered. Among the used lipids, stearylamine was the first one assumed to most possibly cause the observed phenomenon. DPPC and cholesterol are much more widely used in the production of liposomes while SA use is sparser, despite being a common method for encapsulation of negatively charged cargo. If stearylamine conferred some instability to the membrane, not integrating or cooperating well with the other lipids, liposomes could become “leaky” and unstable. This factor can promote liposome aggregation and fusion (*310*), causing aggregation and destruction of membrane integrity and cargo loss. Liposome ζ-potential can also be a factor in the observed colloidal instability of vesicles. The possibility of ζ-potential being the culprit for the liposome instability is

very low as liposomes containing SA, positively charged lipid, would only augment the electrostatic repulsion between vesicles, therefore conferring a higher colloidal stability. However, the possibility cannot be completely excluded.

New liposomes with only DPPC and cholesterol in a 7:3 ratio were fabricated and characterized. These, from the beginning, did not present the visible issues of the previous ones, with no formation of dense precipitate and a homogeneous solution instead. As seen in the **table 2**, empty liposomes have 167.8±0.9517 nm in diameter (mean±SEM). The polydispersity index is 0.2006. It does not represent a very good size distribution and suggests yet a poor monodispersity of produced vesicles. After the enzyme encapsulation and size exclusion chromatography, liposomes present already favourable characteristics. They have an average size of 141.0±1.502 nm in diameter. The polydispersity index also decreases to 0.1142, indicative of considerably monodisperse sample. As so, the second formulation was considered to be functional and submitted to further physical and applicability studies.

For the future microreactor assembly, the charge of individual components is important, as the layering is based on the electrostatic attraction in the solution. Therefore, ζ- potential of liposomes was measured to determine future procedure. Negative or positive charge of liposomes would be decisive on the polymer used immediately before, in order to guarantee a correct deposition. When measured, liposome surface charge in solution is -7.612±0.7268 mV (mean ±SEM) in a HEPES 10 mM pH 7.4 solution. Low ionic strength of the buffer is necessary for accurate measurement, as the solvent's high ionic content may interfere with the reading, but the remaining characteristics and buffer composition is close to the one used in future assays. In free solution, the obtained value is representative of a poor colloidal stability but, as the liposome's purpose is to be assembled as a part of a bigger particle, it was not considered to be an issue. As so, final version of liposomes, and the most used in this work, are the second formulation DPPC:Chol: monodisperse, with an average size of 141 nm and -7.612 mV surface charge, a negative charge in a solution, with superoxide dismutase enzyme encapsulated in the liposomes.

3.2.2. Enzymatic activity.

After physical characterization of liposomes, the encapsulated superoxide dismutase enzymatic activity was evaluated (**figure 8**). As in the case of nanoparticles, in order to determine liposome enzymatic activity, the SOD activity assay was used. The control situation corresponds to the sample treated with reagents that produce O_2^- and no antioxidants. As so, the control absorbance value is accounted as 100% of the O_2^- produced by the assay and the test values are the O_2^- produced in the solution with the analyte present. The samples absorbances are normalized to the control situation. The assay was performed at 37°C in a 20 min reaction. Enzyme-containing liposomes were synthesized and had their activity measured in nine independent syntheses (N=9).

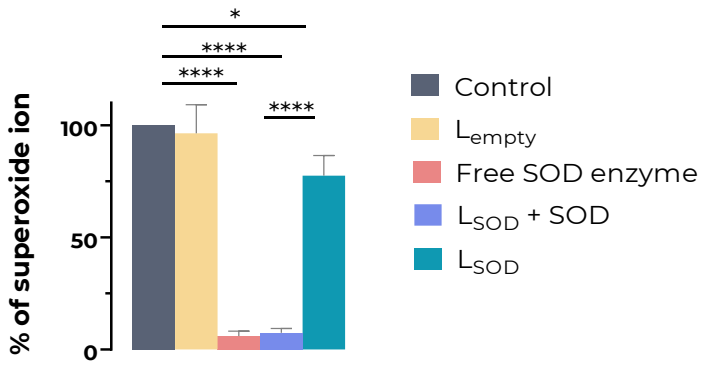

Figure 8: Superoxide dismutase activity of liposomes and enzymes in free solution. Control bar corresponds to reaction with no antioxidant compounds and normalized to 100% of O_2^- produced by the assay. Other data represent amount of O_2^- that remains in the solution after the reaction when incubated with each particular material. L_{SOD}+SOD refers to liposomes before the non-encapsulated enzyme is separated by the size exclusion chromatography. Liposomes after chromatography have only the liposomes and enzyme that was incorporated in it and designated as L_{SOD}. All data presented as mean ± SEM, **N=5-10**, * $p<0.05$, **** $p<0.0001$. Statistical test used to analyse the data was one-way ANOVA with Sidak multiple comparison test.

Various controls were made in order to calculate the encapsulation rate of superoxide dismutase enzyme in the liposomes with maximal precision. As lipids by themselves are susceptible to oxidative damage, reactive oxygen species react with membrane/vesicle lipids, oxidizing them in a process called lipid peroxidation (*311*, *312*). Although damaging to the lipid structure, it also reduces, to some extent, the amount of active reactive oxygen species in the solution. As this can be a changing factor when measuring the amount of O_2^- amount in the solution, the activity of empty liposomes was evaluated. After the reaction with presence of empty liposomes, 96.43±12.67% (mean ± SEM) of O_2^- remained in the solution. As the decrease is not significant, the

data suggest that the lipid contribution to ROS conversion in a solution is non-significant and therefore, not accounted. As a positive control, pure SOD1 enzyme was used in 500 U/mL, the same concentration as the one used in the synthesis. After the incubation with the enzyme, only 5.974±2.236% of O_2^- remained, meaning that more than 94% of ion was scavenged by the enzyme. Similar situation occurs when measuring activity of liposomes before the size exclusion chromatography (both encapsulated and non-encapsulated enzyme in the solution). After the incubation, 7.457±1.895% of ion remained, indicating a consumption rate of 93%. As the statistical test shows no significance between these values, the enzyme in the liposomes plus free enzyme solution has a full function, that is, the enzyme encapsulation process does not affect the enzyme activity. Finally, liposomes with the encapsulated enzyme were separated from the free enzyme and the enzymatic activity evaluated. In the assay, 77.47±9.002% of the O_2^- remained in the solution.

For the determination of the encapsulation efficiency, the O_2^- consumption by pure SOD enzyme (500 U/mL) was assumed as the maximum value of the ion scavenging. As so, 94.03% were considered as 100% of enzymatic activity, correspondent to the activity of 500 U/mL solution of pure enzyme. In function of this value, the encapsulated enzyme activity was calculated.

$$\frac{(100 - L_{SOD}) * 100}{100 - \text{Free SOD enzyme}} = Encapsulated\ enzyme\ activity$$

By the presented equation, the enzymatic activity of encapsulated SOD enzyme equals to 23.96% of the ion consumption rate. As the activity of empty liposomes was almost null and considered insignificant, the activity is attributed to the enzymatic capacity of the encapsulated enzyme. Moreover, considering 500 U/mL as the enzyme concentration responsible for 100% of the ion consumption, encapsulated enzyme has the activity of 119.8 U/mL. This encapsulation ratio goes along the predicted by the literature encapsulation rates of SOD enzyme by conventional methods of synthesis (*55*).

3.3. Microreactors

3.3.1. First generation of microreactors: Mn_3O_4 nanoflowers and liposome-encapsulated superoxide dismutase

Microreactors containing liposome-encapsulated SOD and nanoflowers were synthesized following the described protocol (**2.2.3.**) Briefly, microreactors were assembled from PS particles, with coating of PDA as initial and finishing layers. Microreactors contained a layer of nanoflowers and two layers of liposomes, stabilized with layers of PLL and PMAc as intermediates. The structure was characterized physically and enzymatically.

3.3.1.1. Physical characterization

After the assembly, a deposition control was made, to evaluate the efficiency of the assembly. The deposition of active components: nanoflowers and liposomes was verified by direct methods, TEM and fluorescence microscopy, respectively. As the remaining layers rely on the electrostatic forces to assemble, a surface charge measurement was also used.

To confirm the deposition of the liposomes in the microreactors, a fluorescent dye was used. Di-8-ANEPPS is a membrane potential responding dye. As it is lipophilic and can bind and be retained in the cellular membrane, this dye is widely used to stain lipid membranes and extracellular vesicles, showing low levels of unspecific fluorescence and high levels of fluorescence when bound to lipids (*313*). It has also been demonstrated to specifically interact with DPPC and DPPC+cholesterol membranes (*314*) Incomplete microreactors after each liposome deposition step and fully assembled microreactors were incubated with the dye for 20 min and the fluorescence of each sample observed (**figure 9A**). The first layer gives some fluorescence, yet very low, representative of one layer of dyed liposomes (**figure 9A1**), while the second already represents a microreactor with two layers of liposomes, both fluorescently tagged. The intensity of fluorescence is also approximately double of the first (**figure 9A2**). Finally, fully assembled microreactor shows roughly the same pattern and intensity of fluorescence as the samples marked immediately after the second layer of liposomes (**figure 9A3**). The increase in fluorescence from the one liposome layer to two layers demonstrates that microreactors do, in fact, incorporate both layers of liposomes, as intended by the assembly. Final fully assembled microreactors (**figure 9A3**) show a very close to the two-layered microreactor

fluorescence, interpreted as retaining all the layered liposomes correctly until the end of the assembly, and for posterior use.

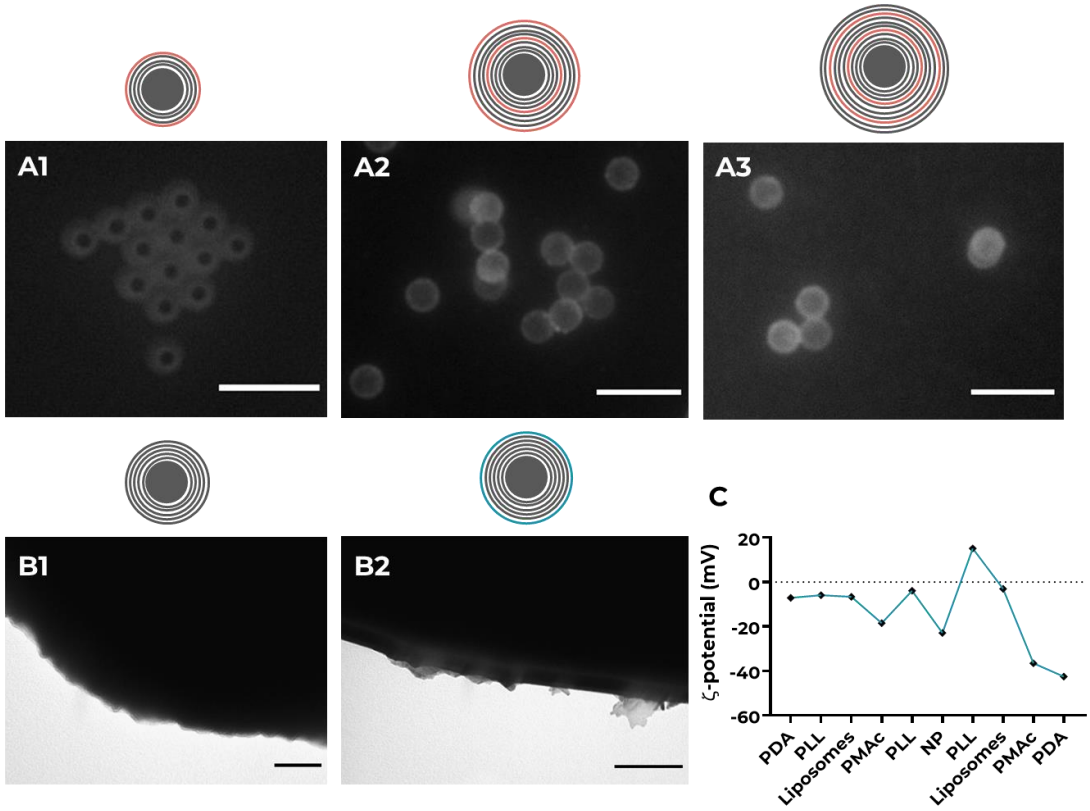

Figure 9: Deposition control in first generation microreactors. A) Liposomes labelled with Di-8-ANEPPS fluorescent dye. A**1)** Partly assembled microreactors, with only one layer of liposomes. **A2)** Partly assembled microreactors, after the deposition of the second layer of liposomes. **A3)** Fully assembled microreactors. All scale bars are 20 µm. **B)** Nanoflower deposition on a microreactor surface. Transmission electron microscopy acquired representation of Mn_3O_4 nanoflowers adsorption on the microreactors. **B1)** Microreactor surface before the nanoflower deposition, scale bar 200 nm. **B2)** microreactor surface after the nanoflower deposition, scale bar 200 nm. **C)** Microreactor layering control with surface ζ-potential measurement. Each point corresponds to the value of microreactors surface charge after layering the correspondent polymer or nanomaterial. All data presented as mean, N=1.

The nanoparticle deposition was observed by transmission electron microscopy. During the assembly, samples of microreactors before and after the nanoparticle attachment step were isolated, deposited on the copper grid and the surface visualized under the electron microscope (**figure 9B1**). While irregular from the previous deposition steps (polymers and liposomes), the microreactor surface shows none of the nanoflower typical shape deposition. The after sample was isolated immediately after the nanoflower deposition of the microreactor surface (**figure 9B2**). As seen, it contains clear particle deposition with the irregular “flower” shape of the

Mn_3O_4 nanoparticles. Parting from the given scale, deposited particles have around the 70 nm in diameter, typical to the synthesized nanoflowers, showing this way a successful deposition of the layer of nanoflowers on the surface of microreactor.

Confirming the remaining polymer layers assembly is not done in such direct way. Layer-by-layer technique has as its principle the electrostatic attraction between different charges. The assembly assay alternates the polymers, layering positive and negative charged molecules in order to promote the interaction and layer attachment. As ζ-potential allows to estimate the surface charge of a particle by measuring its electrostatic interaction with adjacents, it was used to monitor the charges in the charge with each assembly step (**figure 9C**).

As the assembly is based on the attraction of opposite charges, the expected outcome would be a positive-negative variation between layers. It is important to note that only one polymer in the assembly does not rely on the electrostatic forces in order to interact with the previous layer– PMAc. As it has cholesterol in its composition, it integrates in the liposomes' membrane. But as the polymer also has an associated negative charge, following step deposits positively charged PLL as the counteract of PMAc associated charge, depending on the electrostatic forces for the further assembly.

As PDA is a negative charged polymer, the first layer of the assembly also shows negative zeta potential value of -7.073 mV. Next the microreactor is coated with PLL, positive charged polymer. However, the microreactor charge stays almost unaltered – surface charge of -5.890 mV. Liposome coating does not alter the charge considerably, bringing it close to the PDA coated reactor with -6.633 mV. However, this charge is very close to the real zeta potential of liposomes, measured in the chapter **3.2.1**. which is -7.6 mV. Coating with PMAc reduces the charge of microreactors to -18.53 mV and following layer of PLL raises this charge up to -3.910 mV, fairly close to 0 but not yet a positive charge as expected. Later, coating with manganese oxide nanoparticles causes a decrease in the surface charge, bringing it to -22.93 mV which is also close to the ζ-potential of free manganese oxide nanoparticles measured in **3.1.2**. Once again, a layer of positive charged PLL is used to attach to nanoparticles, and the microreactor surface charge is raised to 15.13 mV. Microreactors are once again coated with liposomes and exhibit a -3.007 mV surface charge that later decreases to -36.60 mV due to PMAc and finishes with -42.60 mV due to PDA final polymer coating.

The obtained ζ-potential pattern does not completely correspond to the one that was expected. As seen before, the first layering steps show very little variations in

charge, and the PLL coating does not raise it to positive values. The more progressed was the process, the more the expected zig-zag pattern was notable. Only after the first PMAc incubation, when the reactor charge decreased significantly, the changes in between layers became more apparent. From that on, each step showed a higher variation then the one before. This can be very easily seen when looking only at PLL charges. While in theory it should always give a positive charge, first PLL layer was negative and almost equal to neighbouring components. The second layer, while still negative, came much closer to zero and finally third reached a high positive value. It was hypothesized that even though at first assembly still occurs correctly as it continues and all components are layered correctly, there is not enough surface charge to, in its turn, attract much opposite charge and register a big difference. As the polymers are accumulating, and with use of more strongly charged one, surface charges accumulate enough for the next layer to also attach in much more significant way, causing a bigger shift in the ζ-potential.

For the final step of microreactor assembly, PDA was the polymer of choice. Since these microreactors are to be used in biological systems, mainly in the brain, a previously conducted study with similar microreactors analysed different coatings interaction with cells in culture. As it concluded, PDA was the one that showed the best interaction with both cell line neurons and primary neural cultures (*279*) (*277*). PDA is as a polymerizing compound, with a high compatibility and adherence to various materials (*315*). It is a very common polymer used in order to enhance the biocompatibility of materials and it is especially widely applied in the central nervous system (*316*), as it is associated with a reduction of neuroinflammatory responses to materials foreign to the system (*317*), in addition to good interaction with neurons, with capacity of modulatory and scaffold action for neuronal stem cells (*318*, *319*), while having no dopaminergic activity.

Overall, based on these results, the different stages of microreactor assembly were successful. The microreactor's main purpose is to incorporate and stabilize its active components, compartmentalizing them and improving the biocompatibility of the less compatible ones. Due to core´s size, it also allows for the microreactors to maintain a cell-like profile, by remaining in the extracellular space and not being internalized by their biological counterparts. While biocompatibility was not yet evaluated as this stage of the study, results suggest that both nanoparticles and liposomes were successfully incorporated into the structure, and that microreactors stabilized and assembled with all the planned layers.

3.3.1.2. Enzymatic activity

As microreactors incorporate both nanoflowers that consume approximately 66% of the O_2^- (when in the same concentration as the ones used for microreactor production), and liposome encapsulated superoxide dismutase, which consumes approximately 23% of the ion, the enzymatic activity of microreactors is expected to be either a sum of the activity of both these components or, at least, to be higher than the activity of each individual component.

Identically to previous results, O_2^- scavenging activity of the microreactors in free solution is measured by the SOD activity commercial kit. Reagents responsible for generation of O_2^- and conversion of WST into a colorimetric dye are incubated with and without the presence of microreactors for 20 min at 37°C and were later analysed by measuring the absorbance of the solution (**figure 10**).

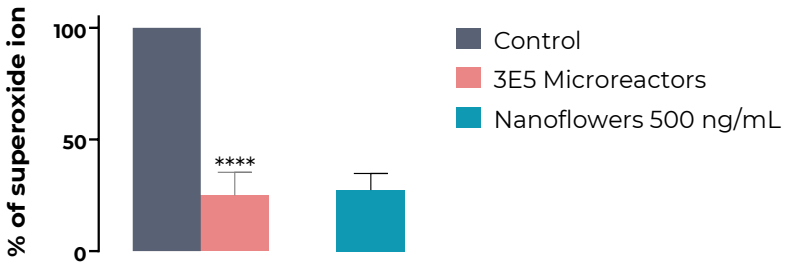

Figure 10: SOD-like activity of free Mn_3O_4 nanoflowers and microreactors containing liposome encapsulated SOD and Mn_3O_4 nanoflowers in free solution. Control bar is correspondent to 20 min reaction without the presence of any antioxidant and is normalized to 100% of O_2^-. Pink bar corresponds to percentage of remaining O_2^- in the solution after 20 minutes of reaction in the presence of microreactors. All data presented as mean ± SEM, **N=7**, **** p<0.0001, two tailed unpaired T-student test, compared to control. Blue bar corresponds to the activity of free Mn_3O_4 nanoflowers, evaluated in 3.1.3. and presented as a mean of activity comparison.

The control bar corresponds to the maximum quantity of the O_2^- produced by each assay. It is accounted as 100% of ion and other conditions are normalized to the control value. Incubation with microreactors yields 25.02±10.25% (mean±SEM) of the original concentration of ion. This corresponds to a 75% decrease of the total quantity of the ion, scavenged by microreactors.

Microreactor activity was not as high as expected. Considering that nanoflowers alone yield 66% of O_2^- consumption, 75% of ion scavenged by microreactors suggest that the activity is either not additive or one/both components are not functioning to their full capacity. Since the presence of both nanoparticle and

liposome after the assembly was previously confirmed, but no cumulative activity was observed, two theories can be proposed to explain this phenomenon. First, while the TEM and fluorescent staining deposition controls allow to confirm the presence of nanoflowers and liposomes on the microreactor surface, they do not allow to estimate the amount of nanoflowers or liposomes that were incorporated into the structure, restricting this way a numerical evaluation of the deposition success rate. Second, assuming that both nanoflowers and liposomes are fully deposited on the microreactors, the assembly process or the following coating layers may interfere with the materials, partially or fully compromising their activity. This assay, *per se,* was not enough to draw a conclusive result as to why the activity was lower than expected, so further tests were performed.

3.3.2. Second generation: Mn_3O_4 nanoflowers-containing microreactors

As previously discussed, free solution SOD-like activity of microreactors incorporating both liposomes and nanoflowers was similar to free nanoflowers free solution activity. In order to further elucidate the mechanism of catalytic activity in microreactors, a new variation of these microreactors was produced: containing only nanoflowers and no liposomes. The assembly occurred with the deposition of initial PDA layer of PS particles, followed by PLL and nanoflowers deposition, with once again PLL layer on top of nanoflowers. The assembly was concluded by PDA finishing layer. The characterization followed a similar pattern, with some modifications in experimental design. The microreactors with only the nanoflower active principle are expected to have close characteristics both in the shared assembly steps and in free solution enzymatic activity, with the previous nanoflower and liposome containing microreactors.

3.3.2.1. Physical characterization

As these new microreactors only include one active principle: Mn_3O_4 nanoflowers, the main deposition control only included the observation of particle deposition on the reactor surface and overall ζ-potential of the layering. The images of nanoparticle deposition on the microreactor were acquired with scanning electron microscopy (SEM) of uncoated polystyrene spheres, as well as after the deposition of intermediate coatings and nanoflowers (**figure 11**).

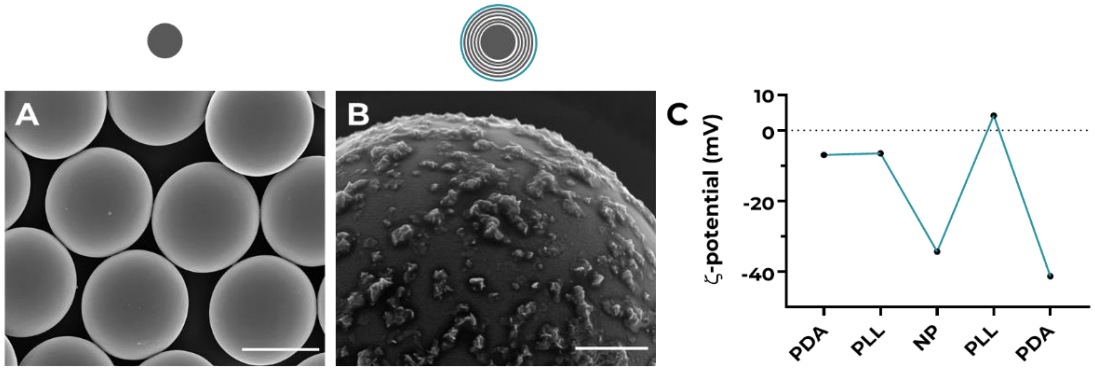

Figure 11: Deposition control in second generation microreactors. A) Uncoated polystyrene spheres used for the posterior layer-by-layer assembly. Images acquired with scanning electron microscopy Scale bar 5 µm. **B)** Microreactor after the nanoflower deposition on the polystyrene reactor core. Images acquired with scanning electron microscopy Scale bar 1 µm. **C)** Microreactor layering control with surface ζ-potential measurement. The charge value of each point corresponds to the value of microreactors surface charge after layering the correspondent polymer or nanomaterial. **N=1**, data presented as mean value. SEM was images were acquired by Miguel A. Ramos.Docampo, a post-doctoral researcher at Cell mimicry laboratory in Interdisciplinary Nanoscience Center, Aarhus.

In the first image (**figure 11A**) pure polystyrene spheres are seen. These are commercially purchased and deposited directly onto the copper grid, without any further coating or/and treatments and visualized under an electron microscope. The surface is uniform and no deposition or any kind of interaction can be observed. Later, the microreactors are also visualized after the deposition of PDA and PLL intermediate coatings and nanoflowers deposition on the surface of the sphere (**figure 11B**). The result shows clear deposition of Mn_3O_4 nanoflowers on the surface of the microreactors in a relatively high success rate. These also show the morphology of nanoflowers.

The deposition control was also followed in the same manner as before, as with the first generation microreactors. Relying of the fact that all polymers have their own charges and are layered in order to interact electrostatically, after each layer deposition the charge is expected to vary between positive and negative charge and create a zig-zag pattern when the charge of microreactors after each layer was measured by ζ-potential. The charges correspondent to the surface charge after each deposited layer are presented in the **figure 11C**.

Similar to what was previously described (**figure 9**), first layer of PDA left the microreactors with a surface charge of -6.917 mV. The next layer of the positively charged PLL did not significantly change the charge, as it remained as -6.493 mV. However, after the nanoparticle deposition, its charge decreased to -34.27 mV and,

posterior incubation with PLL raised the surface charge to positive numbers: 4.223 mV. Finally, the finishing layer of PDA deposited on the microreactor left these with the final charge of -41.20 mV, a value very close to the final charge of the first generation microreactors.

Overall, the assembly was also successful. Microreactors incorporated manganese oxide nanoparticles in a significant amount (at least 50% of the sphere appears to be coated by nanoparticles), and the structure was assembled with all the planed intermediate levels, as demonstrated by the ζ-potential variation. The consistency with the previous characterization validates the microreactor LbL method, showing consistency in results and homogenous assembly.

3.3.2.2. Enzymatic activity

Unlike the previous microreactor assay, for microreactors containing only nanoflowers, the effect of different concentrations on activity was tested. The activity in free solution was measured by the same assay as previously, where the control situation is correspondent to the sample with no antioxidant molecules present. Therefore, point 0 corresponds to the maximum amount of O_2^- produced by the assay, and normalized to 100% of ion. Four independent batches of microreactors were assembled (N=4) and had their activity evaluated in the same range of concentrations. Samples were incubated with the assay reagents for 20 min at 37°C and then had their absorbance at 450 nm read by microplate reader.

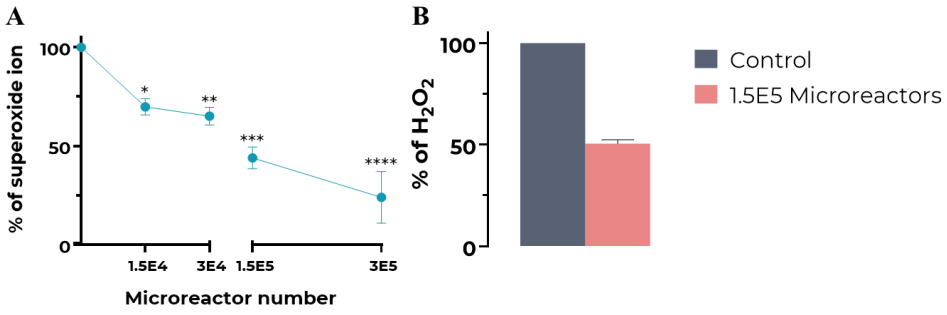

Figure 12: Enzymatic activity of second generation microreactors. A) Concentration dependent SOD-like activity of microreactors. Each data point corresponds to the indicated amount of microreactors containing only Mn_3O_4 nanoflowers in the reaction. 100% correspond to a situation of O_2^- releasing reaction with no antioxidant counterbalance and all data is normalized to its 100% of O_2^- produced by the reaction. Values of each data points represent the amount of not scavenged O_2^-. All data presented as mean ± SEM, **N=4**, * p<0.05, ** p<0.01, *** p<0.001. **** p<0.0001 compared to control, one-way ANOVA with Dunnett multiple comparison test. **B)** Catalase activity of 1.5E5 microreactors in a solution. Control corresponds to 100% of H_2O_2 in the solution, with no antioxidant activity. Data presented as mean ± SEM, **N=2.**

As shown in **figure 12A**, even the lowest tested concentration showed significant reduction in the amount of O_2^- in the solution. When incubated with 1.5E4 of microreactors, only 69.84±4.124% (mean ± SEM) of ion remained. That corresponds to approximately 30% of ion concentration decrease. When the amount of microreactors is increased double fold, the remaining amount of O_2^- equals 65.13±4.450%. For the lower quantity of microreactors, the doubling of the concentration does not cause doubling of ion scavenging activity. When the concentration is raised ten-fold, to 1.5E5 microreactors, the remaining ion equals to 43.94±5.537% of the control, which equals to 56% ion consumption. Finally, when increasing the amount to 3E5 microreactors, the activity nearly doubles, with only 24.03±13.12% of superoxide remaining in the reaction. The highest tested amount of microreactors scavenges approximately 76% of the ion in the reactors. However, it can be noted that the error also increases notably, when compared to previous values. A possible explanation for this phenomenon can be that the high concentration of microreactors reaches an antioxidant activity saturation, and the reaction reaches an equilibrium. As each assay was independent from the other and only the high concentration revealed this behaviour, reaction saturation could possibly explain the elevated variability in its maximum capacity for scavenging the ion, and its decreased variability for lower concentrations of microreactors (*320*).

Only one concentration of microreactors was tested to evaluate catalase-like activity (**figure 12B**). The initial H_2O_2 concentration by the assay is 400 μM of H_2O_2. After incubating the solution for 30 minutes with 1.5E5 microreactors, the assay measured 50.44±1.958% of H_2O_2, when compared with the positive control. While still representing considerable level of enzymatic activity, these levels are lower than those observed with free nanoparticles in the working solution concentration (2.405±0.4427% of remaining H_2O_2) and SOD-like activity for the same number of microreactors (43.94±5.537%of remaining O_2^-).

As the concentrated stock of produced microreactors usually yields nE7 microreactors, tested concentrations are 100 to 1000 times lower than the stock solution, and yet have a high enzymatic activity. This also shows that, if not all, most part of the nanoparticles are successfully integrated in the structure and do not lose their enzymatic activity in fully assembled microreactors.

3.4. SH-SY5Y neuroblastoma cell line

SH-SY5Y is a human (*Homo sapiens sapiens)* neuroblastoma cell line. Provenient from bone marrow, these usually grow while adhering to a surface and in suspension when plated. This cell line is widely used in studies involving neuronal cells. Exempt of any specialized stimulus, cells proliferate constantly, expressing an undifferentiated neuronal phenotype. In undifferentiated form, SH-SY5Y are characterized by a neuroblast-like morphology with little to none truncated processes. Although undifferentiated cells express low levels of mature neuronal cells biomarkers and have poor morphological development, they were found to be adequate for cytotoxicity studies as these do not require specific protein expression.

3.4.1. Nanoparticle and liposome toxicity in SH-SY5Y neuroblastoma cells

As discussed in the introduction, liposomes are organic vesicles and are usually biocompatible. The application of metal and metal oxide nanoparticles, in their turn, is still hindered as, despite having amazing properties, they are usually cytotoxic. Manganese, even when encapsulated in many metalloproteins and enzymes, is a heavy metal. In toxicology and environmental studies, there is plenty of evidence of the impact of manganese overexposure and associated risks (*213*, *225*). But, as much as manganese oxide nanoparticles differ from manganese enzyme co-factors, they also differ from free elemental manganese. As discussed before, the role and characteristics of nanoparticles are majorly dependent on their form. Mn_3O_4 nanoflowers are composed of a conglomerate of 2D manganese oxide nanoplates, which endows them with many sharp edges and a rough surface. While this is usually an advantage for enzymatic purposes, it can be quite hazardous for cells that will come in contact with the particles. Free nanoflowers are also much smaller than microreactors and, possibly, can penetrate cells, causing toxicity and oxidative stress from the inside, as well as membrane damage and rupture. While the concentration dependent study aims to evaluate nanoflower toxicity in detail, it is expected for nanoflowers to have a more detrimental effect on cells, when compared with same concentrations of liposomes.

The toxicity of isolated nanoparticles and liposomes was accessed by the incubation of SH-SY5Y neuroblastoma cells (≈70-80% of confluence) with nanoparticles or liposomes for 24 hours. Cell viability was determined by CCK8 cell counting kit. Samples were performed in three (two highest concentration values) to eight independent cultures (N=3-8). Equal concentration of each nanomaterial was

compared with non-treated cells as the negative control and between each other (**figure 13**).

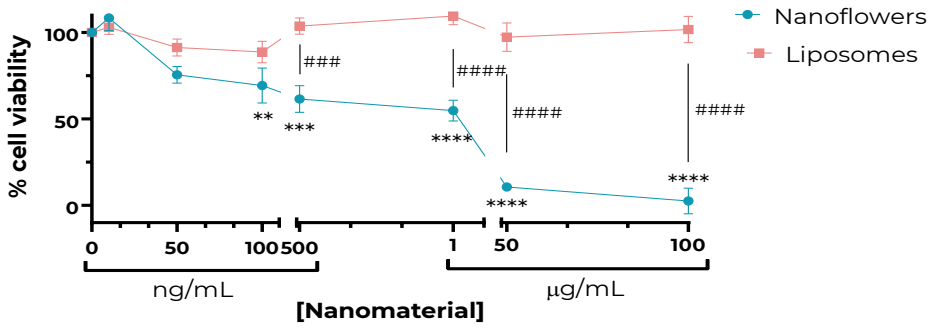

Figure 13: Concentration-dependent nanomaterial toxicity evaluation in SH-SY5Y neuronal cell line. All data presented as mean ± SEM, **N=3-8**. All data values are normalized to zero as the control situation and considered to be 100% of cell viability. Statistics represented with * is related to significancy of the viability decrease of each individual material when compared to the control (non-treated cells). ** p<0.01, *** p<0.001, **** p<0.0001. Statistics with # represent the significancy when comparing the two nanomaterials. The study is done by comparing the viability values of cells when treated with the same concentration of liposomes or nanoflowers. ### p<0.001, #### p<0.0001, one-way ANOVA with Sidak multiple comparison test.

The lowest concentrations evaluated were 10 ng/mL and 50 ng/mL, with no significant cytotoxic effects, neither by nanoparticles nor liposomes. All percentages are presented as a mean ± SEM. When treated with 10 ng/mL of Mn_3O_4 nanoflowers or liposomes, cell viability was 108.4±7.241% and 103.0±4.150%, respectively. Treatment with 50 ng/mL resulted in 75.59±4.828% of cell viability with nanoparticles, which is a visible decrease in relation to smaller concentration, despite not statistically significant different. As for liposomes, viability held on 91.38±4.955%, still considered as a non-significant nor presenting a tendency for cell toxicity. However, starting from the concentration 100 ng/mL, the differences become more prominent. The liposome dose-response curve maintains a linear pattern with no viability decrease even in higher treatment concentrations. The highest used concentration was 0.1 mg/mL and cell viability remained at 101.7±7.626% showing none to very low toxicity of liposome encapsulated enzyme. Manganese oxide nanoparticles, on the other hand, starting from 100 ng/mL, showed 69.34±10.10% of viable cells that represents around 30% of viability loss and is already a significant decrease. From that point on, the toxicity exhibited by nanoparticles continuously increases. When nanoparticle concentration in cells is increased to 500 ng/mL, cell viability decreases to 61.59±7.729% and by doubling the concentration to 1 µg/mL, it decreases to 54.85±5.984%. By significantly increasing treatment concentration, the viability also drops. Upon 50 µg/mL and 0.1

mg/mL treatments, the viability of the cell line decreased down to 10.64±1.083% and 2.529±7.429%, respectively, representative of the death of almost entire cell population.

The effect of treatments with equal concentrations of liposomes and nanoparticles on cell viability was also evaluated. When using concentrations up to 100 ng/mL of the nanomaterial, these seem to be very close and to follow the same influence pattern over cell viability. Starting from the 100 ng/mL concentration point, nanoparticles start showing first signs of cytotoxicity, showing a statistically significant decrease in cell viability, while the liposome remain non-toxic. Furthermore, as the tested concentration of nanomaterials is increased, the disparity between the effect of both on cell viability becomes more pronounced. For 500 ng/mL of nanomaterials, the decrease in viability caused by nanoparticles is far more accentuated when compared to liposomes ($p<0.001$). From that point on, as the concentration increases, the difference is more accentuated reaching the maximum level of significancy of $p<0.0001$.

From the obtained data, liposomes do not seem to be cytotoxic to the cell, at least for short term exposure. On the other hand, nanoparticles were revealed to be cytotoxic from very low concentrations. When testing the concentration dependent activity in free solution, while catalase-like activity required lower concentrations of nanoflowers, with a considerable scavenging effect from the 100 ng/mL (**figure 7B**), the first concentration to have a significant superoxide scavenging activity was 0.1 mg/mL (**figure 7A**). Even 1 µg/mL of nanoparticles did not have significant superoxide activity, and the concentration that first was shown to have significant cell viability decrease was 100 ng/mL, a concentration ten times lower. However, it is also important to consider that in biological systems, the ROS concentrations are much smaller than the ones purposely produced by an enzymatic assay. The obtained results were compared with those from a study that analysed Mn_3O_4 nanoflowers in detail, characterizing their activity and cytotoxicity in the SH-SY5Y neuroblastoma cell line as well (*246*). They report an absence of nanoflower toxicity, within a range of timepoints going up to a maximum incubation time of 24 hours. However, the tested range of concentrations is 10-50 ng/mL. This data goes along with the experimental data of this study, as nanoflowers maintain nontoxic profile until 100 ng/mL. The main issue was whether these low concentrations are able to have a significant enzymatic activity, and the referred study was indeed able to find a significant ROS consumption within the low range concentrations.

Free solution activity is very different from *in situ* activity of nanozymes. The activity may be expressed in a different manner or a concentration range necessary for an optimal enzymatic function may vary. Further studies shall be conducted but it is clear that the use of pure nanoparticles, and Mn_3O_4 nanoflowers in particular, comes with an associated risk that must be assessed. Even with the presented results, these are to be considered as very preliminary, and do not take into account the vast amount of variables that are relevant when studying its effect on the central nervous system or a general biological system.

3.4.2. First generation microreactors toxicity in SH-SY5Y neuroblastoma cells

When integrated into the microreactors, nanoflowers and liposomes are masked by more biocompatible polymers. While for liposomes this may not be as essential as previously seen, for nanoflowers it would be indispensable when considering its applications to living systems. While assembling microreactors, the purpose is not only to integrate a variety of active principles and create a complex system but also to enhance this system by allowing the use of materials that would be unusable under normal circumstances. If any, microreactor toxicity is expected to be lower than that induced by nanoflowers alone, and thus allow the use of enzymatically relevant concentrations of liposomes and nanoflowers (1.25 mg/mL and 0.5 mg/mL respectively).

Similarly to what was previously done, the toxicity of first generation microreactors (Mn_3O_4 nanoflowers and liposome encapsulated SOD) for cells was accessed by incubating SH-SY5Y neuroblastoma cell line (≈70-80% confluency) for 24 hours with different concentrations of microreactors and assessing the cell viability afterwards. As microreactors are counted in a way that allows the determination of the exact number of particles, rather than concentration per mL, four different microreactor amounts were tested (**figure 14**) in duplicates in 4-5 independent assays (N=4-5).

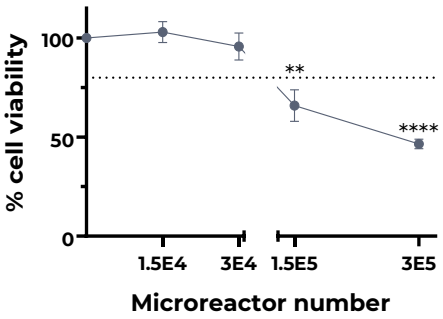

Figure 14: Concentration-dependent first generation microreactors cytotoxicity study in SH-SY5Y neuroblastoma cell line. Four different concentrations of liposome and nanoflower containing microreactors influence on cell viability, upon 24h exposure. All data is normalized to point 0 which corresponds to the viability of untreated cells. Horizontal dashed line corresponds to 80% of cell viability established as a threshold for maximum cell viability decrease. All data presented as mean ± SEM, **N=4-5**, ** p<0.01, **** p<0.0001, one-way ANOVA with Dunnett multiple comparisons test.

By using CCK8 counting kit, it was observed that lower amounts of microreactors cause no loss of cell viability, maintaining cell viability above 80% for up to 3E4 microreactors per well. When incubated with 1.5E4 microreactors, cells show 103.5±5.296% of cell viability (mean±SEM), and with 3E4 microreactors per well, 95.68±6.777% of cell viability, when compared with control situation. However, when the amount of microreactors rises up to 1.5E5, the viability drops to 65.89±7.949%, and when it is raised to the double, only 46.53±2.442% of cells are considered viable, when analysed in function of non-treated cells.

As previously used CCK8 assay is directly dependent on the number of viable cells, a lower absorbance could mean either toxic effect or a lower total number of cells – a factor with high impact when studying a constantly proliferating cell line. As the assay does not allow to differentiate direct cell death from the proliferation inhibition, the cell viability was also evaluated by PI staining. The purpose was to distinguish cell death from inhibition of cell proliferation as this method allows differentiating them. PI penetrates cells with a damaged membrane and stains the nucleus. Only if the cell already has a damaged membrane, will it be able to breach it and enter the intracellular space. However, as PI's functional principle is to intercalate in DNA, it has a positive charge. Microreactors were previously demonstrated to have a negative charge. Because of this, propidium iodide instead of entering the cell or being washed out in the posterior steps, interacted with microreactors, remaining outside the cells, and compromising the assay. No conclusive results about the microreactors toxicity were taken with this study.

Overall, high concentrations of microreactors cause a decrease in cell viability, even though the pathway of action is unknown. Not only, but it is also important to take into account that this assay in particular only considers the pure amount of microreactors, not the number of cells exposed to the reactors.

3.4.3. Second generation microreactors toxicity in SH-SY5Y neuroblastoma cells

After characterizing and testing in free solution the second generation of microreactors, containing only nanoparticles, their toxicity was tested in the SH-SY5Y cells. Following the same pattern, once cells reached ≈80% confluence, they were incubated with microreactors for 24 hours. The viability was assessed by the CCK8 cell counting kit (**figure 15A**). While for the first generation microreactors the toxicity of fixed number of microreactors was tested, second generation took into account the number of cells in the assay. Accounting for that, cell viability studies for the second generation microreactors were done for different microreactors to cells ratios. As reported value of cell confluency is 1E6 cells per cm^2 (*321*), a theoretical value of cells at the moment of incubation is calculated and used for microreactor:cell proportion. Cell viability is expected to be similar to the previous microreactors, as the main cytotoxic component of the microreactors: nanoflowers is still present and liposomes showed high biocompatibility, even in free form.

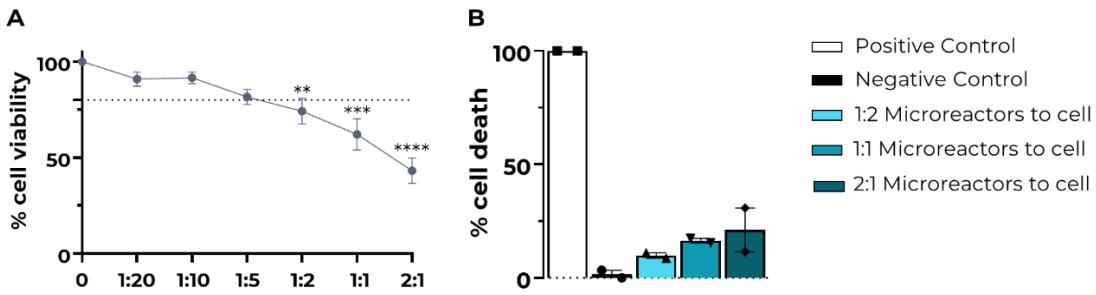

Figure 15: Second generation microreactors cytotoxicity assessment in SH-SY5Y neuroblastoma cells. A) Concentration dependent microreactors influence on SH-SY5Y cell viability upon 24h exposure. All data is normalized to point 0 which corresponds to the viability of untreated cells and is used as the negative control of the assay. Horizontal dashed line corresponds to 80% of cell viability established as a threshold for maximum cell viability decrease. All data presented as mean ± SEM, **N=6**, ** p<0.01, *** p<0.001, **** p<0.0001, one-way ANOVA with Dunnett multiple comparison test. **B)** Microreactors toxicity assessment. Trypan blue cell staining allows exact count of dead cells by penetrating compromised cell membrane. Each data value is normalized internally; percentage corresponds to the number of dead cells to total amount of cells in the sample. Positive control is representative of 100% cell death obtained by treating cells with lysis buffer. Negative control corresponds to untreated cells. All data presented as mean ± SEM, **N=2**.

Threshold of cell viability was established at 80%. Below this value the cell loss is too significant not to be considered. Lower range of microreactor to cell ratios, including 1:20, 1:10 and 1:5 microreactors per cell showed to significant decrease in cell viability. A significant decrease was observed in the **figure 15A** between 1:5 and 1:2 microreactors to cells ration. While 1:5 ratio cell shows 81.55±4.351% value representant of non-significant cell viability loss, 1:2 ratio cell viability value decreases to 74.15±6.668%, below the established threshold. From 1:5 and on, cell viability further decreases, 1:1 ratio rendering 62.11±8.143% of cell viability and the last value referring to 2 microreactors to each cell with 43.17±6.569% of untreated cells viability.

Given this information, another question arises. Are the microreactors actually directly cytotoxic? Some cytotoxicity can be expected as the nanoparticles that these microreactors incorporate were previously shown to be extremely toxic (**figure 13**). In addition, the microreactor core is a relatively big particle (7 µm) and, when co-incubated with cells, it also occupies the physical space that cell might need for growth. Or, without causing a direct toxicity effect, the relatively big particles can interact with cells, depositing on top of them and physically constraining them (*322*). The previously used CCK8 kit does not allow to differentiate between cellular death and the proliferation inhibition. By its principle, all viable cells conduct the enzymatic reaction that produces a colorimetric dye that is later quantified by a spectrophotometer. Reduction in absorbance can be due to the loss of viable cells or just a lesser amount of cells to react. This issue is especially prominent in continuously replicating cell line cultures. The assay used to distinguish cell death from proliferation inhibition standardly is PI staining. However, as explained before, PI staining is compromised by its reaction with the microreactors. Therefore, an alternative method was used. Trypan Blue staining of cells allows to count the number of dead cells in a total number of cells. The conditions determined to have a significant viability reduction by the previous assay (1:2; 1:1 and 2:1 - **figure 15A**) –had their toxicity assessed by the Trypan Blue and the results are presented in the **figure 15B**. The assay was performed in two independent cultures (N=2).

First, the positive control was done by lysing the cells with RIPA buffer. As RIPA is a detergent, it destroys cell membrane, therefore allowing trypan blue to enter and stain the cell. In all the counted samples, all the cells were fully stained and the cell death rate equal to 100%. Negative control is correspondent to cells with no treatments. In this case cells presented 1.680±1.680% (mean ± SEM) of cell death, which can be assumed to be both a normal amount of cell death that spontaneously occurs in any cell culture and cell death associated with the dissociation and sampling of the

cells for the staining. When incubated with 1:2 microreactors, the previous result shows 26% of cell viability reduction. However, when accounting for cellular death alone, the results are seen in a new perspective. The pure toxicity of 1:2 microreactors to cells is 9.889±1.153% while the other value obtained by the CCK8 assay is most likely due to cell proliferation inhibition. The same pattern in observed in higher microreactors concentration, where 1:1 ratio is responsible for 16.39±0.9791% of cell death, as opposed to CCK8 registered 38% cell viability reduction and 2:1 ratio with 21.16±13.59% of cells dead and 60% cell viability reduction. As the cells proliferate less when in contact with microreactors, the difference between general cell viability evaluation and specific cell death count is expected and previously described in a similar situation (*277*).

3.4.4. Microreactors rescuing SH-SY5Y neuroblastoma cell line from H_2O_2 induced oxidative stress.

After assessing the possible negative effects of microreactors, next assays focused on the positive effects that these might have *in situ*, such as rescuing cell viability or scavenging reactive oxygen species. Having in consideration the toxicity assays, 1:10 microreactors to cells ratio was chosen as an optimal point to avoid any cytotoxicity and reduce the effect of proliferation inhibition. Enzymatic activity of microreactors was previously demonstrated in free solution but not yet in cells and actual oxidative stress scenario.

Exposure concentrations were chosen from previously made concentration dependent cell toxicity scan (**supplementary figure I**) in order to cover the concentrations from the point at which the H_2O_2 treatment starts exhibiting the toxic effect, up to the near complete cell population death. Cell viability was evaluated by incubation of cells with a range of H_2O_2 exposure with or without the presence of microreactors for four hours. Cell viability decrease was normalized internally to negative control in each group (with or without microreactor exposure).

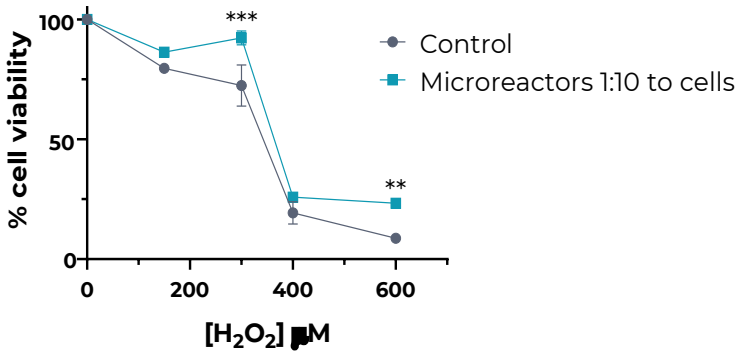

Figure 17: Concentration dependent H_2O_2 induced cytotoxicity with and without microreactor exposure. Each of the conditions: no microreactors and 1:10 ratio was submitted to H_2O_2 treatment for 4 hours in the same concentration range and cell viability evaluated. Data normalization was done internally for each group, for no H_2O_2 treated cells as 100% of cell viability. Statistical analysis was done comparing point at the same H_2O_2 treatment concentration. All data presented as mean ± SEM, **N=3-4,** ** p<0.01, *** p<0.001, one-way ANOVA with Sidak multiple comparison test.

H_2O_2 cytotoxic effect was found to be preventable by the presence of microreactors in the treated cell culture. While the lowest concentration showed no significant difference, it is mostly probably owed to the fact that 150 µM H_2O_2 associated cell death is not as prominent, as the cells have the ability to counteract the insult with their own antioxidant defences. However, from the 300 µM, cell death becomes more accentuated, and the scavenging of the H_2O_2 by microreactors rescues some of the cell viability. While cells alone showed 72.41±8.599% of cell viability, compared to 100% control, when in presence of microreactors, cell viability value was 92.23±2.884%. Unexpected result was seen at 400 and 600 µM treatment. While 400 µM H_2O_2 showed no significant difference between cell with or without the presence of microreactors, 600 µM once again was able to significantly rescue the cell viability. While cells alone had 8.694±2.004% of cell viability, translated roughly into 91% of cell viability loss, cells in the presence of microreactors registered 23.31±0.9905% of cell viability. As so, in the 300 µM condition, microreactors were able to rescue approximately 20% of the cell population from oxidative stress, while when exposed to 600 µM, the difference was approximately 15%.

The obtained results are also in accordance with published data, that, while using platinum nanospheres that also have antioxidant activity, were able to support SH-SY5Y neuroblastoma cells from H_2O_2 induced cellular death, registering higher viability values in their presence. The study used equivalent microreactor: cell ratio and registered difference in viability in lower H_2O_2 concentrations, while stimulating cells for 24 hours (*277*).

While it is difficult to determine the true range of capacity of microreactors to protect biological cells from hostile environments or to prevent their definite damage, it clearly demonstrates their ability of rescue to a certain degree cell viability by scavenging H_2O_2 in the media. Thus, an interesting follow up study would be to explore the threshold of microreactor scavenging capacity. While there is lack of detailed and concise data about the concentrations of H_2O_2 in the brain, it was determined that, theoretically, the concentrations can go as high as 1 mM or, in some cases, even 1.5 mM, until unreversible damage occurs (*323*). This value could be taken as a starting point for the application of microreactors in acute oxidative stress and to further explore the maximal potency of antioxidant activity of the nanoflowers.

3.5. Mixed primary cortex cell culture

3.5.1. Neuroinflammation induction

LPS is the main constituent of an endotoxin found in gram-negative bacteria cell wall, known to activate innate immune response (*324*). When inducing neuroinflammatory response in brain, LPS is usually the to go route. Numerous studies support the LPS-induced activation of microglia and astrocytes, increase in expression of inflammation-related proteins and high release of pro-inflammatory cytokines, as well as oxygen and nitrogen reactive species (*325–327*). All these factors can be detrimental to the central nervous system and the first ones to suffer the consequences are the neurons. Inflammation, and particularly LPS-induced inflammation, causes signalling disturbances, neuronal dysregulation and consequentially neurodegeneration. Besides, LPS stimulus has been related to mitochondria dysregulation and elevated production and accumulation of intracellular ROS, which causes further cell degeneration (*328*, *329*).

Cells were stimulated with 100 ng/mL LPS, the most frequently reported dose used in cell culture neuroinflammation studies (*327*) and 1 µg/mL of LPS, in order to compare if any significant changes would occur. 24 hours after the stimulus, the intracellular amount of O_2^- was evaluated by the DHE fluorescent dye. DHE has the ability to penetrate cell membrane, being found in its unreacted form in the cytoplasm. In the presence of O_2^-, oxidized DHE binds to DNA, creating a highly fluorescent compound. This way higher amount of oxidants (ROS) in the cytoplasm is translated into a higher fluorescence signal.

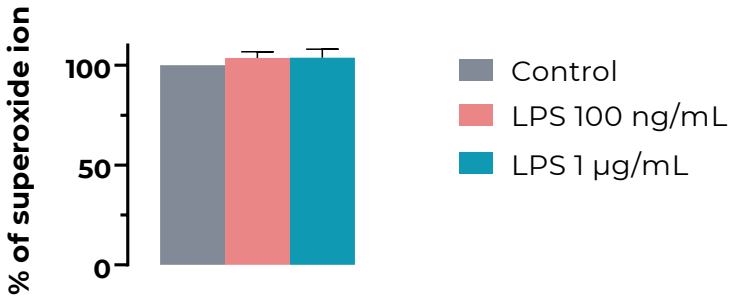

Figure 18: Evaluation of intracellular O_2^- production in mixed primary cultures treated with LPS. A non-treated control and samples treated with 100 ng/mL and 1 µg/mL LPS for 24 hours were incubated with DHE fluorescent dye and had their fluorescence correspondent to oxidized product measured at Ex_{535}/Em_{610} nm. The non-treated sample fluorescence was considered as 100% control and treated cells normalized to it. All data presented as mean ± SEM, **N=5,** no significant differences found.

As seen at the **figure 18**, cells that were stimulated with LPS showed no difference from the untreated ones. As the amount of O_2^- was normalized to the control (untreated cells), the measured fluorescence corresponded to 100% of the ion. Stimulated with 100 ng/mL and 1 µg/mL cells showed 103.6±3.079% and 103.7±4.296% (mean ± SEM) of O_2^-, respectively. Almost null variance in the ROS amount in the cytoplasm suggests that LPS was unable to induce oxidative stress and overproduction of ROS by the cells.

From this analysis alone it was unclear the reason for this lack of response and any significant variation in reactive oxygen species production. As referenced before, cortex cell cultures were previously described to have a rise of oxidative stress and ROS production when treated with LPS (*329*, *330*). The obtained data can be representative of various issues, such as the assay inability to detect ROS variations with enough sensitivity, compensatory cell mechanisms, or a general inability of the cell culture to respond strongly to LPS. The last reason is seen as the most probable and could be due to the lack of cells expressing the Toll like receptor 4 (TLR4) to which LPS binds and induces the activation and inflammatory signalling. In a cortical primary culture in question, the only cells expressing TLR4 would be microglia (*331*, *332*). There are some sparse studies of astrocytes expressing TLR4 receptor but their ability to express constitutively the receptor is very much debated (*333*, *334*). Lack of microglia or a compromised viability or/and function of the present one would also compromise culture's ability to respond to LPS stimuli and, therefore, to promote further neuroinflammatory and oxidative stress response.

To confirm the theory, other than only ROS detection methods were used. The LPS inflammation induction was evaluated by western blot and immunocytochemistry, targeting the most common pro-inflammatory markers. In CNS, the main responsible for inflammatory and reactive responses are microglia and astrocytes (*76*). These influence majorly the process of the inflammation, regulating the pro- or anti-inflammatory patterns. When evaluating neuroinflammation in mixed cell type cultures or slices, some of the most used markers include glial fibrillary acidic protein (GFAP) for astrocytes (*335*) and Iba1 (Ionized calcium binding adapter protein 1) and cluster of differentiation 68 (CD68) for microglia (*336*). Both GFAP and Iba1 are expressed constitutively by astrocytes and microglia, respectively, but when these are activated, expression levels rise significantly and are accounted as markers of cell reactivity. CD68, in its turn, has a low basal level expression and rises to significant levels when microglia is activated. It is a glycosylated type I membrane protein only expressed by macrophages and monocytes and in CNS it is unique to microglia immunomarker (*336*).

Both immunocytochemistry (**supplementary figure II**) and western blot (**supplementary figure III**) were used in order to evaluate the expression of GFAP, Iba1 and CD68. Neither analysis showed a presence of Iba1 in cell cultures. As Iba1 is a constitutively expressed microglial marker, its absence in both analyses allows to hypothesize that mixed primary cultures are exempt of microglia. Another microglia specific marker showed somewhat contradictory results. In three independent cultures, only one had detectable by western blot levels of CD68 **(supplementary figure III**). Further confirming, samples of the same cell culture were analysed by immunocytochemistry (**supplementary figure II**) and showed low, mostly near-nuclear staining in non-treated samples and a higher intensity staining in 100 ng/mL LPS treated cells, with a co-localization of CD68 with GFAP staining. GFAP, the primary immunomarker to detect astrogliosis, in its turn, showed no increase in expression in LPS treated cultures. As no literature has previously described astrocytes expressing CD68, nor interaction between GFAP and CD68, obtained result is most likely due to unspecific interaction between antibodies.

Although more experiments must be performed to form a robust conclusion, the data obtained in this chapter strongly suggests the inability of the cell culture to respond to LPS inflammatory stimuli. The most probable cause is the lack of microglia cells or their inability to respond with inflammatory markers. As so, the primary culture protocol for inflammation model must be further tested and optimized.

3.5.2. Manganese oxide nanoparticles and first generation microreactors toxicity to primary cultures

Similar to the previous assays (chapters **3.4.1.** and **3.4.2.**), the primary culture, at DIV20 which is 24 hours prior to the culture fixation, was incubated with manganese oxide nanoparticles and microreactors at two different ratios. After the 24 hours exposure, the cell viability was evaluated by CCK8 cell counting kit and analysed, comparing the control situation (untreated cells) with the cells exposed to the nanomaterials (**figure 19**). Study was made in three independent cell cultures (N=3). As free nanoflowers have previously shown prominent cytotoxicity in the SH-SY5Y neuroblastoma cell line, it was expected to see a similar pattern in primary cultures. As nanoparticle toxicity mechanisms are straightforward, being mainly through membrane damage, toxic component release and oxidative damage, compensatory mechanisms of other cells may not be sufficient to rescue the cell viability (*184*). As for the microreactors, it was previously hypothesized that the main cell viability influence factor is a proliferation inhibition (chapter **3.4.3.**). As such, primary culture may show significantly less of a viability loss and only show significant cell death at highest microreactor to cell ratio – 2:1.

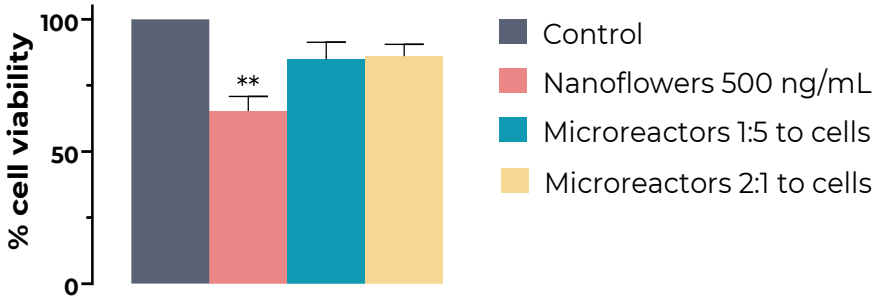

Figure 19: Primary culture cell viability when exposed to nanoflowers and microreactors. Cell were treated with either 500 ng/mL pure nanoflowers or 1:5 and 2:1 ratio of microreactors per cell for 24 hours and their viability was evaluated by CCK8 cell counting assay. Non-treated cells were considered as 100% of cell viability and treated samples normalized to the control. All data presented as mean ± SEM, **N=3**, ** p<0.01, one-way ANOVA with Dunnett multiple comparison test.

The control situation corresponds to cells with no treatments and as so, assumed as the 100% viability and other experimental conditions viability is calculated in its function. When cells are incubated with pure Mn_3O_4 nanoflowers 500 ng/mL, cell count equals to 65.33±5.472% (mean ± SEM) which corresponds to approximately 35% of loss viability. This result shows accordance to toxicity observed in neuronal cell line when incubation with same nanoparticle concentration showed a ≈38% decrease in cellular viability (**figure 13**).

As the cell number for primary culture is regulated, the amount seeded when culturing is assumed to be the final amount of the cells in the well. Thus, the microreactor ratios of 1:5 and 2:1 microreactors to cell correspond to 3E4 and 3E5 microreactor count, respectively. These concentrations were also previously tested in SH-SY5Y cell line (chapter **3.4.2.**). None of the microreactor concentrations showed a significant viability decrease. Cells treated with 3E4 microreactors showed 84.83±6.444% viability and 10x increase concentration (3E5 microreactors) 86.02±4.454%. When compared to the results obtained in SH-SY5Y cell line, these presents accordance to trypan blue viability assays in the neuronal cell line that demonstrates that the presence of microreactors in the culture induces very low levels of cell death and as so, deemed as non-cytotoxic. In the meantime, a hundred times lower concentration of pure nanoflowers than the one used for microreactor production, cause direct toxicity to the cells. That further demonstrates the integration of nanoparticles in a protective and biocompatible structure significantly ameliorates the toxicity of the material, allowing its use in high enough concentration without an acute damage to the system.

3.5.3. Nanoparticle and microreactor activity upon reactive oxygen species

Reactive oxygen species generation and induction or, at the opposite, contra-action of nanoparticles and first generation microreactors (incorporating both Mn_3O_4 nanoflowers and liposome encapsulated SOD) was tested by treating primary cultures with 100 ng/mL and 1 µg/ml of LPS as inflammatory stimuli, and with nanoflowers (500 ng/mL) or microreactors (2:1 reactor to cell). While, as demonstrated previously in the chapter **3.5.1.**, stimulation with LPS alone does not induce detectable increase of ROS in the culture, the aim of this study was to unravel whether inflammatory response modulates, in any way, the cellular response to nanoflowers and microreactors.

While microreactors are targeted into scavenging ROS in the extracellular space, these also incorporate a highly cytotoxic compound (nanoflowers). The microreactor number applied in this assay was the 2 microreactors per 1 cell this concentration showed an approximately 21% of direct cell death on the neuroblastoma cells and approximately 14% of cell death on the primary cultures. Thus, it is expected to observe some degree of cytotoxic response, possibly through oxidative stress and elevation of intra and extracellular ROS:

Free nanoflowers are both more cytotoxic and reduced in size, possibly having a capacity to enter the cells and exhibit their toxicity intracellularly, whereas

microreactors, while also containing nanoflowers, retain them in their structure in the extracellular space, promoting the catalytic activity and avoiding, to a degree, nanoflowers toxicity, as demonstrated in SH-SY5Y studies. While microreactors showed a positive enzymatic activity is scavenging the extracellular ROS; this may not be representative of their behaviour for mixed cell types and for individual cell response to their presence. They can both show scavenging of reactive species or, *au contraire*, no activity or generation of reactive oxygen species due to toxicity and induction of oxidative stress by exposure.

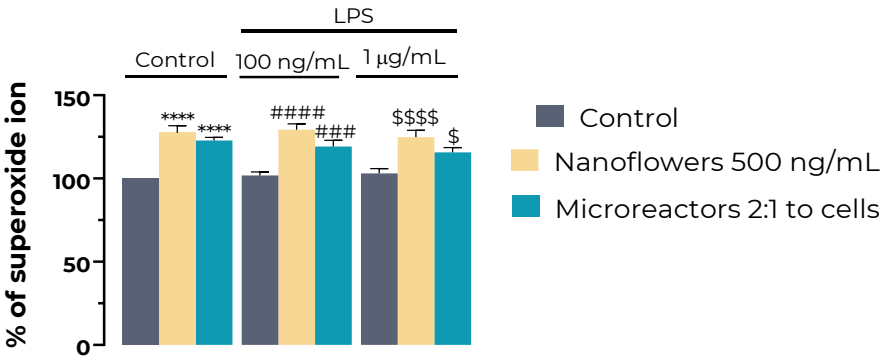

Figure 20: Intracellular reactive oxygen species detection with and without the presence of neuroinflammation stimulus and nanomaterials exposure in mixed primary cultures. Primary culture was treated with LPS, nanoflowers and microreactors 24 hours before the analysis, simultaneously. Intracellular O_2^- amount was estimated by incubating cells with cell permeable superoxide specific DHE fluorescent dye and measuring the fluorescence Ex_{535}/Em_{610} nm. All data normalized to the non LPS and nano- and micromaterial sample. Three test groups contained no inflammation induction, 100 ng/mL of LPS treatment and 1 µg/mL LPS treatment. Each group contained a no nano and micromaterial exposure control, 500 ng/mL nanoflower treatment and 2:1 microreactors to cell treatment. Statistical analysis was performed inside each group where nanoflower and microreactor sample value was compared to the non-treated sample. Each symbol is specific to statistical analysis inside of the group. **** $p<0.0001$ for no LPS treated cells; ### $p<0.001$, #### $p<0.0001$ for 100 ng/mL LPS treated cells; $ $p<0.05$, $$$$ $p<0.0001$ for 1 µg/mL LPS treated cells. All data presented as mean ± SEM, **N=5**, one-way ANOVA with Sidak multiple comparison test.

Incubation of primary culture cells with nanoflowers and microreactors showed an increase of intracellular O_2^- in all situations: no neuroinflammation induction as well as both doses of LPS treatment (**figure 20**.) However, only LPS treatment showed no significant changes. The data suggests that the increase of the O_2^- is directly related to the nanomaterials exposure and possibly caused by it. For example, when exposed to free nanoflowers, superoxide levels rise from the normalized 100% to 127.5±4.178%, 129.3±3.493% and 124.8±4.096% (mean ± SEM) when treated with 0, 100 ng/mL and 1 µg/mL of LPS, respectively. Similarly, when exposed to microreactors, a lesser, yet also an increase in O_2^- is registered. In the control group, 2:1 microreactor amount rises

superoxide levels up to 122.8±1.927% when compared to a no microreactor condition, which translates in roughly 23% ion rise. When exposed to the same amount of microreactors but also 100 ng/mL and 1 μg/mL of LPS, intracellular ion levels are registered to be 119.3±3.493% and 115.7±2.868%, respectively. No significant changes were observed in nanoflower or microreactor exposure effect whether cells were treated or not with LPS.

The generation of reactive oxygen species by nanoparticles and such is not an unprecedented situation. This was described to happen in various literature sources for a very large range metal and metal oxide nanoparticles. Often, same metal or metal oxide composition yielded different activities depending on a number of factors. Some nanoparticles can have both pro-oxidant and antioxidant activities (*337*, *338*). Many nanoparticles described as effective reactive oxygen species showed very different results with only small alterations such as environments, morphology, size, or concentration. Even when studying manganese oxide nanoparticles, radial differences were found, as depending on the environment they could express both pro- and anti-oxidant activities (*305*). Microreactors can either generate reactive oxygen species or act indirectly, inducing oxidative stress in the exposed cells. While viability assay revealed it is not sufficient to cause a significant damage and lead to cell death, induction of oxidative stress can be damaging in a long-exposure scenario. It also contra-acts the purpose of the microreactors in the culture – to scavenge the reactive oxygen species.

4. Conclusions and future perspectives

The presented work had the aim to develop a cell mimicking microreactor with an ability to target and scavenge ROS and prevent oxidative stress damage in cells.

As the aim of the microreactor is to express an antioxidant activity that would be able to support the compromised or insufficient activity of a biological cell, the microreactor theoretical design approached the issue from an enzymatic point of view. As active principles, liposome-encapsulated SOD and Mn_3O_4 nanoflowers were chosen. While SOD is a powerful antioxidant, targeting the primary ROS – O_2^- ion, Mn_3O_4 nanoflowers were previously shown to display the enzymatic activity of all three main antioxidant enzymes: SOD, CAT and GPx enzymes, scavenging both O_2^- and H_2O_2 ions. The opposition of the biological and synthetic means to obtain the catalytic entity can be seen as the focal point of artificial cell development and the advancements in synthetic biology. While liposomes and biological enzymes are much more known and conventional for the use, nanoparticles are still largely an incognita for the biological applications.

In accordance with a published study, manganese oxide nanoparticles showed a flower-like morphology and a good colloidal stability. They showed both SOD and CAT activity, however requiring higher concentration that the original study. When comparing SOD activity of nanoflowers with liposome-encapsulated SOD, the prior showed higher activity, much probably owed to low liposome encapsulation rates. However, in SH-SY5Y neuroblastoma cell line nanoflowers, unlike liposomes, showed accentuated cytotoxicity in low concentrations, showing the impossibility of application of pure nanoflowers in a biological systems. By that, the application of either one of the materials directly in oxidative stress scenario would not be effective.

Minimal cell mimics – microreactors were assembled in order to incorporate both liposome encapsulated SOD and Mn_3O_4 nanoflowers. LbL deposition allowed to create multilayer structure, incorporating, and stabilizing both active cargos, while also augmenting their biocompatibility by the use of adequate polymer films. Assembled microreactors showed SOD-like enzymatic activity and good cell viability results in SH-SY5Y neuroblastoma cell line, showing that they allow the nanomaterial to retain their activity, while also attenuating nanoflower toxicity. Primary mixed cultures showed a similar toxicity results when incubated with free nanoflowers and microreactors, however with a twist. While nanoparticles showed an accentuated toxicity that microreactors did not, both caused a significant rise in O_2^- intracellular ion. While this

was not detrimental for cells in the tested period of time, further studies of the phenomenon should be performed, in order to evaluate microreactor contributions and pathway into leading cells into oxidative stress response. Nonetheless, the results of microreactors free solution activity were close to nanoflowers alone, letting to hypothesize the loss of some activity of any of the components or the inactivity of liposome encapsulated SOD enzyme.

A second generation of microreactors only included Mn_3O_4 nanoflowers as the active principle of the reactors. They retained significant SOD and catalase-like enzymatic activities while showing low amounts of cytotoxicity, where only the highest 2:1 microreactors to cell ration showed a considerable cell death and the main cause of the decrease in cell viability was due to proliferation inhibition of constantly replicating neuroblastoma SH-SY5Y cell line. More importantly, when co-incubated with SH-SY5Y cells and stimulating these with a range of H_2O_2 concentrations known to cause an oxidative stress mediated cell death, microreactors were able to scavenge the H_2O_2 from the media, rescuing the cells to some degree. The ability of microreactors to support cells in the change of environment is a successful example of minimal cell mimicry, creating an antioxidant system that would support their biological counterparts against acute oxidative stress, where biological antioxidant defences are compromised or not sufficient for the stimulus (**figure 21**).

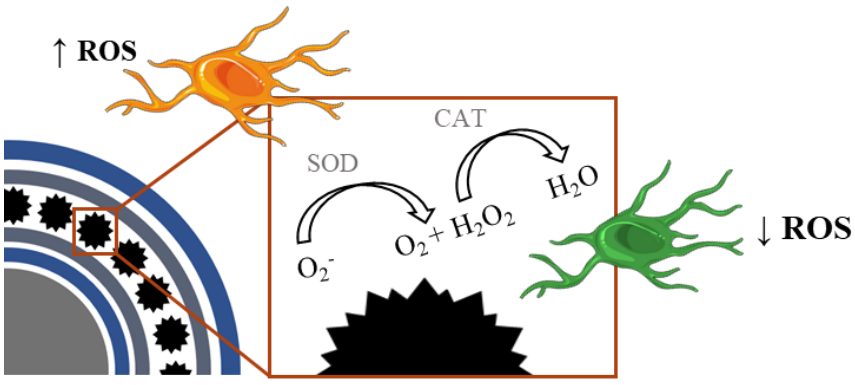

Figure 21: Schematic representation of second generation microreactor activity in cells. Exposed to high ROS concentrations, a cell suffers from oxidative stress and consequential cell death. However, in the presence of nanoflower containing microreactors, extracellular ROS are scavenged. As Mn_3O_4 nanoflowers have multienzymatic activity, they have the ability of clearance of both O_2^- and H_2O_2 ions, both detrimental to the cell. As so, microreactors have the ability to assist mammalian cells to survive changes in their environment and prevent the oxidative stress induced cell death.

Similar cell mimicry system was previously developed recurring to platinum nanoparticles as active entities of the microreactor (*276, 278*). These too, were able to rescue SH-SY5Y neuroblastoma cells from oxidative stress induced damage (in addition to ammonia caused toxicity). The presented study explored the antioxidant activity mimicry in an acute oxidative stress scenario, demonstrating the multienzymatic activity of microreactors and their ability to counteract against higher concentrations of H_2O_2, detrimental to biological cells.

Microreactors are an open field to explore. When talking about the future perspectives, further development can lead down several paths. An increase of complexity of microreactor and individualization into targeting a more specific issue is a viable route. Oxidative stress is a hallmark of many diseases, including neurodegenerative where it is involved in one way or another. However, oxidative stress is rarely the cornerstone of the disease. Adaptation of the liposomal technology, charging the cargo or use of nanozymes targeting other issues can be a beneficial step in developing microreactors as a more efficient therapeutic agent. Incorporation of ROS sensors could be a tool into theragnostic, not only preventing the ROS inflicted damage but also providing with an insight to the focal point of pathology, which can be crucial for further treatment. Modelling of a targeting system or specificity marker could also be a step up for a cell or issue specific activity and a controlled drug release activity. While there are many ideas to be explored, the standing point is to explore the cell mimicry field by raising the complexity and automaticity of assembled structures. Brainstorming of development paths could go for many more pages, exploring old and cutting edge new methods of nanotechnology applications. The terms of synthetic biology and cell mimicry charge their meaning and evolve each year, along with new developments and more and more researches investing their knowledge into exploring the world of cell mimicry and controlled replication of what was once unknown. Microreactors are a leap of faith into the exploration of enzymatic capacities of a biological cell. The fact is, microreactors where they stand, more than any therapeutic agent, are a tool. A cell mimicry system, highly adaptable to any requirement is a technology that above all are a step on a ladder for scientists, contributing for the long going conversation about the perspectives of new ways of science.

5. References

1. E. Cadenas, in *Annual Review of Biochemistry* (1989), vol. 58, pp. 79–110.
2. M. Valko, H. Morris, M. T. D. Cronin, *Curr. Med. Chem.* **12**, 1161–1208 (2005).
3. B. E. Lehnert, R. Iyer, *Hum. Exp. Toxicol.* **21**, 65–69 (2002).
4. P. Brzezinski, *Trends Biochem. Sci.* **29**, 380–387 (2004).
5. L. R. Engelking, L. R. Engelking, *Textb. Vet. Physiol. Chem.*, 219–224 (2015).
6. B. G. Malmström, *Acc. Chem. Res.* **26**, 332–338 (1993).
7. B. Chance, H. Sies, A. Boveris, *Physiol. Rev.* **59**, 527–605 (1979).
8. A. Boveris, *Adv. Exp. Med. Biol.* **78**, 67–82 (1977).
9. M. D. Brand, *Exp Gerontol.* **45**, 466–472 (2010).
10. F. L. Muller, Y. Liu, H. Van Remmen, *J. Biol. Chem.* **279**, 49064–49073 (2004).
11. E. Zito, *Free Radic. Biol. Med.* **83**, 299–304 (2015).
12. X. Chen *et al.*, *EMBO Rep.* **19**, 1–18 (2018).
13. D. W. Christianson, *Prog. Biophys. Mol. Biol.* **67**, 217–243 (1997).
14. B. Halliwell, J. M. C. Gutteridge, *Trends Neurosci.* **8**, 22–26 (1985).
15. S. K. Jonas, P. A. Riley, R. L. Willson, *Biochem. J.* **264**, 651–655 (1989).
16. J. Cadet, J. Richard Wagner, *Cold Spring Harb. Perspect. Biol.* **5** (2013), doi:10.1101/cshperspect.a012559.
17. C. C. Winterbourn, *Nat. Chem. Biol.* **4**, 278–286 (2008).
18. H. Yin, L. Xu, N. A. Porter, *Chem. Rev.* **111**, 5944–5972 (2011).
19. A. Ayala, M. F. Muñoz, S. Argüelles, *Oxid. Med. Cell. Longev.* **2014** (2014), doi:10.1155/2014/360438.
20. J. M. C. Gutteridge, *FEBS Lett.* **172**, 245–249 (1984).
21. D. J. Betteridge, *Metabolism.* **49**, 3–8 (2000).
22. Y. Saito, K. Nishio, Y. Yoshida, E. Niki, *Toxicology*. **210**, 235–245 (2005).
23. M. Valko, C. J. Rhodes, J. Moncol, M. Izakovic, M. Mazur, *Chem. Biol. Interact.* **160**, 1–40 (2006).
24. A. Barzilai, K. I. Yamamoto, *DNA Repair (Amst).* **3**, 1109–1115 (2004).

25. D. Kulms, E. Zeise, B. Pöppelmann, T. Schwarz, *Oncogene*. **21**, 5844–5851 (2002).

26. B. S. Berlett, E. R. Stadtman, *J. Biol. Chem.* **272**, 20313–20316 (1997).

27. C. L. Hawkins, M. J. Davies, *Biochim. Biophys. Acta - Bioenerg.* **1504**, 196–219 (2001).

28. M. H. Garner, A. Spector, *Proc. Natl. Acad. Sci. U. S. A.* **77**, 1274–1277 (1980).

29. R. L. Levine, L. Mosoni, B. S. Berlett, E. R. Stadtman, *Proc. Natl. Acad. Sci. U. S. A.* **93**, 15036–15040 (1996).

30. A. Krisko, M. Radman, *Open Biol.* **9** (2019), doi:10.1098/rsob.180249.

31. M. Radman, *DNA Repair (Amst).* **44**, 186–192 (2016).

32. A. Machado, A. Ayala, E. Gordillo, E. Revilla, C. Santa Maria, *Arch. Gerontol. Geriatr.* **12**, 187–197 (1991).

33. K. R. Gopc, (2013), doi:10.1007/s10620-013-2681-2.

34. A. Bast, R. J. A. Goris, *Pharm. Weekbl. Sci. Ed.* **11**, 199–206 (1989).

35. B. Demple, J. Halbrook, *Nature*. **304**, 466–468 (1983).

36. D. L. Croteau, V. A. Bohr, *J. Biol. Chem.* **272**, 25409–25412 (1997).

37. M. Carmona *et al.*, *Nat. Commun.* **10**, 1–13 (2019).

38. A. Mirzahosseini, B. Noszál, *Sci. Rep.* **6**, 1–11 (2016).

39. S. H. Jo *et al.*, *J. Biol. Chem.* **276**, 16168–16176 (2001).

40. R. Moreno-Sánchez *et al.*, *Biochim. Biophys. Acta - Bioenerg.* **1859**, 1138–1150 (2018).

41. S. García-Santamarina, S. Boronat, E. Hidalgo, *Biochemistry*. **53**, 2560–2580 (2014).

42. M. Schieber, N. S. Chandel, *Curr. Biol.* **24**, 453–462 (2014).

43. H. Younus, *Int. J. Health Sci. (Qassim).* **12**, 88–93 (2018).

44. G. S. A. Wright, S. V. Antonyuk, S. S. Hasnain, *Q. Rev. Biophys.* **52**, e12 (2019).

45. J. Slot, H. Geuze, B. Freeman, J. Crapo, *Lab. Invest.* **55**, 363–371 (1986).

46. K. Karlsson, S. L. Marklund, *Biochem. J.* **255**, 223–228 (1988).

47. S. Imaizumi, V. Woolworth, R. A. Fishman, P. H. Chan, *Stroke*. **21**, 1312–1317 (1990).

48. M. Eugenia *et al.*, *Methods Enzymol.* **391**, 395–413 (2005).

49. P. H. Chan, S. Longar, R. A. Fishman, *Ann. Neurol.* **21**, 540–547 (1987).

50. P. Schilrreff *et al.*, *Colloids Surfaces B Biointerfaces*. **179**, 479–487 (2019).

51. R. Galovi Rengel *et al.*, *Eur. J. Pharm. Sci.* **15**, 441–448 (2002).

52. O. A. Kost *et al.*, *Oxid. Med. Cell. Longev.* **2016** (2016), doi:10.1155/2016/5194239.

53. N. L. Klyachko *et al.*, *Nanomedicine Nanotechnology, Biol. Med.* **8**, 119–129 (2012).

54. J. F. Turrens, J. D. Crapo, B. A. Freeman, *J. Clin. Invest.* **73**, 87–95 (1984).

55. B. A. Freeman, S. L. Young, J. D. Crapo, *J. Biol. Chem.* **258**, 12534–12542 (1983).

56. A. Silvia Porfire, I. Tomuţă, S. E. Leucuţa, M. Achim, *Farmacia*. **61**, 865–873 (2013).

57. X. Xu, A. Costa, D. J. Burgess, *Pharm. Res.* **29**, 1919–1931 (2012).

58. H. Nagami, N. Yoshimoto, H. Umakoshi, T. Shimanouchi, R. Kuboi, *J. Biosci. Bioeng.* **99**, 423–428 (2005).

59. W. L. Stone, M. Smith, Therapeutic uses of antioxidant liposomes. *Appl. Biochem. Biotechnol. - Part B Mol. Biotechnol.* **27** (2004), pp. 217–230.

60. S. S. Kety, *Am. J. Med.* **8**, 205–217 (1950).

61. J. N. Cobley, M. L. Fiorello, D. M. Bailey, *Redox Biol.* **15**, 490–503 (2018).

62. J. Silver, M. E. Schwab, P. G. Popovich, *Cold Spring Harb Perspect Biol.* **7**, a020602 (2014).

63. J. Choi *et al.*, *Mol. Cell. Biochem.* **442**, 187–201 (2018).

64. P. M. Sinet, R. E. Heikkila, G. Cohen, *J. Neurochem.* **34**, 1421–1428 (1980).

65. H. Sies, *Redox Biol.* **11**, 613–619 (2017).

66. J. M. Flynn, S. Melovn, *Free Radic. Biol. Med.* **62**, 4–12 (2013).

67. P. Schönfeld, G. Reiser, *J. Cereb. Blood Flow Metab.* **33**, 1493–1499 (2013).

68. C. Quijano, M. Trujillo, L. Castro, A. Trostchansky, *Redox Biol.* **8**, 28–42 (2016).

69. M. Gleichmann, M. P. Mattson, *Antioxidants Redox Signal.* **14**, 1261–1273 (2011).

70. N. Weiss, G. W. Zamponi, *Neuronal Signal.* **1**, 1–16 (2017).

71. R. D. Burgoyne, *Trends Neurosci.* **10**, 460 (1987).

72. E. M. Kawamoto, C. Vivar, S. Camandola, *Front. Pharmacol.* **3 APR**, 1–17 (2012).

73. A. A. Starkov, C. Chinopoulos, G. Fiskum, *Cell Calcium*. **36**, 257–264 (2004).

74. C. Chinopoulos, V. Adam-Vizi, *FEBS J.* **273**, 433–450 (2006).

75. N. Brustovetsky, T. Brustovetsky, R. Jemmerson, J. M. Dubinsky, *J. Neurochem.* **80**, 207–218 (2002).

76. J. M. Taylor, B. S. Main, P. J. Crack, *Neurochem. Int.* **62**, 803–819 (2013).

77. E. A. Bordt, B. M. Polster, *Free Radic. Biol. Med.* **76**, 34–46 (2014).

78. P. K. Mander, A. Jekabsone, G. C. Brown, *J. Immunol.* **176**, 1046–1052 (2006).

79. D. S. A. Simpson, P. L. Oliver, Ros generation in microglia: Understanding oxidative stress and inflammation in neurodegenerative disease. *Antioxidants*. **9** (2020), pp. 1–27.

80. H.-C. Lu, Ken Mackie, *Biol. Psychiatry*. **79**, 516–525 (2016).

81. S. D. Skaper, V. Di Marzo, *Philos. Trans. R. Soc. B Biol. Sci.* **367**, 3193–3200 (2012).

82. R. M. Adibhatla, J. F. Hatcher, *J. Biochem. Mol. Biol.* **41**, 560–567 (2008).

83. Z. Liu, T. Zhou, A. C. Ziegler, P. Dimitrion, L. Zuo, *Oxid. Med. Cell. Longev.* **28**, 3568–3573 (2017).

84. G. H. Kim, J. E. Kim, S. J. Rhie, S. Yoon, *Exp. Neurobiol.* **24**, 325–340 (2017).

85. D. Schaming, H. Remita, *Found. Chem.* **17**, 187–205 (2015).

86. C. H. Ian Freestone, Nigel Meeks, Margaret Sax, *Gold Bull.* **40**, 270–277 (2007).

87. M. Reibold *et al.*, *Nature*. **444**, 286 (2006).

88. M. Faraday, *Philos. Trans. R. Soc. London*. **147**, 145–181 (1857).

89. D. T. Thompson, *Gold Bull.* **40**, 267–269 (2008).

90. J. Turkevich, *Colloids Classif. Prop. Appl.*, 1–24 (1985).

91. J. Turkevich, P. C. Stevenson, J. Hillier, *Anal. Chem*. **1**, 18 (1949).

92. S. Bayda, M. Adeel, T. Tuccinardi, M. Cordani, F. Rizzolio, *Molecules*. **25**, 1–15 (2020).

93. A. Ali *et al.*

94. S. Griffin *et al.*, *Antioxidants*. **7** (2018), doi:10.3390/antiox7010003.

95. V. Patel, D. Berthold, P. Puranik, M. Gantar, *Biotechnol. Reports*. **5**, 112–119 (2015).

96. G. Oberdörster *et al.*, *Part. Fibre Toxicol.* **2**, 1–35 (2005).

97. D. E. Damby *et al.*, *Environ. Heal.* **16**, 1–15 (2017).

98. F. P. R., S. Y. Chou, *Bull. Museum Hist. Nat. Paris*. **96**, 493–496 (2008).

99. B. D. Gates *et al.*, *Chem. Rev.* **105**, 1171–1196 (2005).

100. A. Pimpin, W. Srituravanich, *Eng. J.* **16**, 37–55 (2012).

101. H. Wu, W. Gao, Z. Yin, *Adv. Healthc. Mater.* **6**, 1–9 (2017).

102. M. N. M. N *et al.*, *PLoS One*. **11**, 20–23 (2016).

103. P. Iqbal, J. A. Preece, P. M. Mendes, *Supramol. Chem.* (2012), doi:10.1002/9780470661345.smc195.

104. S. Zhang, *Mater. Today*. **93**, 42–48 (2003).

105. O. C. Renn, M. Roco, *Int. Risk Gov. Counc.*, 103 (2006).

106. V. Karunaratne, N. Kottegoda, A. de Alwis, *J. Natl. Sci. Found. Sri Lanka*. **40**, 3–8 (2012).

107. R. Sparrow, *J. Bioeth. Inq.* **6**, 13–23 (2009).

108. P. S. Aithal, S. Aithal, *Int. J. Eng. Manuf.* **6**, 15–25 (2016).

109. S. T. Stern, S. E. McNeil, *Toxicol. Sci.* **101**, 4–21 (2008).

110. M. N. Uddin, F. Desai, E. Asmatulu, *Environ. Chem. Lett.* **18**, 1073–1083 (2020).

111. S. Naqvi, A. Panghal, S. J. S. Flora, *Front. Neurosci.* **14**, 1–26 (2020).

112. A. K. Sharma *et al.*, *Drug Deliv. Transl. Res.* **10**, 1171–1190 (2020).

113. P. Ramos-Cabrer, F. Campos, *Int. J. Nanomedicine*. **8**, 951–960 (2013).

114. R. E. Pagano, J. N. Weinstein, *Annu. Rev. Biophys. Bioeng.* **7**, 435–468 (1978).

115. V. S. Chaudhari, U. S. Murty, S. Banerjee, *Environ. Chem. Lett.* **18**, 1803–1812 (2020).

116. H. Ijaz *et al.*, Lipid particulate drug delivery systems: A review. *Bioinspired, Biomim. Nanobiomaterials*. **7** (2018), pp. 109–121.

117. S. A. Wissing, O. Kayser, R. H. Müller, *Adv. Drug Deliv. Rev.* **56**, 1257–1272 (2004).

118. S. Shidhaye, R. Vaidya, S. Sutar, A. Patwardhan, V. Kadam, *Curr. Drug Deliv.* **5**, 324–331 (2008).

119. S. Banerjee, J. Pillai, *Expert Opin. Drug Metab. Toxicol.* **15**, 499–515 (2019).

120. V. P. Torchilin, *Pharm. Res.* **24**, 1–16 (2007).

121. Y. Lu, E. Zhang, J. Yang, Z. Cao, *Nano Res.* **11**, 4985–4998 (2018).

122. S. Kim, Y. Shi, J. Y. Kim, K. Park, J. X. Cheng, Overcoming the barriers in micellar drug delivery: Loading efficiency, in vivo stability, and micelle-cell interaction. *Expert Opin. Drug Deliv.* **7** (2010), pp. 49–62.

123. N. Düzgüneş, G. Gregoriadis, *Methods Enzymol.* **391**, 1–3 (2005).

124. G. Gregoriadis, *FEBS Lett.* **14**, 95–99 (1971).

125. G. Bozzuto, A. Molinari, *Int. J. Nanomedicine*. **10**, 975–999 (2015).

126. H. Mishra, V. Chauhan, K. Kumar, D. Teotia, *J. Drug Deliv. Ther.* **8**, 400–404 (2018).

127. D. Bitounis, R. Fanciullino, A. Iliadis, J. Ciccolini, *ISRN Pharm.* **2012**, 1–11 (2012).

128. D. C. Litzinger, A. M. J. Buiting, N. van Rooijen, L. Huang, *Biochim. Biophys. Acta*. **1190**, 99–107 (1994).

129. R. Kumar, K. R. Aadil, S. Ranjan, V. B. Kumar, *J. Drug Deliv. Sci. Technol.* **57**, 101617 (2020).

130. G. Pamunuwa, V. Karunaratne, D. N. Karunaratne, *J. Nanomater.* **2016** (2016), doi:10.1155/2016/4535790.

131. R. A. Schwendener, *Eur. J. Drug Metab. Pharmacokinet.* **13**, 135–141 (1988).

132. J. Chen *et al.*, *Drug Dev. Ind. Pharm.* **39**, 197–204 (2013).

133. M. C. Blok, E. C. M. Van Der Neut-Kok, L. L. M. Van Deenen, J. De Gier, *Biochim. Biophys. Acta*. **406**, 187–196 (1975).

134. M. L. Immordino, F. Dosio, L. Cattel, *Int. J. Nanomedicine*. **1**, 297–315 (2006).

135. S. C. Semple, A. Chonn, P. R. Cullis, *Adv. Drug Deliv. Rev.* **32**, 3–17 (1998).

136. R R C New, *Liposomes: a practical approach* (Oxford: IRL Press, 1990).

137. J. Gubernator, *Expert Opin. Drug Deliv.* **8**, 565–580 (2011).

138. W. E. Bawarski, E. Chidlowsky, D. J. Bharali, S. A. Mousa, *Nanomedicine Nanotechnology, Biol. Med.* **4**, 273–282 (2008).

139. L. Ordóñez-Gutiérrez, F. Wandosell, *Front. Synaptic Neurosci.* **12**, 1–10 (2020).

140. B. Smith *et al.*, *J. Control. Release*. **153**, 187–194 (2012).

141. E. Casals, M. Soler, M. Gallardo, J. Estelrich, *Langmuir*. **14**, 7522–7526 (1998).

142. J. S. Beckman, R. L. Minor, B. A. Freeman, *J. Free Radicals Biol. Med.* **2**, 359–365 (1986).

143. C. Dhand *et al.*, *RSC Adv.* **5**, 105003–105037 (2015).

144. I. Khan, K. Saeed, I. Khan, *Arab. J. Chem.* **12**, 908–931 (2019).

145. A. P. Reverberi, N. T. Kuznetsov, V. P. Meshalkin, M. Salerno, B. Fabiano, *Теоретические Основы Химической Технологии*. **50**, 63–70 (2016).

146. M. Nasrollahzadeh, M. Atarod, M. Sajjadi, S. M. Sajadi, Z. Issaabadi, *Plant-Mediated Green Synthesis of Nanostructures: Mechanisms, Characterization, and Applications* (Elsevier Ltd., ed. 1, 2019; http://dx.doi.org/10.1016/B978-0-12-813586-0.00006-7), vol. 28.

147. J. Singh *et al.*, *J. Nanobiotechnology*. **16**, 1–24 (2018).

148. A. R. Tao, S. Habas, P. Yang, *Small*. **4**, 310–325 (2008).

149. K. An, G. A. Somorjai, *ChemCatChem*. **4**, 1512–1524 (2012).

150. M. Giovanni, M. Pumera, *Electroanalysis*. **24**, 615–617 (2012).

151. N. G. Khlebtsov, L. A. Trachuk, A. G. Mel'nikov, *Opt. Spectrosc. (English Transl. Opt. i Spektrosk.* **98**, 77–83 (2005).

152. R. M. S. Pereira, J. Borges, G. V. Smirnov, F. Vaz, M. I. Vasilevskiy, *ACS Photonics*. **6**, 204–210 (2019).

153. V. Kulkarni, E. Prodan, P. Nordlander, *Nano Lett.* **13**, 5873–5879 (2013).

154. S. A. Maier *et al.*, *Adv. Mater.* **13**, 1501–1505 (2001).

155. K. M. Mayer, J. H. Hafner, *Chem. Rev.* **111**, 3828–3857 (2011).

156. J. Liu *et al.*, *Materials (Basel).* **11** (2018), doi:10.3390/ma11101833.

157. D. A. French, thesis, University of Arkansas (2018).

158. J. Lermé, C. Bonnet, M. A. Lebeault, M. Pellarin, E. Cottancin, *J. Phys. Chem. C*. **121**, 5693–5708 (2017).

159. V. V Zhirnov, R. K. Cavin Iii, *Basic physics of ICT* (2nd Editio., 2015; internal-pdf://254.185.99.25/physics of ICT.pdf%0Ahttp://www.sciencedirect.com/science/article/pii/B9780323313025000028).

160. D. Sumanth Kumar, B. Jai Kumar, H. M. Mahesh, *Quantum Nanostructures (QDs): An Overview* (Elsevier Ltd., 2018; http://dx.doi.org/10.1016/B978-0-08-101975-7.00003-8).

161. G. N. Blackman, D. A. Genov, *Phys. Rev. B*. **97**, 1–10 (2018).

162. A. D. Yoffe, *Adv. Phys.* **50**, 1–208 (2001).

163. J. Estelrich, E. Escribano, J. Queralt, M. A. Busquets, *Int. J. Mol. Sci.* **16**, 8070–8101 (2015).

164. W. S. Galvãoa, D. M. A. Netob, R. M. Freirec, P. B. A. Fechined, *Solid State Phenom.* **241**, 139–176 (2016).

165. M. Allen *et al.*, *Magn. Reson. Med.* **54**, 807–812 (2005).

166. A. H. Schmieder *et al.*, *Magn. Reson. Med.* **53**, 621–627 (2005).

167. J. Pellico, C. M. Ellis, J. J. Davis, *Contrast Media Mol. Imaging*. **2019** (2019), doi:10.1155/2019/1845637.

168. A. A. M. Elsherbini, M. Saber, M. Aggag, A. El-Shahawy, H. A. A. Shokier, *Magn. Reson. Imaging*. **29**, 272–280 (2011).

169. T. Neuberger, B. Schöpf, H. Hofmann, M. Hofmann, B. Von Rechenberg, *J. Magn. Magn. Mater.* **293**, 483–496 (2005).

170. P. M. Price, W. E. Mahmoud, A. A. Al-Ghamdi, L. M. Bronstein, *Front. Chem.* **6**, 1–7 (2018).

171. M. E. Vance *et al.*, *Beilstein J. Nanotechnol.* **6**, 1769–1780 (2015).

172. X. Zhu, K. Pathakoti, H.-M. Hwang, *Green synthesis of titanium dioxide and zinc oxide nanoparticles and their usage for antimicrobial applications and environmental remediation* (Elsevier Inc., 2019; https://doi.org/10.1016/B978-0-08-102579-6.00010-1).

173. M. D. Newman, M. Stotland, J. I. Ellis, *J. Am. Acad. Dermatol.* **61**, 685–692 (2009).

174. A. J. Shnoudeh *et al.*, *Synthesis, Characterization, and Applications of Metal Nanoparticles* (Elsevier Inc., 2019; http://dx.doi.org/10.1016/B978-0-12-814427-5.00015-9).

175. S. Baruah, J. Dutta, *Environ. Chem. Lett.* **7**, 191–204 (2009).

176. J. M. Wilkinson, *Med. Device Technol.* **14**, 29–31 (2003).

177. E. Brun, C. Sicard – Roselli, *Cancer Nanotechnol.* **5**, 1–13 (2014).

178. S. Barua, S. Mitragotri, *Nano Today*. **23**, 1–7 (2014).

179. P. P. Fu, Q. Xia, H. M. Hwang, P. C. Ray, H. Yu, *J. Food Drug Anal.* **22**, 64–75 (2014).

180. M. P. Nikolova, M. S. Chavali, *Biomimetics*. **5** (2020), doi:10.3390/BIOMIMETICS5020027.

181. R. G. D. Andrade, S. R. S. Veloso, E. M. S. Castanheira, *Int. J. Mol. Sci.* **21** (2020), doi:10.3390/ijms21072455.

182. Y. J. Lee, E. Y. Ahn, Y. Park, *Nanoscale Res. Lett.* **14**, 1–14 (2019).

183. Y. S. Chen, Y. C. Hung, I. Liau, G. S. Huang, *Nanoscale Res. Lett.* **4**, 858–864 (2009).

184. S. A. Khan, *Metal nanoparticles toxicity: Role of physicochemical aspects* (Elsevier Inc., 2019; http://dx.doi.org/10.1016/B978-0-12-816960-5.00001-X).

185. A. M. Studer *et al.*, *Toxicol. Lett.* **197**, 169–174 (2010).

186. N. Chen *et al.*, *Biomaterials*. **33**, 1238–1244 (2012).

187. Y. N. Chang, M. Zhang, L. Xia, J. Zhang, G. Xing, *Materials (Basel).* **5**, 2850–2871 (2012).

188. N. Golbamaki *et al.*, *Nanoscale*. **7**, 2154–2198 (2015).

189. S. Pakrashi *et al.*, *PLoS One*. **9** (2014), doi:10.1371/journal.pone.0087789.

190. H. Xie, M. M. Mason, J. P. Wise, *Rev. Environ. Health*. **26**, 251–268 (2011).

191. M. Valko *et al.*, *Int. J. Biochem. Cell Biol.* **39**, 44–84 (2007).

192. E. A. K. Warren, C. K. Payne, *RSC Adv.* **5**, 13660–13666 (2015).

193. R. Masoud *et al.*, *PLoS One*. **10**, 1–17 (2015).

194. H. L. Karlsson *et al.*, *Toxicology*. **313**, 59–69 (2013).

195. L. M. Tolliver *et al.*, *Int. J. Mol. Sci.* **21** (2020), doi:10.3390/ijms21051731.

196. S. Abdel-Ghany *et al.*, *Inorg. Nano-Metal Chem.* **50**, 926–932 (2020).

197. Q. Li, C. Huang, L. Liu, R. Hu, J. Qu, *Nanomaterials*. **8**, 1–13 (2018).

198. K. Uchidan, *Redox Biol.* **1**, 94–96 (2013).

199. A. Manke, L. Wang, Y. Rojanasakul, *Biomed Res. Int.* **2013** (2013), doi:10.1155/2013/942916.

200. A. Albanese, P. S. Tang, W. C. W. Chan, *Annu. Rev. Biomed. Eng.* **14**, 1–16 (2012).

201. H. J. Wang *et al.*, *Toxicol. Vitr.* **24**, 1953–1961 (2010).

202. A. Sharma, A. K. Goyal, G. Rath, *J. Drug Target.* **26**, 617–632 (2018).

203. P. . Michelle Longmire, Peter L. Choyke, M.D., and Hisataka Kobayashi, M.D., *Nanomedicine (Lond)*. **3**, 703–717 (2012).

204. X. Feng *et al.*, *Int. J. Nanomedicine*. **10**, 4321–4340 (2015).

205. D. Ye *et al.*, *Nanoscale*. **5**, 11153–11165 (2013).

206. L. T. M. Sa *et al.*, *J. Pharm. Biomed. Anal.* **70**, 602–604 (2012).

207. Y. Cao, S. Li, J. Chen, *Toxicol. Mech. Methods*. **0**, 1–17 (2020).

208. R. Guadagnini, K. Moreau, S. Hussain, F. Marano, S. Boland, *Nanotoxicology*. **9**, 25–32 (2015).

209. M. J. Akhtar *et al.*, *Int. J. Nanomedicine*. **7**, 845–857 (2012).

210. G. Oberdörster *et al.*, *Part. Fibre Toxicol.* **2**, 1–35 (2005).

211. G. V. Scăeţeanu, L. Ilie, C. Călin, *Am. Chem. Sci. J.* **3**, 247–263 (2013).

212. G. F. Kwakye, M. M. B. Paoliello, S. Mukhopadhyay, A. B. Bowman, M. Aschner, *Int. J. Environ. Res. Public Health*. **12**, 7519–7540 (2015).

213. C. C. Huang, N. S. Chu, C. S. Lu, R. S. Chen, D. B. Calne, *Neurology*. **50**, 698–700 (1998).

214. J. Bornhorst *et al.*, *J. Biol. Chem.* **287**, 17140–17151 (2012).

215. *Neuroleptics, Antipsychotics*.

216. M. Sidoryk-Wegrzynowicz, M. Aschner, *J. Intern. Med.* **273**, 466–477 (2013).

217. K. S. Kirkley, K. A. Popichak, M. F. Afzali, M. E. Legare, R. B. Tjalkens, *J. Neuroinflammation*. **14**, 0–17 (2017).

218. C. E. Gavin, K. K. Gunter, T. E. Gunter, *Biochem. J.* **266**, 329–334 (1990).

219. K. M. Erikson, D. C. Dorman, V. Fitsanakis, L. H. Lash, M. Aschner, *Biol. Trace Elem. Res.* **111**, 199–215 (2006).

220. N. L. Parmalee, M. Aschner, *Neurotoxicology*. **56**, 262–268 (2016).

221. K. Wieghardt, *Angew. Chemie Int. Ed. English*. **28**, 1153–1172 (1989).

222. J. W. Whittaker, *Arch Biochem Biophys*. **23**, 111–120 (2012).

223. H. Sigel, *Metal Ions in Biological Systems: Volume 37: Manganese and Its Role in Biological Processes* (Illustrated, 2000).

224. J. Roth, S. Ponzoni, M. Aschner, *Manganese Homeostasis and Transport* (2018), vol. 176.

225. A. Takeda, *Brain Res. Rev.* **41**, 79–87 (2003).

226. F. Yan *et al.*, *Med. Chem. (Los. Angeles).*, 342–356 (2010).

227. L. Rouco *et al.*, *J. Inorg. Biochem.* **203**, 110918 (2020).

228. S. R. Doctrow *et al.*, *J. Med. Chem.* **45**, 4549–4558 (2002).

229. J. Lee, J. A. Hunt, J. T. Groves, *J. Am. Chem. Soc.* **120**, 6053–6061 (1998).

230. G. Passard, D. K. Dogutan, M. Qiu, C. Costentin, D. G. Nocera, *ACS Catal.* **8**, 8671–8679 (2018).

231. P. Failli *et al.*, 7273–7283 (2009).

232. S. Nistri *et al.*, *Free Radic. Res.* **49**, 67–77 (2015).

233. F. C. Friedel, D. Lieb, I. Ivanović-Burmazović, *J. Inorg. Biochem.* **109**, 26–32 (2012).

234. M. Becatti *et al.*, *Sci. Rep.*, 1–20 (2019).

235. M. Becatti *et al.*, *Vascul. Pharmacol.* **75**, 19–28 (2015).

236. J. Du *et al.*, *Nanotechnology*. **17**, 4923–4928 (2006).

237. A. Vázquez-Olmos *et al.*, *Rev. Adv. Mater. Sci.* **30**, 362–366 (2005).

238. Q. F. Deng, T. Z. Ren, Z. Y. Yuan, *React. Kinet. Mech. Catal.* **108**, 507–518 (2013).

239. H. R. Barai, A. N. Banerjee, N. Hamnabard, S. W. Joo, *RSC Adv.* **6**, 78887–78908 (2016).

240. C. S. Li *et al.*, *Nat. Commun.* **6**, 1–5 (2015).

241. A. S. Prasad, *Mater. Sci. Semicond. Process.* **71**, 342–347 (2017).

242. M. Yin, S. O'Brien, *J. Am. Chem. Soc.* **125**, 10180–10181 (2003).

243. F. Wei, X. Cui, W. Chen, D. G. Ivey, *J. Phys. Chem. C*. **112**, 15075–15083 (2008).

244. Y. H. Son *et al.*, *Coatings*. **9** (2019), doi:10.3390/coatings9100631.

245. Y. F. Han *et al.*, *Catal. Commun.* **7**, 739–744 (2006).

246. N. Singh, M. A. Savanur, S. Srivastava, P. D'Silva, G. Mugesh, *Nanoscale*. **11**, 3958–3967 (2019).

247. N. Singh, M. A. Savanur, S. Srivastava, P. D´Silva, N. Mugesh, *Angew. Chemie Int. Ed. English*. **56**, 14267–14271 (2017).

248. N. Singh, M. Geethika, S. M. Eswarappa, G. Mugesh, *Chem. - A Eur. J.* **24**, 8393–8403 (2018).

249. D. Jeong *et al.*, *ACS Catal.* **5**, 4624–4628 (2015).

250. E. R. Stobbe, B. A. De Boer, J. W. Geus, *Catal. Today*. **47**, 161–167 (1999).

251. A. Maltha, T. L. F. Favre, H. F. Kist, A. P. Zuur, V. Ponec, *J. Catal.* **149**, 364–374 (1994).

252. Y. Wang *et al.*, *J. Mater. Chem. A*. **3**, 2934–2941 (2015).

253. H. Chen, J. He, *J. Phys. Chem. C*. **112**, 17540–17545 (2008).

254. H. Chen, J. He, *Chem. Lett.* **36**, 3–4 (2007).

255. M. M. Hanczyc, *Artif. Life*. **26**, 260–273 (2020).

256. A. Cheng, T. K. Lu, *Annu. Rev. Biomed. Eng.*, 155–178 (2012).

257. K. Musunuru, *JAMA Cardiol.* **2**, 914–919 (2017).

258. M. Vajdy *et al.*, *Immunol. Cell Biol.* **82**, 617–627 (2004).

259. C. You, R. Huang, X. Wei, Z. Zhu, Y. H. P. Zhang, *Synth. Syst. Biotechnol.* **2**, 208–218 (2017).

260. A. G. Bower, M. K. McClintock, S. S. Fong, *Bioeng. Bugs*. **1**, 309–312 (2010).

261. Can Xu, S. Hu, X. Chen, *Mater. Today*. **19**, 516–532 (2016).

262. E. Callaway, *Nature*. **531**, 557–558 (2016).

263. A. N. Zelikin, B. Städler, *Small*. **16**, 1–2 (2020).

264. Y. Elani *et al.*, *Sci. Rep.* **8**, 1–8 (2018).

265. P. L. Luisi, F. Ferri, P. Stano, *Naturwissenschaften*. **93**, 1–13 (2006).

266. A. Salehi-Reyhani, O. Ces, Y. Elani, *Exp. Biol. Med.* **242**, 1309–1317 (2017).

267. D. J. Timson, *Fermentation*. **5**, 1–9 (2019).

268. V. Norris, S. N. Krylov, P. K. Agarwal, G. J. White, *J. Mol. Microbiol. Biotechnol.* **27**, 117–127 (2017).

269. M. Liang, X. Yan, *Acc. Chem. Res.* **52**, 2190–2200 (2019).

270. F. Itel, P. S. Schattling, Y. Zhang, B. Städler, *Adv. Drug Deliv. Rev.* **118**, 94–108 (2017).

271. R. Roodbeen, J. C. M. Van Hest, *BioEssays*. **31**, 1299–1308 (2009).

272. C. Schmitt, A. H. Lippert, N. Bonakdar, V. Sandoghdar, L. M. Voll, *Front. Bioeng. Biotechnol.* **4**, 1–12 (2016).

273. G. Murtas, *Mol. Biosyst.* **5**, 1292–1297 (2009).

274. A. C. Forster, G. M. Church, *Mol. Syst. Biol.* **2** (2006), doi:10.1038/msb4100090.

275. L. yan Zhang, S. hua Chang, J. Wang, *Protein Cell*. **1**, 427–434 (2010).

276. W. J. Streit, R. E. Mrak, W. S. T. Griffin, *J. Neuroinflammation*. **1**, 1–4 (2004).

277. A. Armada-Moreira *et al.*, *ACS Appl. Mater. Interfaces*. **10**, 7581–7592 (2018).

278. A. Armada-Moreira *et al.*, *Adv. Biosyst.* **2**, 1700244 (2018).

279. A. Armada-Moreira *et al.*, *Adv. Biosyst.* **4**, 1–10 (2020).

280. J. C. Xavier, K. R. Patil, I. Rocha, *Microbiol. Mol. Biol. Rev.* **78**, 487–509 (2014).

281. J. Borges, J. F. Mano, *Chem. Rev.* **114**, 8883–8942 (2014).

282. J. J. Richardson *et al.*, *Chem. Rev.* **116**, 14828–14867 (2016).

283. F. Hua, Y. M. Lvov, *Chapter 1 - Layer-by-layer assembly* (2008; http://www.sciencedirect.com/science/article/pii/B9780080450520500038).

284. M. Schönhoff, *J. Phys. Condens. Matter*. **15** (2003), doi:10.1088/0953-8984/15/49/R01.

285. B. Städler, A. D. Price, A. N. Zelikin, *Adv. Funct. Mater.* **21**, 14–28 (2011).

286. A. B. Porto-Pazos *et al.*, *PLoS One*. **6**, 1–8 (2011).

287. Z. Sajedinia, S. Hélie, *Comput. Intell. Neurosci.* **2018** (2018), doi:10.1155/2018/3689487.

288. K. Lenk *et al.*, *Front. Comput. Neurosci.* **13**, 1–19 (2020).

289. A. Armada-Moreira *et al.*, *Front. Cell. Neurosci.* **14**, 1–27 (2020).

290. S. Mahmoud, M. Gharagozloo, C. Simard, D. Gris, *Cells*. **8**, 184 (2019).

291. M. E. Lynge *et al.*, *ACS Appl. Mater. Interfaces*. **5**, 2967–2975 (2013).

292. N. Singh, M. A. Savanur, S. Srivastava, P. D'Silva, G. Mugesh, *Nanoscale*. **11**, 3958–3967 (2019).

293. R. A. Floyd, *Proc. Soc. Exp. Biol. Med.* **222**, 236–245 (1999).

294. R. Nunes P.S., Bezerra M.S., Costa L.P., Cardoso J.C., Albuquerque-Junior R.L., *Public Heal. Engl.* **2780**, 1–2 (2016).

295. A. Jerónimo-Santos *et al.*, *Cereb. Cortex*. **25**, 3107–3121 (2015).

296. S. A. Altman, L. Randers, G. Rao, *Biotechnol. Prog.* **9**, 671–674 (1993).

297. C. A. Schneider, W. S. Rasband, K. W. Eliceiri, *Nat. Methods*. **9**, 671–675 (2012).

298. A. Thill, O. Spalla, *Colloids Surfaces A Physicochem. Eng. Asp.* **217**, 143–151

(2003).

299. R. A. French *et al.*, *Environ. Sci. Technol.* **43**, 1354–1359 (2009).

300. E. Joseph, G. Singhvi, *Multifunctional nanocrystals for cancer therapy: A potential nanocarrier* (Elsevier Inc., 2019; http://dx.doi.org/10.1016/B978-0-12-816505-8.00007-2).

301. J. D. Clogston, A. K. Patri, *Methods Mol. Biol.* **697**, 63–70 (2011).

302. M. G. Carneiro-Da-Cunha, M. A. Cerqueira, B. W. S. Souza, J. A. Teixeira, A. A. Vicente, *Carbohydr. Polym.* **85**, 522–528 (2011).

303. J. Stetefeld, S. A. McKenna, T. R. Patel, *Biophys. Rev.* **8**, 409–427 (2016).

304. M. Kaszuba, D. McKnight, M. T. Connah, F. K. McNeil-Watson, U. Nobbmann, *J. Nanoparticle Res.* **10**, 823–829 (2008).

305. X. Jiang, P. Gray, M. Patel, J. Zheng, J. J. Yin, *J. Mater. Chem. B.* **8**, 1191–1201 (2020).

306. J. Yao *et al.*, *Chem. Sci.* **9**, 2927–2933 (2018).

307. A. M. Schrand *et al.*, *Wiley Interdiscip Rev Nanomed Nanobiotechnol*. **2**, 21–24 (2010).

308. Z. Chen *et al.*, *ACS Nano*. **6**, 4001–4012 (2012).

309. Y. Liu, H. Wu, M. Li, J. J. Yin, Z. Nie, *Nanoscale*. **6**, 11904–11910 (2014).

310. Y. Xia, J. Sun, D. Liang, *Langmuir*. **30**, 7334–7342 (2014).

311. Y. Yoshida, M. Shichiri, *J. Clin. Biochem. Nutr*. **54**, 151–160 (2014).

312. S. Gieseg, S. Duggan, J. M. Gebicki, *Biochem. J.* **350**, 215–218 (2000).

313. S. A. Stoner *et al.*, *Cytom. Part A*. **89**, 196–206 (2016).

314. D. Robinson, N. A. Besley, P. Obshea, J. D. Hirst, *J. Phys. Chem. B*. **115**, 4160–4167 (2011).

315. H. Lee, S. M. Dellatore, W. M. Miller, P. B. Messersmith, *Science (80-.).* **318**, 426–430 (2007).

316. M. E. Lynge, R. Van Der Westen, A. Postma, B. Städler, *Nanoscale*. **3**, 4916–4928 (2011).

317. A. Golabchi, B. Wu, B. Cao, C. J. Bettinger, X. T. Cui, *Biomaterials*. **225**, 119519 (2019).

318. S. Sieste *et al.*, *Adv. Healthc. Mater.* **7**, 1–11 (2018).

319. K. Yang *et al.*, *Biomaterials*. **33**, 6952–6964 (2012).

320. A. Miró, M. T. Hernandez, M. J. Costas, J. C. Cameselle, *J. Biochem. Biophys. Methods*. **22**, 177–184 (1991).

321. J. L. Biedler, M. Schachner, *Cancer Res.* **38**, 3751–3757 (1978).

322. C. Kirchner *et al.*, *Talanta*. **67**, 486–491 (2005).

323. M. E. Rice, *Neuroscientist*. **17**, 389–406 (2011).

324. C. V. Rosadini, J. C. Kagan, *Curr. Opin. Immunol.* **44**, 14–19 (2017).

325. A. Noailles, V. Maneu, L. Campello, P. Lax, N. Cuenca, *Cell Death Dis.* (2018), doi:10.1038/s41419-018-0355-x.

326. B. I. N. Liu, J. Hong, *he J. Pharmacol. Exp. Ther.* **304**, 1–7 (2003).

327. J. J. Neher, U. Neniskyte, J. Zhao, A. M. Tolkovsky, G. C. Brown, *J. Immunol.* **186**, 4973–4983 (2015).

328. C. Woo, J. Lim, J. Kim, *J. Immunol.* (2004), doi:10.4049/jimmunol.173.11.6973.

329. Y. Nolan, E. Vereker, A. M. Lynch, M. A. Lynch, *Exp. Neurol.* **184**, 794–804 (2003).

330. H. Noh, J. Jeon, H. Seo, *Neurochem. Int.* **69**, 35–40 (2014).

331. A. Vargas-Caraveo *et al.*, *Sci. Rep.* **7**, 1–15 (2017).

332. T. Kielian, *J. Neurosci. Res.* **83**, 711–730 (2006).

333. T. Owens, *J. Neuroimmunol.* **159**, 1–2 (2005).

334. C. Farina *et al.*, *J. Neuroimmunol.* **159**, 12–19 (2005).

335. L. F. Eng, R. S. Ghirnikar, *Brain Pathol.* **4**, 229–237 (1994).

336. D. E. Korzhevskii, O. V. Kirik, *Neurosci. Behav. Physiol.* **46**, 284–290 (2016).

337. S. Alarifi, D. Ali, S. Alkahtani, *Biomed Res. Int.* **2017** (2017), doi:10.1155/2017/5478790.

338. Y. Huang *et al.*, *Angew. Chemie*. **128**, 6758–6762 (2016).

339. J. Pike, J. Hanson, L. Zhang, S. W. Chan, *Chem. Mater.* **19**, 5609–5616 (2007).

6. Supplementary Data

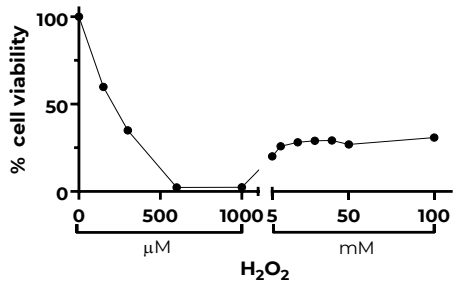

Supplementary figure I: Concentration dependant H_2O_2 toxicity to SH-SY5Y neuroblastoma cell line. Cell viability of cell exposed for 24 hours to a range of H_2O_2 concentrations – 150, 300, 600, 1000 µM and 5, 10, 20, 30, 40, 50, 100 mM. All data normalized to a negative control: untreated cells. **N=1**

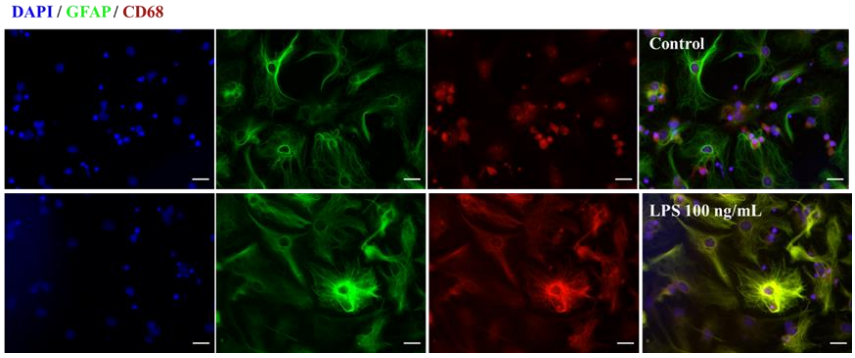

Supplementary figure II: Immunostaining of cortex primary mixed cell cultures. When stimulated with LPS, beside occasional single cell reactivity increase, no significant increase in GFAP expression was registered. CD68 is seen with a different expression phenotype and intensity, apparent to co-localize with GFAP. Untreated cells showed low levels of CD68 staining, concentrating mainly in the nucleus. Scale bar 20 µm.

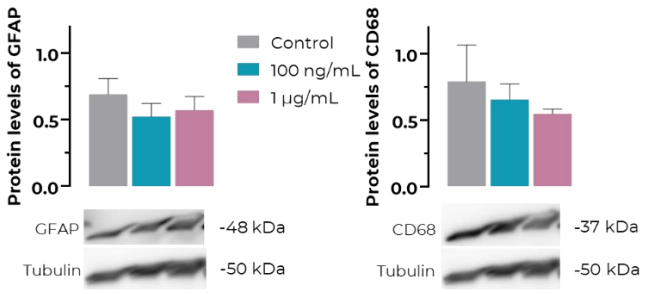

Supplementary figure III: Protein levels of GFAP and CD68 in primary mixed cell cultures. The ratio of protein of interest, with the internal control tubulin was normalized to the control (non- treated cells). The two evaluated conditions are with 100 ng/mL and 1 µg/mL of LPS for 24 hours. The in no evidence of any significant change in any of the proteins expression when stimulated with LPS. Data expressed as mean ± SEM, **N=3** for GFAP analysis and **N=2** for CD68.